**Universidade do Estado do Rio de Janeiro**
Centro de Tecnologia e Ciências
Instituto de Química

Arthur Henrique Azevedo Gonçalves

# $Fe_3O_4$/RGO composites for the indigo carmine photo-Fenton discoloration

Rio de Janeiro
2023

Arthur Henrique Azevedo Gonçalves

**Fe3O4/RGO composites for the indigo carmine photo-Fenton discoloration**

Dissertação apresentada, como requisito parcial para a obtenção do grau de Mestre, ao Programa de Pós-Graduação em Engenharia Química, da Universidade do Estado do Rio de Janeiro. Área de concentração: Processos Químicos, Petróleo e Meio Ambiente.

Orientadores:

Prof. Dra. Cristiane Assumpção Henriques,

Prof. Dra. Deborah Vargas Cesar

Dr. Alexandre Barros Gaspar

Rio de Janeiro

2023

CATALOGAÇÃO NA FONTE
UERJ / REDE SIRIUS / BIBLIOTECA CTC/Q

G635 Gonçalves, Arthur Henrique Azevedo.

Fe3O4/RGO composites for the indigo carmine photo-Fenton discoloration – 2023.
92 f.

Orientador (a): Cristiane Assumpção Henriques
Deborah Vargas Cesar
Alexandre Barros Gaspar

Dissertação (Mestrado) – Universidade do Estado do Rio de Janeiro. Instituto de Química.

1. Corantes e tingimento – Teses. 2. Indústria têxtil – Teses. 3. Efluentes - Teses. Água – Purificação – Teses. I. Henriques, Cristiane Assumpção. II. Cesar, Deborah Vargas. III. Gaspar, Alexandre Barros. IV. Universidade do Estado do Rio de Janeiro. Instituto de Química. V. Título.

CDU 541.128



Assinatura

20/03/2024
Data

Arthur Henrique Azevedo Gonçalves

**$Fe_3O_4$/RGO composites for the indigo carmine photo-Fenton discoloration**

Dissertação apresentada, como requisito parcial para a obtenção do grau de Mestre, ao Programa de Pós-Graduação em Engenharia Química, da Universidade do Estado do Rio de Janeiro. Área de concentração: Processos Químicos, Petróleo e Meio Ambiente.

Aprovada em 21 de agosto de 2023.

Banca Examinadora:

Prof. Dra. Cristiane Henriques (Orientador)
Instituto de Química – Universidade do Estado do Rio de Janeiro

Prof. Dra. Deborah Vargas Cesar (Orientador)
Instituto de Química – Universidade do Estado do Rio de Janeiro

Dr. Alexandre Barros Gaspar (Orientador)
Divisão de Catálise, Biocatálise e Processos Químicos – Instituto Nacional de Tecnologia

Prof. Dr. Fatima Maria Zanon Zotin
Instituto de Química - UERJ

Prof. Dr. André Von-Held Soares
Departamento de Engenharia Química e de Petróleo – Universidade Federal Fluminense

Dra. Erika Batista Silveira
Divisão de Catálise, Biocatálise e Processos Químicos – Instituto Nacional de Tecnlogia

Rio de Janeiro

2023

## DEDICATÓRIA

À Luciene Azevedo, minha querida mãe, (*in memorian*).

## AGRADECIMENTOS

À minha mãe Luciene (*in memorian*) e ao meu pai Marcus. Sem seus contínuos estímulos e apoio, eu nunca chegaria aqui. Obrigado por me proporcionarem tudo o que um filho precisa para seguir em frente. Amo vocês!

Ao meu irmão Victor Hugo pelas conversas, ajudas e amor sincero.

Aos meus avós Paulino (*in memorian*) e Maria Tereza. Muito obrigado por ajudarem na minha educação, pelos mimos e pelo amor.

À Cristina, que ajudou muito a minha família na minha criação.

À minha orientadora Cristiane Henriques e coorientadora Deborah Cesar, por todos os ensinamentos, orientação e conselhos. Sempre muito solícitas e abertas a sugestões, questionamentos e novos rumos da pesquisa.

Ao meu coorientador Alexandre Gaspar (DICAP/INT), por sempre me apoiar e confiar no meu trabalho. Obrigado pelos valiosos ensinamentos, discussões, novos temas e por me dar autonomia para sugerir e executar novos testes e caracterizações.

Ao meu colega de pesquisa Pedro Siciliano, que possibilitou a execução de diversas atividades laboratoriais e apoiou toda a pesquisa.

À Noema Miranda que sempre me apoiou e confiou no meu crescimento. Obrigado por tudo!

Aos meus amigos Allan, Felipe, Ivan, Jorge, Leonardo, André, João e Adriana. Sempre muito parceiros e me aturando. Sempre acreditando no meu crescimento e me incentivando.

Aos meus superiores Javier Velasco e Rafael Barrozo (DICOR/INT), que sempre me motivaram a me capacitar e proporcionaram que eu me dedicasse, também, ao PPGEQ.

Aos meus colegas/amigos de laboratório Rejane, Hugo, Rachel, Gabriela, Emerson, David, Christopher, Andrea, Rodrigo, Thais, Priscilla, Valéria, Marcello e Maria. Estamos todos os dias juntos, obrigado por confiarem no meu trabalho.

Ao CNPq pelo suporte financeiro.

Ao CBPF, pelas análises de EPR, VSM e Mössbauer, e à COPPE/UFRJ, pelas análises de DRS.

Ao CENANO/INT, pelas análises de XPS, FE-SEM e STEM-in-SEM e LAMAP/INT pelas análises de TGA.

À UERJ, que com sua estrutura permitiu que eu seguisse minha pesquisa e aprendizado.

Ao INT, além de me proporcionar infraestrutura, há 12 anos confia no meu trabalho.

Sei que posso estar cometendo injustiça por não nomear todos os que me ajudaram e apoiaram em algum momento. Portanto, esse agradecimento vai para todos vocês!

A ciência nunca resolve um problema sem criar pelo menos outros dez.

*George Bernard Shaw*

**ABSTRACT**

GONÇALVES, Arthur Henrique Azevedo. *$Fe_3O_4$/RGO composites for the indigo carmine photo-Fenton discoloration.* 2023. 88 f. Dissertação (Mestrado em Engenharia Química) - Instituto de Química, Universidade do Estado do Rio de Janeiro, Rio de Janeiro, 2023.

Textile Industry plays an important role both in Brazil and the world. However, it is responsible for generate large quantities of synthetic dye-containing effluents. It is well known that many of these dyes are stable when released in the nature. One example is indigo carmine (IC), used worldwide in denim fabrication. This dye is toxic, harmful to human health, and causes serious environmental impacts. Thus, the development of new technologies aiming to treat textile dye-containing effluents it is of great importance. In this work, nanocomposites of magnetite ($Fe_3O_4$) anchored on reduced graphene oxide (RGO) were synthesized an evaluated in the IC photo-Fenton discoloration, an advanced oxidative process, considered one of the most promising effluent treatment approaches. Different physicochemical characterization techniques showed that magnetite nanoparticles were successfully anchored on RGO sheets. Besides, the presence of RGO is responsible for improving magnetite properties, yielding to high active materials for IC discoloration. Also, the magnetic properties of these materials provided a simple separation method from the reaction medium. Reuse tests were conducted with the nanocomposite with the best performance showing that it can be used for, at least, 4 cycles, without significant activity loss.

Keywords: reduced graphene oxide; magnetite; indigo carmine; photo-fenton; water remediation.

# RESUMO

GONÇALVES, Arthur Henrique Azevedo. *Compósitos $Fe_3O_4$/RGO para a descoloração foto-Fenton do índigo carmim.* 2023. 88 f. Dissertação (Mestrado em Engenharia Química) - Instituto de Química, Universidade do Estado do Rio de Janeiro, Rio de Janeiro, 2023.

A Indústria Têxtil tem grande importância no Brasil e no Mundo. Entretanto, é responsável por gerar grandes quantidades de efluentes contendo corantes sintéticos. É sabido que muitos dos corantes utilizados são estáveis quando despejados na natureza. Um exemplo é o índigo carmim (IC), usado mundialmente na produção de denim. Este corante é conhecido por ser tóxico, perigoso para o ser humano e por causar sérios problemas ambientais. Logo, o desenvolvimento de novas tecnologias que visam o tratamento de efluentes contendo corantes têxteis é de suma importância. Neste trabalho, nanocompósitos de magnetita ($Fe_3O_4$) ancorada em óxido de grafeno reduzido (RGO) foram sintetizados para serem avaliados na descoloração foto-Fenton do IC, um processo oxidativo avançado, considerado uma das formas de tratamento mais promissoras. Diversas técnicas de caracterização físico-química mostraram que nanopartículas de magnetita foram ancoradas com sucesso sobre folhas de RGO. Além disso, a presença de RGO no compósito é responsável por aprimorar as propriedades da magnetita, resultando em materiais altamente ativos para a descoloração do IC. Outrossim, o magnetismo desses materiais possibilitou a fácil separação do meio reacional. Testes de reuso foram realizados com o nanocompósito que apresentou a melhor performance, mostrando que o mesmo pode ser utilizado por, no mínimo 4 ciclos, sem ter perdas significativas na atividade.



Palavras-chave: óxido de grafeno reduzido; magnetita; índigo carmim; foto-fenton; tratamento de água.

## FIGURES INDEX

Figure 1 – SEM image of GO. 17
Figure 2 – FESEM image of RGO. 18
Figure 3 – SEM image of $Fe_3O_4$/RGO. 18
Figure 4 – FESEM image of $Fe_3O_4$/RGO. 19
Figure 5 – FESEM -EDX mapping of $Fe_3O_4$/RGO. 19
Figure 6 – FESEM -EDX composition of $Fe_3O_4$/RGO. 20
Figure 7 – XRD patterns for graphite, GO, and $Fe_3O_4$/RGO. 21
Figure 8 – TGA curves for GO, RGO, and $Fe_3O_4$/RGO. 22
Figure 9 – Raman spectra: D and G band comparison between the carbonaceous materials. 23
Figure 10 – Whole Raman spectra comparison between $Fe_3O_4$/RGO, and RGO. 24
Figure 11 – XPS survey spectra for GO, RGO, and $Fe_3O_4$/RGO. 25
Figure 12 – XPS C1s spectra for GO, RGO, and $Fe_3O_4$/RGO. 26
Figure 13 – XPS O1s spectra for GO, RGO, and $Fe_3O_4$/RGO. 26
Figure 14 – Fe2p spectrum peak fitting for $Fe_3O_4$/RGO. 27
Figure 15 – Indirect bandgap determination for $Fe_3O_4$/RGO composite. 28
Figure 16 - Magnetization M as a function of magnetic field H at 300K. The inset shows the enlarger view of magnetization curve at low magnetic field region. 29
Figure 17 – Indigo carmine discoloration in function of time. 31
Figure 18 – UV-Visible spectra of indigo carmine dye discoloration with $Fe_3O_4$/RGO composite. 31
Figure 19 – Illustrative picture of dye discoloration and magnetic separation. 33
Figure 20 – Reusability of the $Fe_3O_4$/RGO composite. 34
Figure 21 – XPS Fe2p spectrum peak fitting for $Fe_3O_4$/RGO after the firs indigo carmine discoloration test. 34
Figure 23– SEM images of bulk $Fe_3O_4$. 43
Figure 22 – SEM images of bare reduced graphene oxide. 43
Figure 24– STEM-in-SEM micrograph of nanocomposite 3. 44
Figure 25 – STEM-in-SEM micrograph of nanocomposite 2. 44
Figure 26 – STEM-in-SEM micrograph of nanocomposite 1. 45
Figure 27 – XRD patterns for RGO and all nanocomposites. 47
Figure 28 – XRD patterns of all nanocomposites to highlight RGO halo. 47
Figure 29 – TGA analysis for RGO and all nanocomposites. 48

Figure 30 – DRS spectra for all nanocomposites and bare $Fe_3O_4$. ..... 49
Figure 31 – EPR spectra for all nanocomposites. ..... 51
Figure 32 – VSM curves for all composites. ..... 52
Figure 33 – $^{57}$Fe Mössbauer absorption spectrum at 300K for nanocomposite 1. ..... 54
Figure 34 – $^{57}$Fe Mössbauer absorption spectrum at 300K for nanocomposite 2. ..... 54
Figure 35 – $^{57}$Fe Mössbauer absorption spectrum at 300K for nanocomposite 3. ..... 54
Figure 36 – IC discoloration with different $H_2O_2$ inputs, and without a photocatalyst. ..... 56
Figure 37 – UV-visible spectra for photolysis tests. ..... 57
Figure 38 – IC photo-Fenton discoloration for the different nanocomposites with a catalyst dosage of 0.33 $g.L^{-1}$. ..... 59
Figure 39 – IC photo-Fenton discoloration with different dosages of nanocomposite 3. ... 61
Figure 40 – IC photo-Fenton discoloration with different $H_2O_2$ concentrations and nanocomposite 3 (0.33$g.L^{-1}$). ..... 62
Figure 41 – UV-visible absorption spectra obtained for each time interval for IC photo-Fenton discoloration with nanocomposite 3 (0.33 $g.L^{-1}$). ..... 62
Figure 42 – IC photo-Fenton discoloration curves for nanocomposite 3 recycling tests. ... 63
Figure 43 – UV-visible absorption spectra obtained for each time interval for IC photo-Fenton discoloration with the third reuse of nanocomposite 3 (0.33 $g.L^{-1}$). ..... 63
Figure 44 – Fe2p XPS photoelectron spectra of fresh and reused (3 recycles, or 4 runs) nanocomposite 3. ..... 64
Figure 45 – $Fe2p_{3/2}$ peak fitting of fresh and reused (3 recycles, or 4 runs) nanocomposite 3. 64
Figure A1 – UV-visible absorption spectra obtained for different IC concentrations. ..... 83
Figure A2 – Calibration curve for different IC concentrations of Figure A1 ..... 83
Figure A3 – EDX mapping of site 1. ..... 84
Figure A4 – EDX mapping of site 2. ..... 84
Figure A5 – Isotherm plots for all nanocomposites. ..... 85
Figure A6 – Pore size distribution for all nanocomposites. ..... 85
Figure A7 – Ln ($C_0$/C) x time kinetic plot for IC discoloration with different $H_2O_2$, in the absence of a heterogeneous catalysts ..... 86
Figure A8 – IC discoloration curves for all nanocomposites with a catalyst dosage of 0.67 $g.L^{-1}$, and a fixed $H_2O_2$ concentration of 2.3 x $10^{-1}$M. ..... 86
Figure A9 – Ln ($C_0$/C) x time kinetic plots for IC discoloration with all nanocomposites (0.33 $g.L^{-1}$), and fixed $H_2O_2$ concentration of 2.3 x $10^{-1}$ M. ..... 87

Figure A10– Ln ($C_0$/C) x time kinetic plots for different nanocomposite 3 dosages in IC discoloration, with a fixed $H_2O_2$ concentration of 2.3 x $10^{-1}$. ..... 87
Figure A11 – Ln ($C_0$/C) x time kinetic plots for IC discoloration with nanocomposite 3 (0.33 $g.L^{-1}$), with varied $H_2O_2$ concentrations. ..... 88

## TABLES INDEX

Table 1 – Carbon species after C1s peak fitting. ..... 27
Table 2 – Zeta potential at pH=6 for RGO, and $Fe_3O_4$/RGO composite. ..... 29
Table 3 – Compilation of different photocatalysts in IC discoloration. ..... 32
Table 4 – Nanocomposites nomenclatures, iron precursor contents, and approximate mass ratio of the precursors. ..... 40
Table 5 – STEM-in-SEM particle counting, FE-SEM-EDX iron content, crystallite size (by XRD), BET specific surface area, and mesopore volumes of all nanocomposites. ..... 45
Table 6 – Parameters obtained by DRS, EPR spectra and VSM curves for all nanocomposites. 52
Table 7 – Hyperfine parameters from Mössbauer spectra of nanocomposite 1. ..... 55
Table 8 – Hyperfine parameters from Mössbauer spectra of nanocomposite 2. ..... 55
Table 9 – Hyperfine parameters from Mössbauer spectra of nanocomposite 3. ..... 55
Table 10 – IC heterogeneous catalysis discoloration results of different works found in literature. 67
Table A1 – Compilation of all IC discoloration results in this work (article 2). ..... 82

**TABLE OF CONTENTS**

INTRODUCTION ..... 9
1 SYNTHESIS OF A MAGNETIC FE3O4/RGO COMPOSITE FOR THE RAPID PHOTO-FENTON DISCOLORATION OF INDIGO CARMINE DYE ..... 11
**1.1 Introduction ..... 11**
**1.2 Experimental ..... 13**
1.2.1 Synthesis of Graphene Oxide, Reduced Graphene Oxide and Magnetite/Reduced Graphene Oxide Composite ..... 13
1.2.2 Characterization ..... 14
1.2.3 Photo-Fenton discoloration of indigo carmine ..... 16
**1.3 Results and discussion ..... 16**
**1.4 Conclusions ..... 35**
2 EFFECT OF FE3O4: RGO RATIOS IN MAGNETIC NANOCOMPOSITES APPLIED FOR DYE DISCOLORATION ..... 36
**2.1 Introduction ..... 36**
**2.2 Materials and Methods ..... 38**
2.2.1 Synthesis of the materials ..... 38
2.2.2 Characterization ..... 40
2.2.3 Indigo carmine (IC) photocatalysis ..... 41
**2.3 Results and discussion ..... 42**
2.3.1 Materials characterization ..... 42
2.3.2 IC photo-Fenton discoloration ..... 56
2.3.2.1 IC discoloration in the absence of a heterogeneous catalyst ..... 56
2.3.2.2 Heterogeneous IC photo-Fenton discoloration ..... 58
2.3.2.3 Critical assessment of IC discoloration with $Fe_3O_4$/RGO nanocomposites ..... 65
**2.4 Conclusion ..... 68**
CONCLUSIONS AND SUGGESTIONS ..... 69
REFERENCES ..... 71
APPENDIX A – SUPPLEMENTARY MATERIAL OF ARTICLE 2 ..... 82
APPENDIX B – SCIENTIFIC PRODUCTION (JOURNALS) ..... 89
APPENDIX C – SCIENTIFIC PRODUCTION (PROCEEDINGS OF CONFERENCES) 92

## INTRODUCTION

Textile industry has an important role worldwide, due to its great potential of creating jobs, developing regions and profit generation. In Brazil, for example, which is among the 5 largest denim producers and consumers in the world, this sector in 2021 represented 19.5% of the workers from industrial production (IEMI, 2022 *apud* ABIT, 2023). However, textile industry is known by generating expressive dye-containing effluent volumes, requiring attention and methods to prevent the water bodies.

Nowadays, there are thousand types of dyes, being traded worldwide, with an annual production that exceeds 700.000 tons (Moussavi; Mahmoudi 2009). It is estimated that, ending the synthetic dyes production, there are significant losses that reach 1%-2%. Besides, after the textile industry dyeing and finishing procedures, around 20% to 50% of synthetic dyes are lost and disposed in the water bodies (Zanoni; Yamanaka, 2016).

Among the great variety of synthetic dyes, indico carmine (IC) is an example of the most used dies in the textile industry (Shanker *et al.*, 2017). By owing an intense blue color, it is largely employed in denim, and clothing production. On the other hand, it is about being an anionic dye, indigoid, very stable, and toxic. IC is known as harmful for humane health and environment (Othman *et al.*, 2007). Thus, designing new effluent treatment techniques are important to mitigate the environmental and health problems caused by textile dyes.

An interesting approach in the dye-containing effluents management is the heterogeneous photocatalysis by using photo-Fenton processes. This type of treatment has many advantages, such as: easy catalyst separation from the medium, catalyst reuse, mild conditions operations, and possibility of mineralizing the pollutants. They are known as Advanced Oxidative Processes (AOPs), where the decomposition of hydrogen peroxide ($H_2O_2$) leads to hydroxyl radicals (•OH) generation. These structures have a strong oxidant character, being responsible for attacking the pollutant molecules, cleaving the C-C/C-H bonds, leading to their mineralization.

In the last years, semiconductor compounds received a crescent notoriety in the heterogeneous photocatalysis of organic pollutants (Othman *et al.*, 2007; Vautier *et al.*, 2001). Magnetite spinel ($Fe_3O_4$) is an iron oxide that has interesting features, such as: narrow band gaps, demanding less energy to generate the •OH radicals; strong magnetic character, facilitating the separation processes; are biocompatible, resulting in environmental-friendly materials; and abundant, making possible the synthesis of cost-effective photocatalysts. On the other hand, studies report that bare $Fe_3O_4$ tends to agglomerate, thus losing its activity.

Graphene-based materials, such as reduced graphene oxide (RGO) own diverse attractive physicochemical properties. Their textural, electronic, and optical features resulted in increasingly studies to combine semiconductor oxides with RGO for effluent treatment. Besides, as a support to anchor the semiconductor particles, RGO can prevent particle agglomeration, and improve their physicochemical properties.

In this regard, this work is addressed to synthesize a magnetic $Fe_3O_4$/RGO composite to act as a photocatalyst in the IC photo-Fenton discoloration. The composite physicochemical properties are studied to associate its activity in the IC discoloration. Also, reaction parameters such as photocatalyst, and $H_2O_2$ loads are investigated to understand their contribution in the IC photo-Fenton discoloration.

This document is structured as a compendium of two scientific articles, where Chapter 1 is the already published work describing the synthesis of a $Fe_3O_4$/RGO composite, with approximately 90%wt of $Fe_3O_4$, and 10%wt of RGO, for the IC discoloration (Gonçalves *et al.*, 2020). Based on this work, a second article (Chapter 2) was published (Gonçalves *et al.*, 2024) aiming to investigate the $Fe_3O_4$:RGO ratio in IC photo-Fenton discoloration. Then, the best catalyst was selected to perform a study varying the oxidant reactant, and the composite loads, providing kinetic data. In sequence, the Conclusion section aims to highlight the main results, and to discuss new steps for further works.

# 1 SYNTHESIS OF A MAGNETIC FE3O4/RGO COMPOSITE FOR THE RAPID PHOTO-FENTON DISCOLORATION OF INDIGO CARMINE DYE

The first results of this dissertation were reported and discussed in this article. The composite (~90%wt)$Fe_3O_4$/(~10%wt)RGO was synthesized by employing an adaptation of the facile synthesis reported by Qiu *et al.* (2016). Initial indigo carmine photo-Fenton discoloration tests were performed, showing outstanding activity of this composite. Thus, thorough physicochemical characterizations were carried out to associate its properties to its activity. Also, the magnetic properties of this composite provided an easy recovery from the reaction medium. The composite was then reused, and it was not observed a significant activity loss. One explanation for maintaining its activity after the first cycle of indigo carmine photo-Fenton discoloration, is the preservation of the $Fe_3O_4$ spinnel, revealed by X-Ray Photoelectron Spectroscopy (XPS) technique.

## 1.1 Introduction

Water pollution caused by dyes has been the focus of much concern over the last years due to the massive amounts used every day, leading to environmental and health complications. Several types of processes are responsible for dye wastewater pollution, being the textile industry the most contributor to this problem (Yaseen; Scholz, 2019). Besides, it is worsened by the high stability of the dyes (Tho *et al.*, 2018). Among the variety of dyes on the wastewater pollution, indigo carmine, also called Acid Blue 74, is an indigoid dye that is known by its hazardousness and toxicity (Mittal *et al.*, 2006). Indigo carmine is carcinogenic and is associated with many other serious health problems (Barka *et al.*, 2008; Jenkins, 1978).

Different processes based on physical-chemical properties have been studied to reduce wastewater pollution by organic dyes (Mittal *et al.*, 2006; Boruah *et al.*, 2015; Lin; Lin, 1993; Hai *et al.*, 2013; Daud; Hameed, 2011). Among them, adsorption is one of the most common processes used to remove pollutants from wastewaters, such as drugs, dyes, and others. Maksoud *et al.* (2020) discussed its advantages and disadvantages, focusing on magnetic nanoparticules and biosorbents. Eco-friendly, low cost, and high efficiency are some

properties that characterize them as excellent adsorbents. However, adsorption has several challenges, such as experimental conditions, commercial and disposal issues.

Heterogeneous photocatalytic approach is considered one of the most promising alternatives for wastewater pollution due to many advantages. At first, heterogeneous systems are attractive due to the easy removal from the medium, thus facilitating the catalyst reuse. Also, by using a UV source, photocatalytic processes can be carried out at moderate temperatures and pressures (Barka *et al.*, 2008). Furthermore, the possibility of dye mineralization, where the organic dye molecules can be converted into $H_2O$, $CO_2$, and mineral acids (Barka *et al.*, 2008; Li *et al.*, 2015), is a significant advantage when compared to physical processes.

In a review written by Shestakova and Sillanpää (2013), photo-Fenton process could be a viable alternative for wastewater dye removal due to many advantages, such as rapid reactions and total mineralization of the pollutants. Fenton-like reactions are considered advanced oxidation processes (AOPs), where $H_2O_2$ is decomposed into •OH radicals (Sreeja; Sosamony, 2016). These radicals have an extremely oxidant character and, therefore, can mineralize organic dyes. Metal oxides assisted by a light source can be used as heterogeneous photocatalysts to improve $H_2O_2$ decomposition, increasing the photo-Fenton reaction rates. Based on what was mentioned, iron oxides are extensively studied due to their abundance (Li; Zhang, 2010; Liu *et al.*, 2017) and relatively low-cost (See, *et al.*, 2014).

Magnetite ($Fe_3O_4$) is a mixed oxide composed of both $Fe^{2+}$ and $Fe^{3+}$ ions that can generate •OH radicals improving the photo-Fenton process (Hsieh; Lin, 2012). Furthermore, due to its magnetic character, which facilitates the catalyst separation from the medium, and other interesting properties (such as biocompatibility and low toxicity), magnetite rises as an attractive photo-Fenton catalyst alternative (Yang *et al.*, 2015). However, if used without being supported, magnetite particles tend to form $Fe(OH)_3$ (Nieto-Juarez; Kohn, 2013), leading to the catalytic activity suppression. For that reason, $Fe_3O_4$ hybrid materials emerge as promising catalysts to photo-Fenton reactions.

Graphene can be defined as a single layer sheet composed of sp2 hybridized carbon, in a hexagonal structure, and it is considered a 2D material due to its carbon atom thick (Rao *et al.*, 2009; Geim; Novoselov, 2007). Graphene has remarkable properties such as high specific area (Steurer *et al.*, 2009), conductivity (Zhang; Pan, 2011), and excellent electron mobility (Ambrosi *et al.*, 2016). Therefore, it is an interesting alternative to support different oxides, such as $Fe_3O_4$, that could be used as heterogeneous photocatalyst as aforementioned.

In the way of Fenton processes (with and without UV-light) for dye wastewater removal, many different works employing $Fe_3O_4$/graphene-like hybrids have been published in the last years. Jiang *et al.* (2017) synthesized RGO/$Fe_3O_4$ by using brown alga (Sargassum thunbergii) as a reducing agent and this composite showed 96% of methylene blue discoloration. Arshad *et al.*, (2018), using a graphene/$Fe_3O_4$ nanocomposite for methyl orange (MO) treatment, reached 99.24% of MO removal. For rhodamine B removal, Qin *et al.* (2014) first performed adsorption tests then successfully regenerated their $Fe_3O_4$/RGO composite by adopting the Fenton approach. Magnetic ZnFe2O4-reduced graphene oxide was developed and tested by Yao *et al.* (2014) in the photo-Fenton discoloration of various dyes. It is important to note that besides the excellent dye discoloration activity, these authors highlight the easy separation of their $Fe_3O_4$/RGO composites due to their magnetic properties.

For indigo carmine photocatalysis, there are works employing different materials with remarkable results (Agorku *et al.*, 2015a; Vautier *et al.*, 2001; Othman *et al.*, 2007; Galindo *et al.*, 2001). However, to this date, our group did not find any work that uses a facile synthesized magnetic $Fe_3O_4$/RGO composite for indigo carmine photo-Fenton discoloration. Qiu *et al.* (2016) reported a facile synthesis of a $Fe_3O_4$/RGO composite that can be employed in order to achieve highly dispersed $Fe_3O_4$ nanoparticles that can be used as photo-Fenton catalysts.

In this way, this work aimed to synthesize magnetic $Fe_3O_4$ decorated on reduced graphene oxide ($Fe_3O_4$/RGO) by a simple approach. The synthesized materials will be evaluated as a heterogeneous catalyst for the indigo carmine discoloration by the photo-Fenton process. Their catalytic performance will be discussed based on their physicochemical properties.

## 1.2 Experimental

### 1.2.1 Synthesis of Graphene Oxide, Reduced Graphene Oxide and Magnetite/Reduced Graphene Oxide Composite

The graphene oxide (GO) synthesis employed in this work was a modified Hummers method, as previously described by Soares *et al.* (2018). The graphite used was a commercial

graphite (Grafine 996100, kindly provided by Nacional de Grafite, Brazil). In a glass flat bottom flask, 11.5 mL of an $H_2SO_4$ (95 wt.%, Vetec, Brazil) solution and 270 mg of $NaNO_3$ (98 wt.%, Isofar, Brazil) were added to 220 mg of graphite under magnetic stirring at 0 ºC. After that, $KMnO_4$ (99 wt.%, Isofar, Brazil) was continuously added to the mixture, which was kept at 35 ºC for 1 h. Distilled water was then added to the mixture, and the temperature was set to 98 ºC ± 5 ºC for 15 min. After, 60 mL of a $H_2O_2$ solution (10 wt.%, Isofar, Brazil) were added to the mixture and maintained at 20 ºC for 1 h. Finally, in order to remove the impurities, the mixture was filtered and washed with 20 mL of $H_2O_2$ (10 wt.%), 20mL of $H_2SO_4$ (5 wt.%), centrifuged (each cycle) and then washed with distilled water to reach pH = 6.0.

The $Fe_3O_4$/RGO composite was synthesized as an adaptation of Stöber-like synthesis described by Qiu *et al.* (2016). 200 mg of GO was dispersed in an ethanol/acetonitrile solvent in the ratio of 3:1 during 90 min using an ultrasonic bath. After that, 1.33 mL of ammonium hydroxide (28 wt.%) was added, and the mixture was maintained at magnetic stirring for 30 min at room temperature. Then, 50 mL of a solution of iron nitrate ($Fe(NO_3)_3.9H2O$) (0.17 mol $L^{-1}$), from Sigma-Aldrich, Brazil, was slowly added to the mixture and stirred for 30 min. Next, the suspension was refluxed at 60 ºC for 40 h under magnetic stirring. After that, the suspension was centrifuged, washed with ethanol, and dried at 40ºC in an oven. The solid obtained was treated at 500 ºC (heating rate of 1.5 ºC min-$^{1}$), for 2 h, under 50 mL $min^{-1}$ of pure nitrogen flow. In order to prepare a reference RGO, a desirable amount of GO (without the iron nitrate addition procedure) was treated at 500 ºC (heating rate of 1.5 ºC $min^{-1}$), for 2 h, under 50 mL $min^{-1}$ of pure nitrogen flow.

### 1.2.2 Characterization

Scanning Electron Microscopy (SEM) and Field Emission Scanning Electron Microscopy (FESEM) were used to investigate the carbonaceous materials and composite morphology. Electron Dispersive X-Ray (FESEM-EDX) was performed to observe the C, O and Fe distribution and composition in the Fe3O4/RGO composite. SEM images were registered in an INSPECT microscope. FESEM images, FESEM-EDX mapping and composition were acquired in a Quanta FEG 450, without metallic covering. Both microscopes are from FEI company.

The crystallographic analysis was performed by X-Ray diffractometry (XRD) in a Rigaku Miniflex II diffractometer, with CuKα radiation of 1.540562 Å, and employing a tension of 30 kV and 15 mA. The range was 2θ from 5º to 70º, with a step of 0.05º and 2º min-$^{1}$/step.

The thermal stability of the materials studied in this work was investigated using Thermo Gravimetric Analysis (TGA). The analyses were performed in a STA 409 Pc Luxx (NETZSCH) equipment from room temperature to 1000ºC with a 20ºC min$^{-1}$ heating rate and 20 mL min$^{-1}$ of air flow.

Laser Raman Spectroscopy (LRS) analysis was performed at room temperature, in a LabRAM HR800 (Horiba-Jobin Yvon), with a BX41 confocal microscope (Olympus), and a micro-spectrometer equipped with a thermal conductivity detector operating at -70 ºC and a 632 nm He-Ne laser. The measurements were taken with 10s beam exposure time, and 10 accumulations.

The Diffuse Reflectance Spectroscopy (DRS) analysis, in the UV-vis range, was performed using a Varian Cary 500 Scan to estimate the composite bandgap value. The analyses were obtained in the 200–800 nm range. $BaSO_4$ was used as a diluent to the composite (1:25) and as the reference for the experiment.

Zeta potential was measured to investigate the electrostatic characteristic of $Fe_3O_4$/RGO composite and RGO in an aqueous medium. 10 mg of material were dispersed in 20 mL of ultrapure water for 30 min with magnetic stirring, to ensure the water adsorption equilibrium with the catalyst. Then, aliquots of 5 mL were measured in an SZ100 equipment (Horiba Scientific).

$Fe_3O_4$/RGO magnetic properties were investigated by means of Vibrating Sample Magnetometry (VSM) analysis in a Physical Property Measurements System (PPMS) DynaCool of Quantum Design.

X-Ray Photoelectron Spectroscopy (XPS) measurements were obtained in a PHOIBOS 150 (SPECS) with a non-monochromatic AlKα (1.4 keV) source. The anode operation was with 10 W of power rating. Survey and high-resolution spectra pass energies were 50 eV and 20 eV, respectively. All spectra were calibrated by using the adventitious carbon photoelectron energy of 284.6 eV, and all peak fitting were performed with a Shirley baseline in CasaXPS software (version 2.3.17) (Casa XPS, 2018). The analysis chamber pressure range was $10^{-10}$-$10^{-9}$ mbar during all analyses.

### 1.2.3 Photo-Fenton discoloration of indigo carmine

Photocatalysis of indigo carmine dye was performed in a 50 mL glass batch reactor with a cooling jacket and the UV source was a Master HPI-T (400W) metal vapor lamp from PHILIPS as reported by Costa *et al.* (2019). Before reaction, 20 mg of $Fe_3O_4$/RGO were dispersed in 14.3 mL of distilled water in an ultrasonic bath during 30 min and added to the reactor. After that, 15 mL of 20 mg $L^{-1}$ of indigo carmine dye and 0.7 mL of 30 % $H_2O_2$ were added to the dispersion in order to obtain a dye concentration of 10 mg $L^{-1}$. Then, the magnetic stirring was turned on and the suspension was kept stirring in the dark for 30 min. to ensure the dye-catalyst adsorption equilibrium. To start the photocatalysis tests, the UV lamp was turned on and aliquots of approximately 2 mL were withdrawn from the reaction medium at regular intervals. Soon after, the composite was magnetically separated with a magnetic bar, and then filtered with a Millipore filter (MILEX-GV PVDF) 0.22 µm. Finally, the aliquots were analyzed in a Varian Cary 500 UV-vis spectrometer (which previously generated a calibration curve with different concentrations of indigo carmine dye solutions), at 611 nm (Figures A1 and A2). The discoloration of indigo carmine was calculated as shown in Equation 1. For the reuse experiment, the recovered composite was washed with water, dried during 30 min in oven at 100 ºC and used in the next photocatalysis reaction.

$$\boldsymbol{Discoloration}\ (\%) = \frac{(C_0 - C_A)}{C_0}\ x\ 100 \qquad (1)$$

Where, $C_A$ is the calculated concentration of the specific aliquot and $C_0$ is the initial concentration of indigo carmine dye.

## 1.3 Results and discussion

SEM and FESEM images were obtained in order to compare the morphologies of the materials studied in this work. Graphene oxide (GO) morphology is similar to sheets with wrinkles and folds, which is due to the interaction of oxygen groups present on the surface (Soares, 2018) (Figure 1). Both reduced graphene oxide (RGO) (Figure 2) and $Fe_3O_4$/RGO composite (Figure 3 and 4) showed sheet-like shapes. The composite morphology suggests

that $Fe_3O_4$ oxide is highly dispersed on the RGO surface, which should indicate a large surface area. Literature reports values of specific surface area varying from 100 to 400 $m^2g^{-1}$ (Qiu *et al.*, 2016; Ferreira *et al.*, 2020; Babu *et al.*, 2017). According to the results of Qiu et al (2016), whose method of synthesis was used in the present work, it was obtained a composite with 199 $m^2$ $g^{-1}$. In a recent work, our group obtained 177 $m^2$ $g^{-1}$ as the specific surface area for GO/γ-$Fe_2O_3$ with a Fe-oxide/GO mass ratio of 9, similar mass ratio to that obtained in the present work (Ferreira *et al.*, 2020). Therefore, we can expect similar specific surface area values to the aforementioned works.

Figure 1 – SEM image of GO

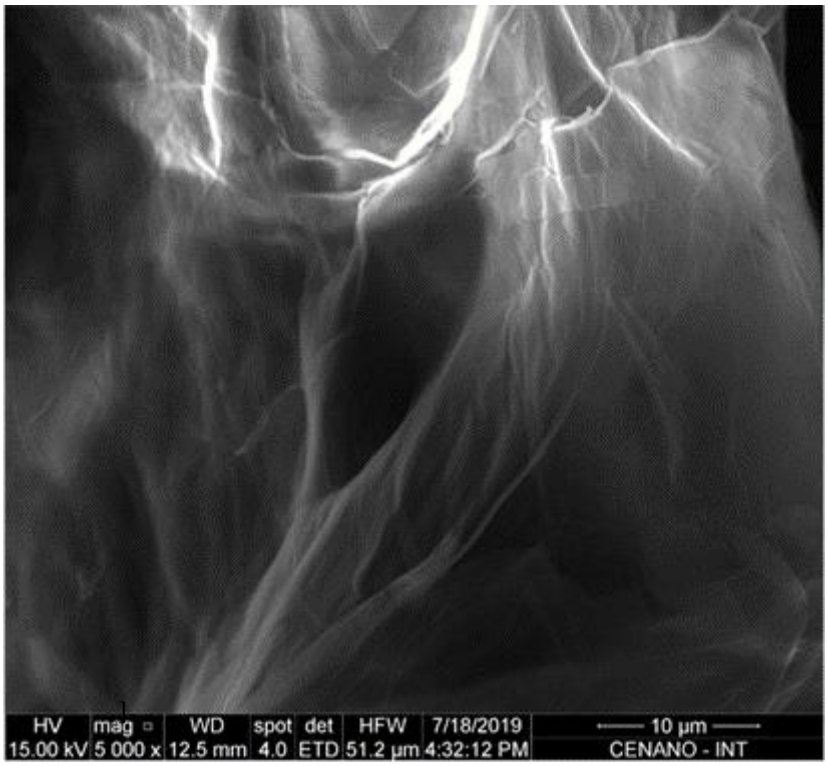


Source: The author, 2020.

Figure 2 – FESEM image of RGO.

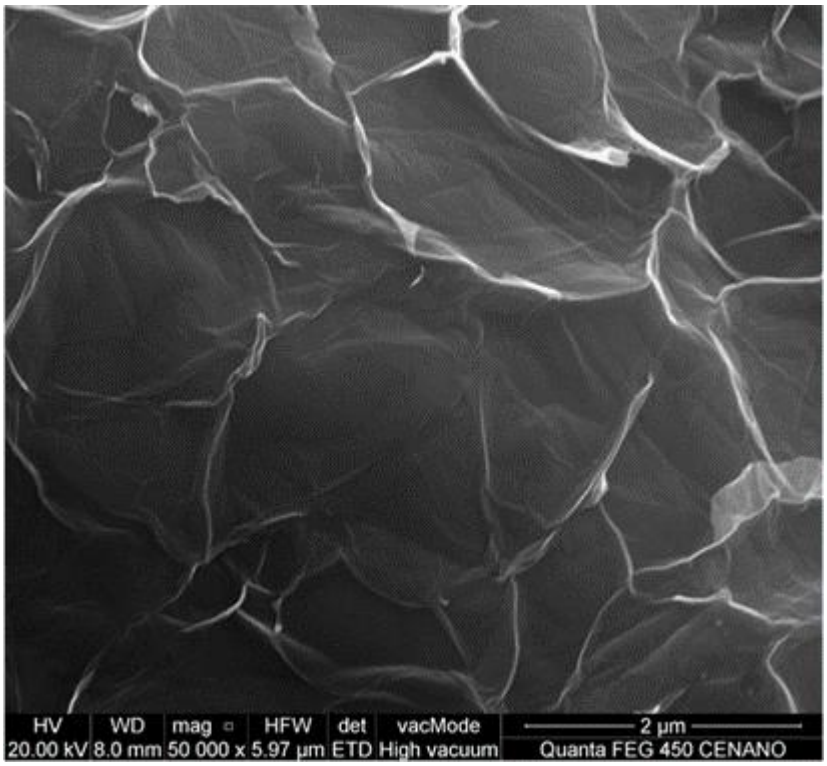


Source: The author, 2020.

Figure 3 – SEM image of $Fe_3O_4$/RGO.

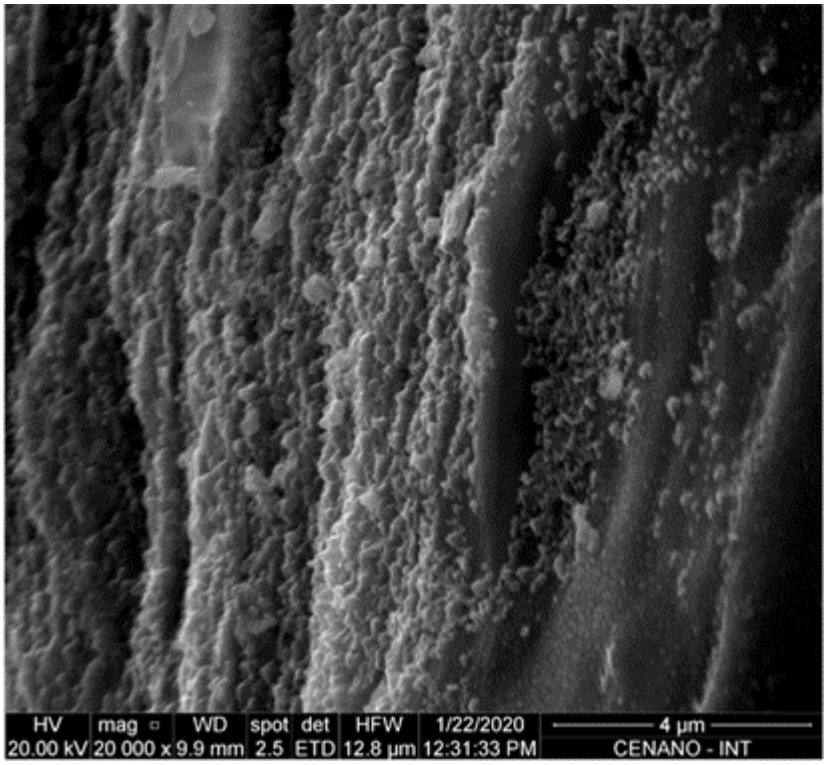


Source: The author, 2020.

Figure 4 – FESEM image of $Fe_3O_4$/RGO.

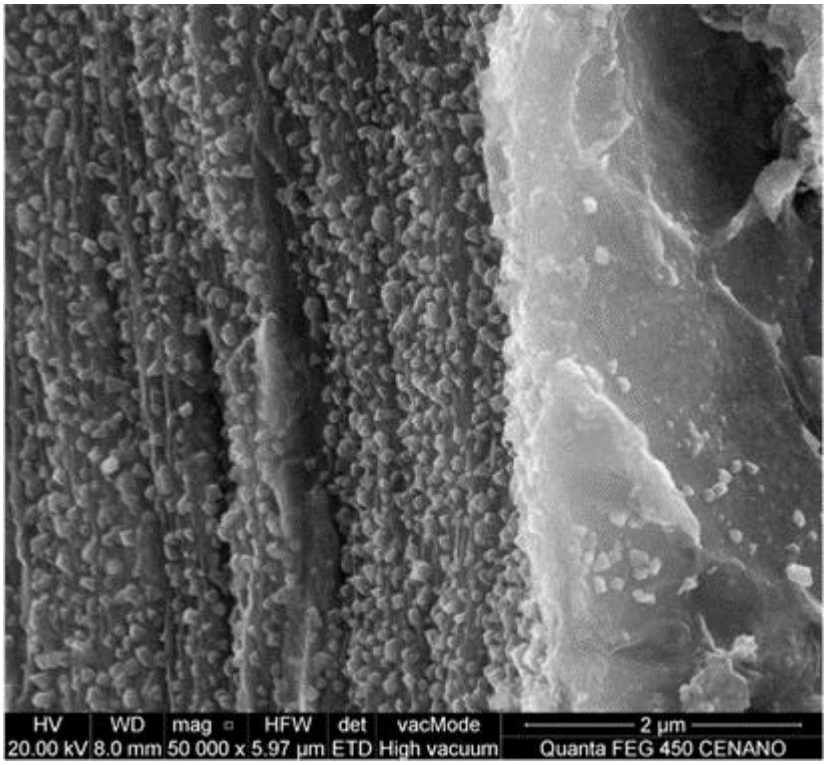


Source: The author, 2020.

Figure 5 – FESEM -EDX mapping of $Fe_3O_4$/RGO.

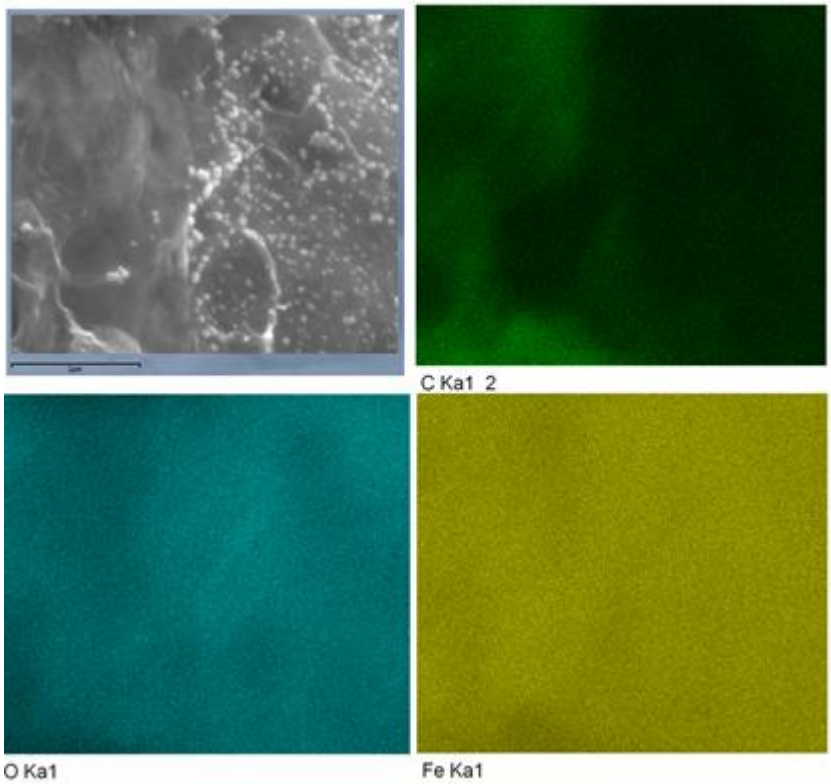


Source: The author, 2020.

Figure 6 – FESEM -EDX composition of $Fe_3O_4$/RGO.

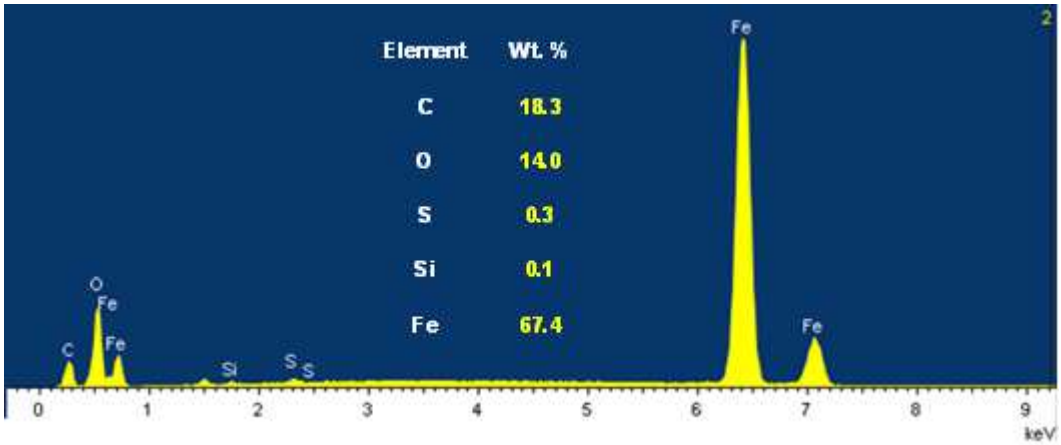


Source: The author, 2020.

By analyzing the composite FESEM image (Figure 4), it is possible to note that iron particles were anchored on the reduced graphene surface. FESEM-EDX mapping of $Fe_3O_4$/RGO composite is shown in Figure 5. Iron and oxygen maps show that these elements are well dispersed on RGO sheets. The composite presented 67.4 wt.% Fe equivalent to 93.2 wt.% $Fe_3O_4$, according to semi-quantitative FESEM-EDX composition analysis as displayed in Figure 6. The other elements were C 18.3 wt.%, O 14.0 wt.% and traces of Si and S as impurities. However, the analysis of oxygen is impaired because there is an overlap with iron as shown in the Figure 6.

Figure 7 shows the XRD patterns for the parent graphite and the prepared samples (GO, RGO, and $Fe_3O_4$/RGO). The pristine graphite presents the sharp peak characteristic of graphite (002) at $2\theta = 26.5^o$ (d-spacing = 3.361 Å, JCPDS 75-2078). Upon oxidation of graphite to graphene oxide (GO), this peak disappears, and a peak at $2\theta = 10.4^o$ (d-spacing = 8,500 Å, JCPDS 41–1487) is observed, which characterizes the formation of a lamellar structure and confirms the oxidation of graphite to graphene oxide (GO) (Johra *et al.*, 2014; Rufuss *et al.*, 2017). The increase in the d-spacing can be associate with the formation of oxygen-containing functional groups and the presence of water molecules between the interlayer space of GO (Shalaby *et al.*, 2015). After the treatment at 500ºC, under $N_2$ flow, it is observed a halo at $2\theta = 25.2^o$, corresponding to d spacing of 3.532 Å, while the former peak disappears, which is characteristic of the GO reduction and formation of reduced graphene oxide (RGO) (Zhao *et al.*, 2012; Haneef *et al.*, 2017). The d-spacing of RGO, close to that of the parent graphite, and disappearance of peak at $2\theta = 10.4^o$ suggest that oxygen-

containing groups of graphite oxide were efficiently removed (Shalaby *et al.*, 2015). The XRD pattern for the synthesized composite shows crystalline $Fe_3O_4$ peaks at 29.9º (220), 35.4º (311), 43.1º (400), 56.9º (511), and 62.5º (440) [JCPDS 76-1849]. It is not possible to observe the peak characteristic of RGO, probably because of the high quantity of crystalline $Fe_3O_4$, as discussed elsewhere (Boruah *et al.*, 2017) . In parallel, the $Fe_3O_4$ diffraction peaks showed high Full Width at Half Maximum (FWHM) values, suggesting that $Fe_3O_4$ particles are in the order of nanometers (Yao *et al.*, 2012). This was confirmed by the $Fe_3O_4$ crystallite size estimation at $2\theta = 35.4º$, calculated by the Scherrer's equation for the plan (311), which was equal to 21 nm.

Figure 7 – XRD patterns for graphite, GO, and $Fe_3O_4$/RGO.

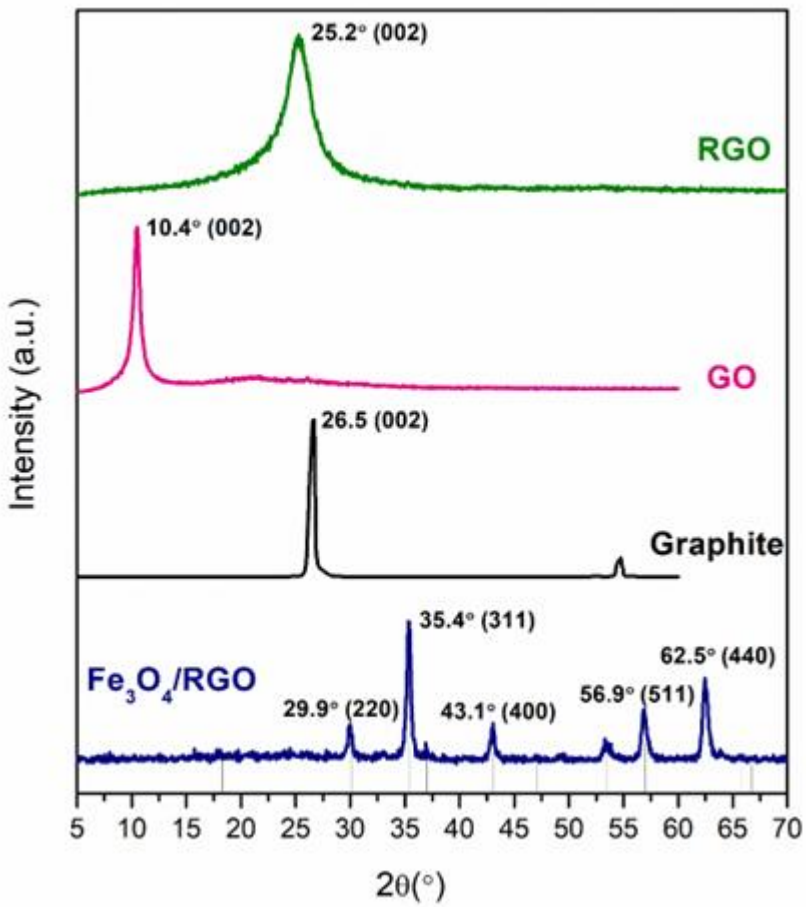


Source: The author, 2020.

TGA analysis is shown in Figure 8. The TGA profile for GO shows a considerable weight loss up to 200 ºC, which was attributed to thermal desorption of water. A drastic loss starting at around 210 ºC can be related to the oxygen functional groups elimination (Shen *et al.*, 2010). After that, the graphitic substrate decomposition is observed starting in temperatures above 450 ºC (Kim *et al.*, 2017). RGO also presented an adsorbed water weight

loss up to 200 ºC, although in a lower proportion than the observed for GO. The further weight loss for RGO (starting around 500 ºC up to 800 ºC) corresponds to the graphene sheets combustion as observed elsewhere (Qiu *et al.*, 2016; Boruah *et al.*, 2017; Fan *et al.*, 2013; Hu *et al.*, 2016). These results clearly show that RGO presents higher thermal stability than GO (Shen *et al.*, 2010). $Fe_3O_4$/RGO composite presented a slight weight gain in the range of 200-350 ºC, which can be attributed to the $Fe_3O_4$ oxidation to $Fe_2O_3$ (Kim *et al.*, 2017; Latorre-Sanchez *et al.*, 2012). The maximum weight losses up to 1000ºC for RGO and Fe3O4/RGO were 95 % and 10 %, respectively. Therefore, by calculating the total $Fe_3O_4$/RGO weight loss summed to the remaining RGO weight after 1000ºC, the estimated $Fe_3O_4$ content in the composite was 85 %, which is in good agreement with the semi quantitative FESEM-EDX analysis.

Figure 8 – TGA curves for GO, RGO, and $Fe_3O_4$/RGO.

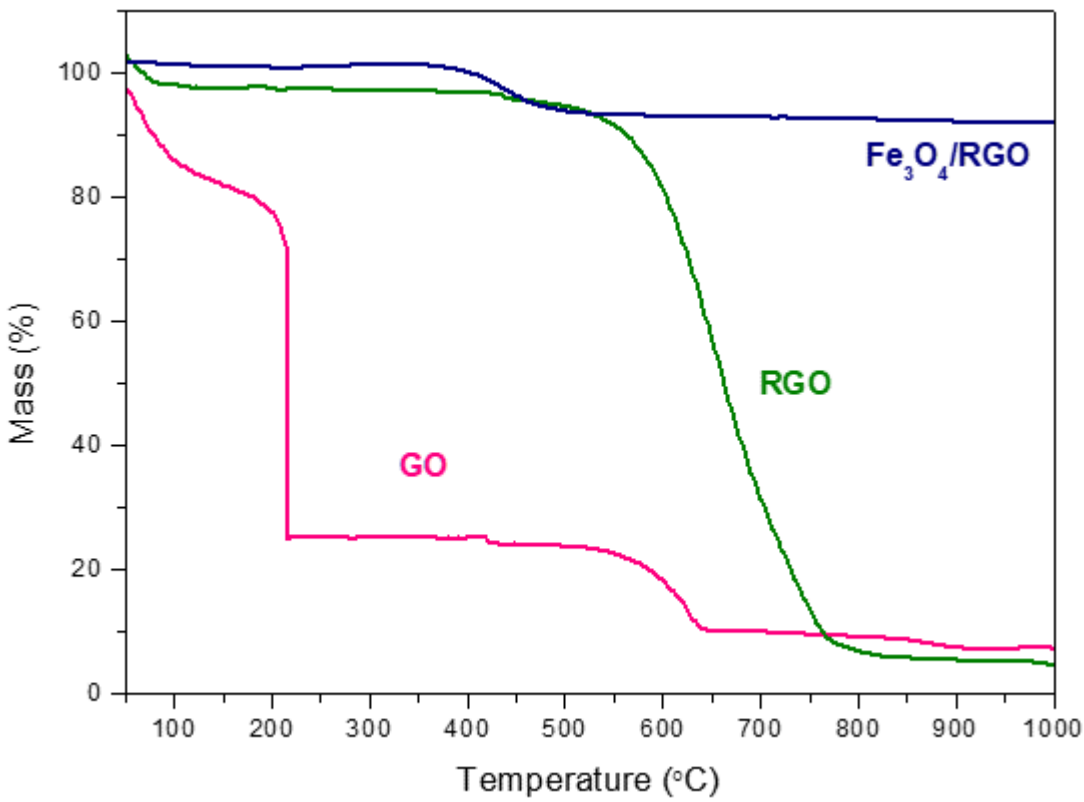


Source: The author, 2020.

LRS analyses are shown in Figure 9 and 10. The major differences between graphite and GO Raman spectra are the appearance of the D band in GO spectrum, which is associated to the disorder of the graphite edges; the broadening in D and G bands; and the Raman shift of

the G band of GO toward higher wavenumbers, due to isolated double bonds. Figure 9 also shows the RGO Raman shift spectrum. ID/IG ratio did not show difference between GO and RGO samples (both presented an ID/IG ratio of 0.99). However, the G band shift toward lower wavenumbers in RGO indicates the exfoliation of GO sheets (Kudin *et al.*, 2008; Choi *et al.*, 2011). Figure 10 shows the Raman spectrum for $Fe_3O_4$/RGO composite. The peaks in the range of 200-650 $cm^{-1}$ are related to the magnetite oxidation to hematite during the Raman analysis (Beattie; Gilson, 1970); while the band at ~680 $cm^{-1}$ confirms the $Fe_3O_4$ formation (See, *et al.*, 2014; Verble, 1974; Shebanova; Lazor, 2003). It is also important to note that G band for the composite is virtually absent. This result is similar to that obtained by Boruah *et al.* (2017) and is an evidence that $Fe_3O_4$ is in higher proportions compared to RGO.

Figure 9 – Raman spectra: D and G band comparison between the carbonaceous materials.

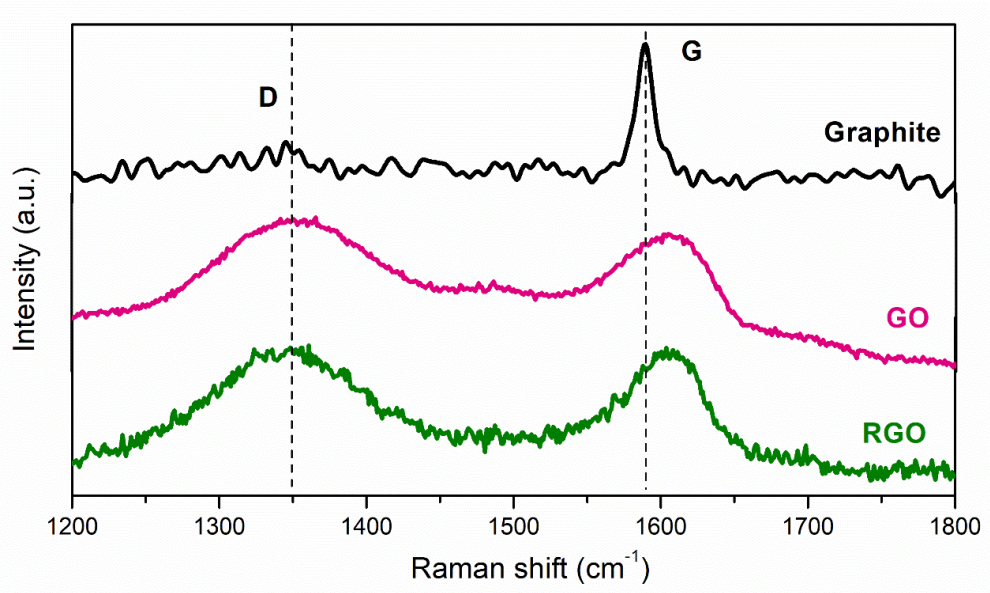


Source: The author, 2020.

Figure 10 – Whole Raman spectra comparison between $Fe_3O_4$/RGO, and RGO.

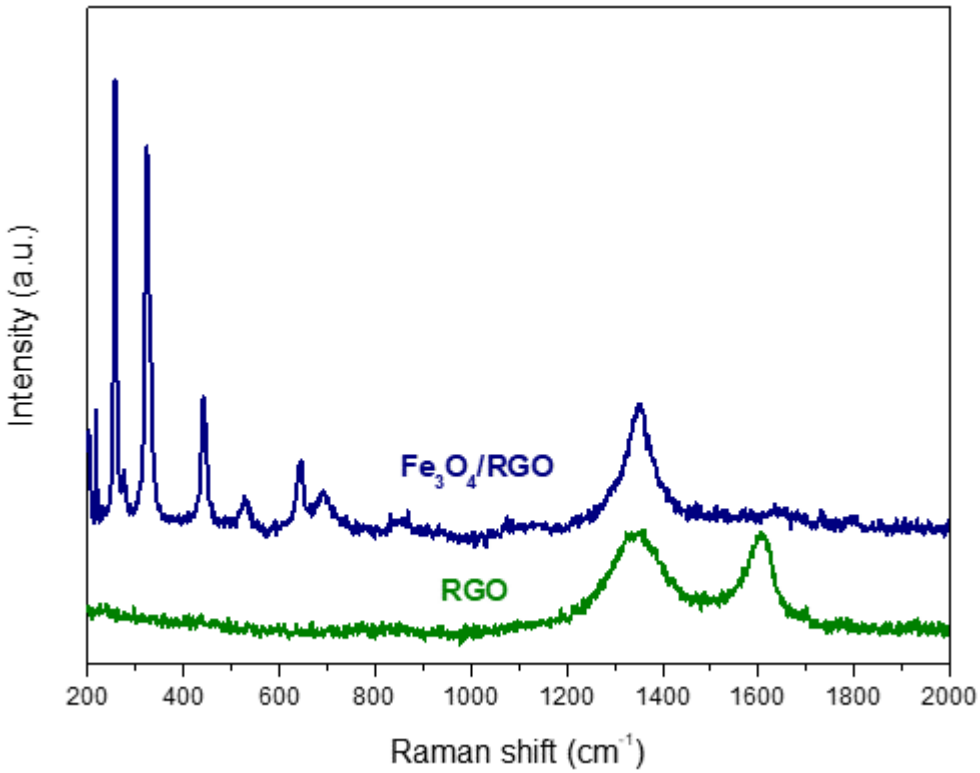


Source: The author, 2020.

The surface chemical investigation was performed by X-ray photoelectron spectroscopy (XPS). Figure 11 shows the survey spectra of the composite and the carbonaceous materials (GO and RGO) and Table 1 shows the surface O/C atomic ratio of the materials. The XPS O/C atomic ratio of GO and RGO was 0.33 and 0.16, respectively. These results demonstrate the surface oxygen removal during the thermal reduction. Survey spectrum of $Fe_3O_4$/RGO composite shows, besides the C1s and O1s peaks, the appearance of Fe2p, Fe3p, Fe2s, Fe3s, and FeLMM peaks indicating that iron was successfully anchored on the surface of graphene sheets. In parallel, after the composite synthesis, the O/C atomic ratio increased to 0.48 indicating the iron oxide formation on the RGO surface. C1s and O1s high-resolution spectra of GO, RGO, and $Fe_3O_4$/RGO are shown in Figure 12 and 13, respectively. As can be seen in Table 1, the deconvolution of C1s photoelectron peaks (Figure 12) shows that the peaks related to oxygen-bound carbon species notoriously reduced or disappeared for the RGO sample. A similar result was observed for the $Fe_3O_4$/RGO composite, at the same time that the O1s photoelectron peak of this sample (Figure 13) shifted toward lower binding energies [$BE_{O1s}$(GO) = 532.5 eV; $BE_{O1s}$($Fe_3O_4$/RGO) = 530.0 eV], indicating that surface oxygen is preferably bound to iron in this sample. O1s photoelectron region for the

$Fe_3O_4$/RGO composite could be deconvoluted in two peaks: 530.1 eV (iron-oxygen) and 532.4 eV (carbon-oxygen) (Madhuvilakku *et al.*, 2017), showing that reduced graphene oxide still has carbon-oxygen groups, although in minor proportions. $Fe2p_{3/2}$ high-resolution spectrum for $Fe_3O_4$/RGO composite is shown in Figure 14. In a study performed by Biesinger *et al.* (2011), which studied the peak fitting of various first-row transition metals compounds, iron showed to be the most complex. Therefore, the deconvolution of $Fe2p_{3/2}$ is, in many cases, not straightforward and requires attention. In the case of $Fe_3O_4$, which is both $Fe^{2+}$ and $Fe^{3+}$ high-spin mixed oxide, the multiplet-splitting concept should be used to obtain a reasonable fitting. The $Fe2p_{3/2}$ peak fitting residual for $Fe_3O_4$/RGO sample was 0.87 (calculated using CasaXPS software (CasaXPS, 2018)), indicating that the created peak model is satisfactory. The peaks related to $Fe^{2+}$ (A) and $Fe^{3+}$ (B) were: 708.7 eV (A1), 709.5 eV (A2), 710.5 eV (B1), 711.5 eV (B2), 712.6 eV (B3), 713.7 eV (B4), and 714.8 (B5), respectively. The calculated $Fe^{3+}/Fe^{2+}$ ratio was 1.9, agreeing either with Biesinger et. al. (2011) that found a $Fe^{3+}/Fe^{2+}$ ratio of 1.7 and the theoretical, which is 2.

Figure 11 – XPS survey spectra for GO, RGO, and $Fe_3O_4$/RGO.

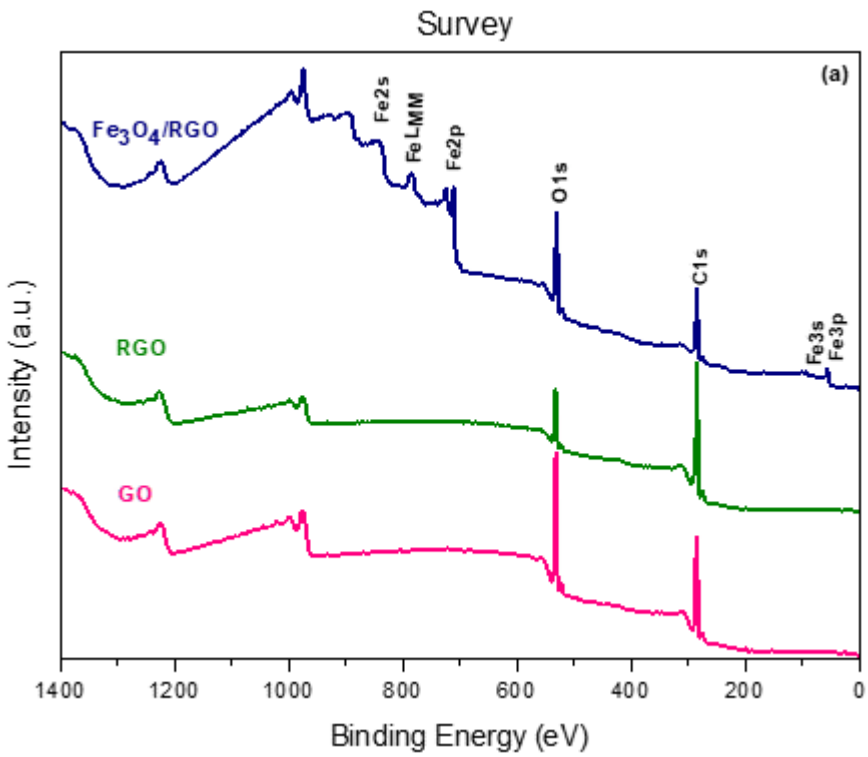


Source: The author, 2020.

Figure 12 – XPS C1s spectra for GO, RGO, and $Fe_3O_4$/RGO.

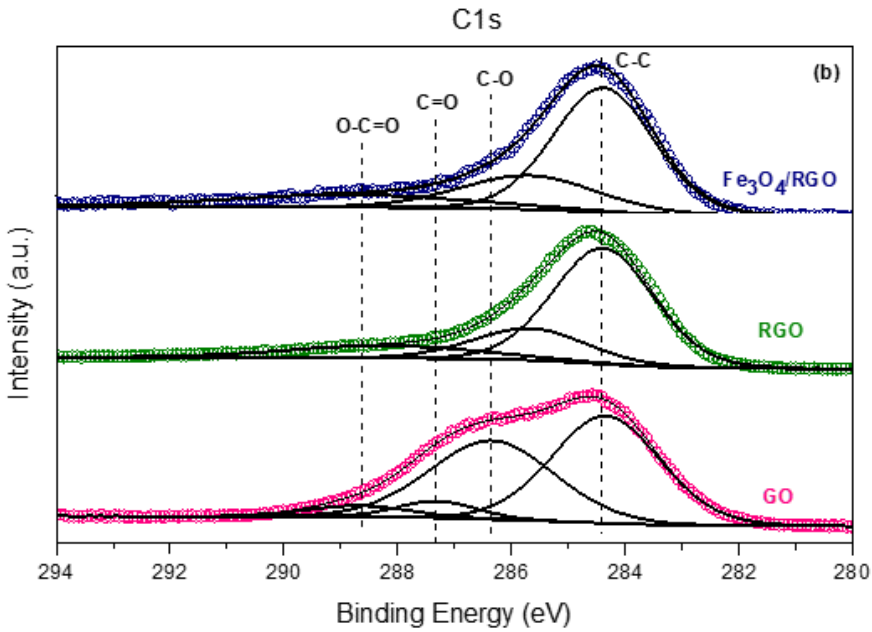


Source: The author, 2020.

Figure 13 – XPS O1s spectra for GO, RGO, and $Fe_3O_4$/RGO.

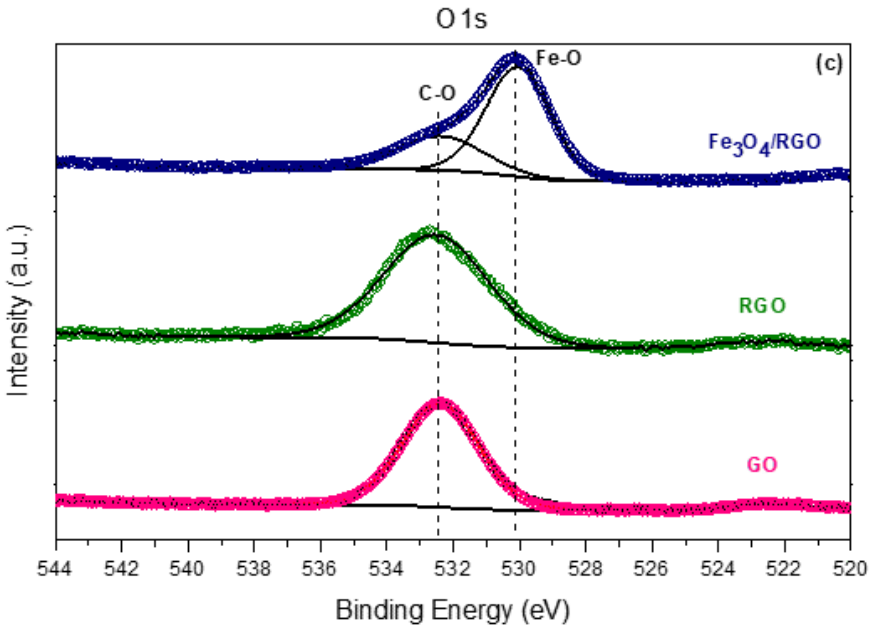


Source: The author, 2020.

Figure 14 – Fe2p spectrum peak fitting for $Fe_3O_4$/RGO.

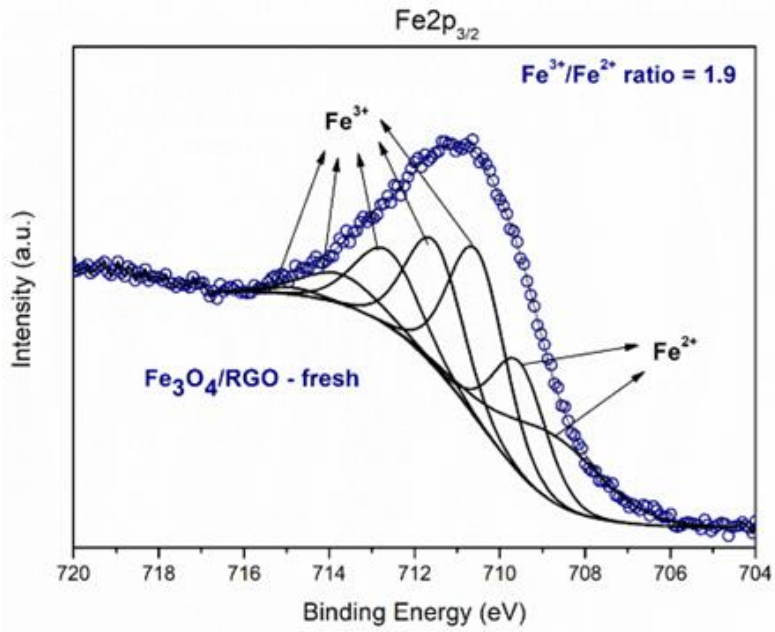


Source: The author, 2020.

Table 1 – Carbon species after C1s peak fitting.

| Sample | O/C atomic ratio | Carbon surface species (relative %) | | | |
|---|---|---|---|---|---|
| | | C-C | C-O | C=O | O-C-O |
| GO | 0.33 | 48.5 | 41.0 | 5.6 | 4.9 |
| RGO | 0.16 | 65.9 | 20.4 | - | 13.7 |
| $Fe_3O_4$/RGO | 0.48 | 61.9 | 23.0 | - | 15.1 |

Source: The author, 2020.

Bandgap energy for $Fe_3O_4$/RGO composite was estimated by using the DRS analysis, applying the Kubelka-Munk function (Kubelka; Munk, 1931), and following Tauc's method (Tauc *et al.*, 1966) to extrapolate the composite bandgap, is shown in Figure 15. The bandgap value found for the $Fe_3O_4$/RGO composite was 1.33 eV, characteristic of a semiconductor (Strehlow; Cook, 1973). Compared to the values obtained for $Fe_3O_4$ nanoparticles from other works (Ghandoor *et al.*, 2012; Kulkarni *et al.*, 2013), the value found in this study indicates a narrower bandgap, suggesting an RGO contribution, as observed by Agorku *et al.* (2015b). Huang *et al.* (2012) studied the bandgap values for different O/C ratios RGO by using Density Functional Theory. This author found that the most stable RGO configuration with a 0.17 O/C

ratio presented a narrow bandgap value of 1.14 eV. If compared to the XPS results, our composite presented a surface O/C ratio of 0.16. Thus, by associating XPS quantitative results with bandgap it is reasonable to suggest that the RGO is contributing to a narrower bandgap value, which indicates a $Fe_3O_4$-RGO interaction.

Figure 15 – Indirect bandgap determination for $Fe_3O_4$/RGO composite.

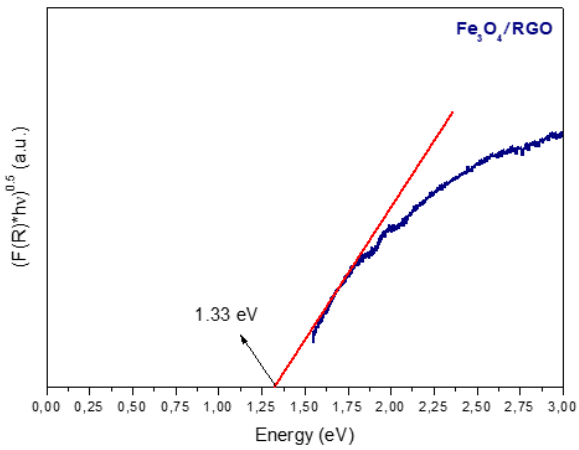


Source: The author, 2020.

Zeta potential was measured to compare the electrostatic characteristic between $Fe_3O_4$/RGO composite and RGO in an aqueous medium (Table 2). Zeta potential at pH = 6 for RGO and $Fe_3O_4$/RGO composite were -77.7 mV and -46.9 mV, respectively. Indigo carmine has two sulfonic groups ($SO_3^-$) that confer a negative character to this molecule. Therefore, the less negative the charges on the photocatalyst surface, the better the attraction between photocatalyst and indigo carmine dye (or lesser repulsion). Thus, $Fe_3O_4$ formation on RGO sheets suggests that the photocatalyst-dye interaction can be favored, as observed by Costa *et al.* (2019), which studied different ZnO-$Nb_2O_5$ mixed oxides for bromophenol blue dye photodegradation.

Table 2 – Zeta potential at pH=6 for RGO, and $Fe_3O_4$/RGO composite.

| Sample | Zeta potential (mV) |
|---|---|
| RGO | -77.7 |
| $Fe_3O_4$/RGO | -46.9 |

Source: The author, 2020.

Figure 16 shows the magnetic analysis for $Fe_3O_4$/RGO composite. The composite has a ferromagnetic character with a saturation magnetization of 43 emu/g. The remanence and coercivity are presented by the inset in Figure 16. The values obtained are 11 emu/g and 155 Oe, and they agree with those previously observed for $Fe_3O_4$/graphene and coercivity is nearby the known values of $Fe_3O_4$, 115-150 Oe (Jiang *et al.*, 2017; Arshad *et al.*, 2018; Qin *et al.*, 2014).

Figure 16 - Magnetization M as a function of magnetic field H at 300K. The inset shows the enlarger view of magnetization curve at low magnetic field region.

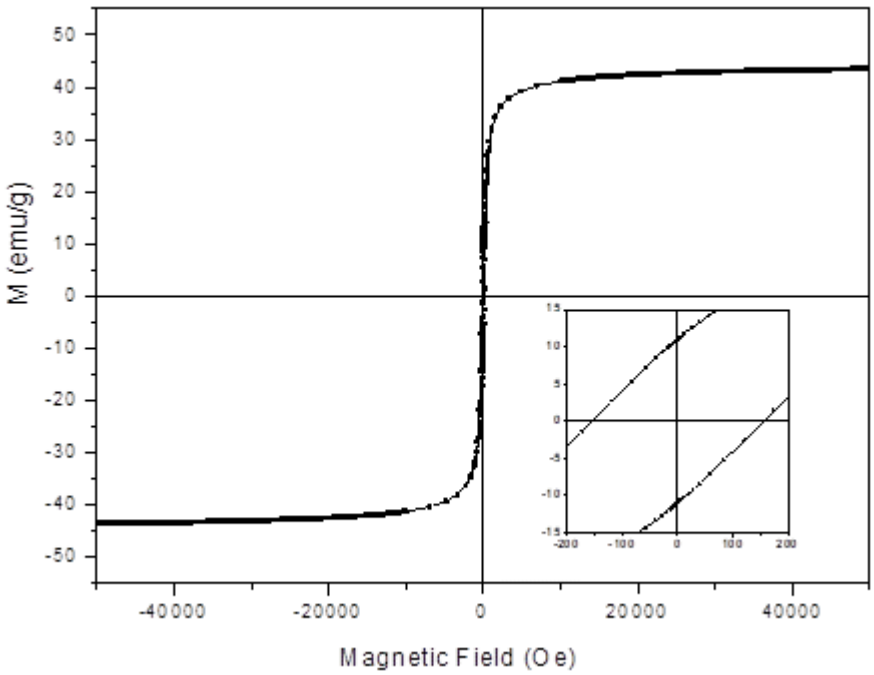


Source: The author, 2020.

The discoloration of indigo carmine is shown in Figure 17. No indigo carmine discoloration can be observed without $H_2O_2$ and the catalyst. When only $H_2O_2$ and UV were used, a discoloration of 71% was observed at 60 min, showing that photo-Fenton reaction of indigo carmine can occur even in the absence of a heterogeneous catalyst (Aleboyeh, *et al.*, 2003). With RGO, $H_2O_2$, and UV, the discoloration increased to 80% at 60 min, while the composite promoted total discoloration at 5 min. Figure 18 shows the UV-visible spectra of indigo carmine discoloration with the $Fe_3O_4$/RGO composite. Without UV lamp turned on (from -30min to 0min), the intensity of the peak at 611 nm decreased, corresponding to ~85% of discoloration, showing that the composite already adsorbs indigo carmine dye, probably due to the commonly high specific surface area of this type of material (Qiu *et al.*, 2016; Ferreira *et al.*, 2020; Babu *et al.*, 2017), and as suggested by FESEM results (Figures 3 and 4). Either Figure 17 or 18 show the rapid discoloration of indigo carmine, with the composite, after 5 min UV lamp was turned on. As highlighted in Figure 18, it is important to note that no sign of isatin-like molecules formation is observed around 241nm (Quartarone *et al.*, 2003), as observed elsewhere (Zaied *et al.*, 2011; Flox *et al.*, 2006; Ammar *et al.*, 2006). These results suggest that the catalyst degraded not only the indigo carmine dye but also its first degradation product (isatin sulfonic acid). The rapid indigo carmine discoloration in this study may be explained by the less negative zeta potential after $Fe_3O_4$ formation on RGO sheets, which is responsible for improving the attraction of indigo carmine molecule; the narrower bandgap value, showing that the composite demands less energy to start electron transfer; and the $Fe^{3+}/Fe^{2+}$ surface atomic ratio calculated by XPS. Qiu et al (2016) compared a commercial $Fe_3O_4$ powder with a $Fe_3O_4$/RGO composite in methyl orange, methyl blue and rhodamine B photo-Fenton discoloration. It was observed that the composite showed superior activity compared to the bare $Fe_3O_4$ powder, even after the reuse cycles. This author attributed the superior composite photocatalytic activity to the persistence of the cycle conversion process of $Fe^{3+}/Fe^{2+}$, while the bare $Fe_3O_4$ quickly forms $Fe(OH)_3$, thus deactivating the catalyst. The $Fe^{3+}/Fe^{2+}$ conversion cycle is extremely important to maintain the photocatalyst activity in photo-Fenton reactions because graphene can accept the electrons provided by magnetite and indigo carmine dye after UV light irradiation. The electron transfer from $Fe^{2+}$ to $Fe^{3+}$ allows $Fe^{2+}$ to react with $H_2O_2$ to generate the •OH radical that possesses a high oxidant character, which attacks the dye molecule. Simultaneously, graphene sheets supply the electrons to reduce the $Fe^{3+}$ to $Fe^{2+}$ and maintain the •OH radical production (Qiu *et al.*, 2016). Therefore, the surface $Fe^{3+}/Fe^{2+}$ atomic ratio by XPS is an important factor that can be used to explain the high activity of the composite.

Figure 17 – Indigo carmine discoloration in function of time.

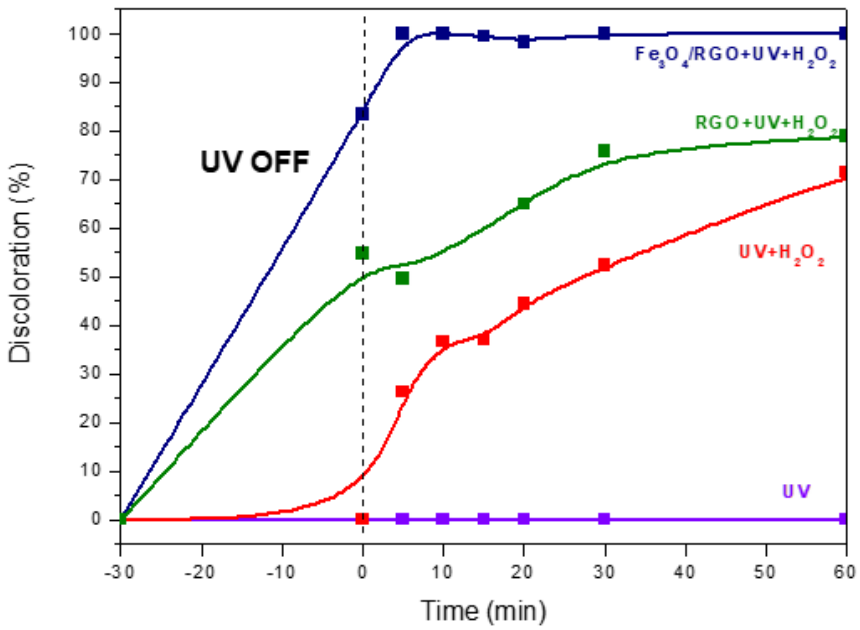


Source: The author, 2020.

Figure 18 – UV-Visible spectra of indigo carmine dye discoloration with $Fe_3O_4$/RGO composite.

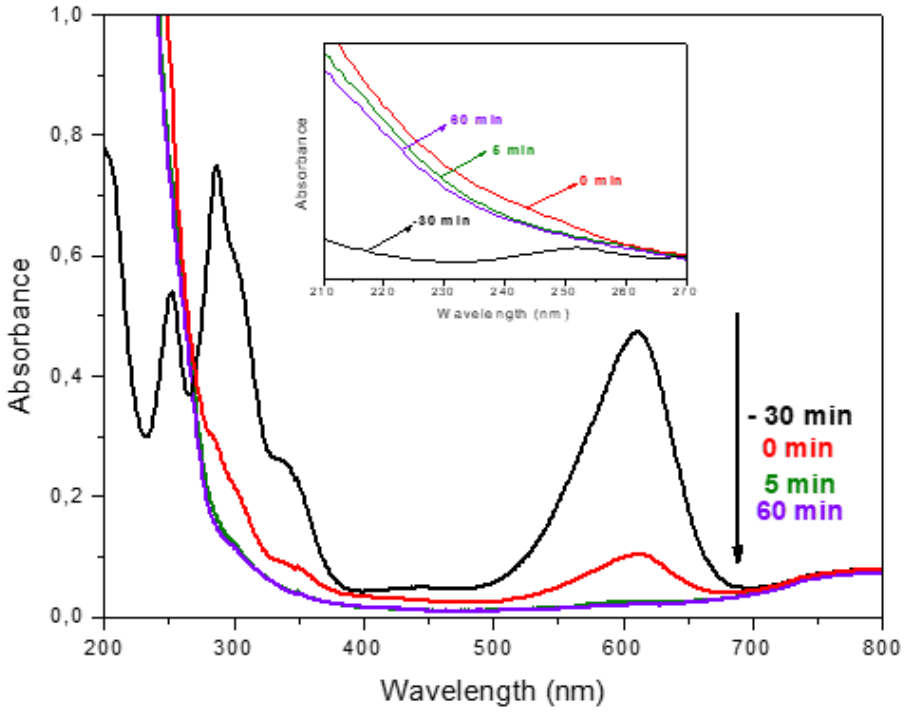


Source: The author, 2020.

Table 2 shows a compilation of some indigo carmine dye photocatalysis applying different materials. Cosme-Torres *et al.* (2019) used a natural clinoptilolite-heulandite type zeolite and obtained an indigo carmine discoloration up to 94% at pH = 3. Khanh *et al.* (2019) studied the indigo carmine discoloration with $ZnBi_2O_4$/RGO (2% of RGO) and achieved 91% of discoloration at pH = 6.3, after 75 min of reaction. This author observed, by photocurrent response analysis that RGO in the composite worked as a good electron acceptor, suppressing the electron-hole recombination promoted by UV light, thus increasing the indigo carmine discoloration. The other works listed in Table 3 also showed remarkable indigo carmine discoloration, yet by applying noble metals, adjusting the pH and using $O_3$ (Kurt *et al.*, 2016; Coelho *et al.*, 2010; Secula *et al.*, 2019). In the present study, however, there was no pH adjustment for the experiment (our photo-Fenton reactions were performed at pH=6), and the catalyst was easily separated from the reaction medium with a magnetic bar, as can be seen in Figure 19, which is an advantage if applied in large scale.

Table 3 – Compilation of different photocatalysts in IC discoloration.

| Catalyst | IC dye discoloration (%) | IC/cat mass ratio | Comments | References |
|---|---|---|---|---|
| $Fe_3O_4$/RGO | 100 (5 min) | 0.02 | 10%RGO/pH 6.0 | This work |
| Co-ZnS/RGO | 100 (180 min) | 0.02 | 0.3%Co/0.5%RGO | Agorku *et al.*, 2015a |
| Mn/$TiO_2$ | 90 (60 min) | 0.30 | pH 2.0 | Othman *et al.*, 2007 |
| Pd-ZnS/RGO | 100 (210 min) | 0.02 | 1.0%Pd/0.5%RGO | Agorku *et al.*, 2015b |
| ZeoSonFe zeolite | 94 (120 min) | 0.20 | pH 3.0 | Torres *et al.*, 2019 |
| $ZnBi_2O_4$/RGO | 91 (75 min) | 0.05 | pH 6.3/2% RGO | Khahn *et al.*, 2019 |
| Pt-graphene | ~75 (5 min) | 0.20 | - | Kurt *et al.*, 2016 |
| Sn/$Al_2O_3$ | ~100 (40 min) | 0.05 | 60% Sn/pH 5.0 | Coelho *et al.*, 2010 |
| Fe/AC | 100 (10 min) | 0.25 | pH 3.0/$O_3$ | Secula *et al.*, 2019 |

Source: The author, 2020.

Figure 19 – Illustrative picture of dye discoloration and magnetic separation.

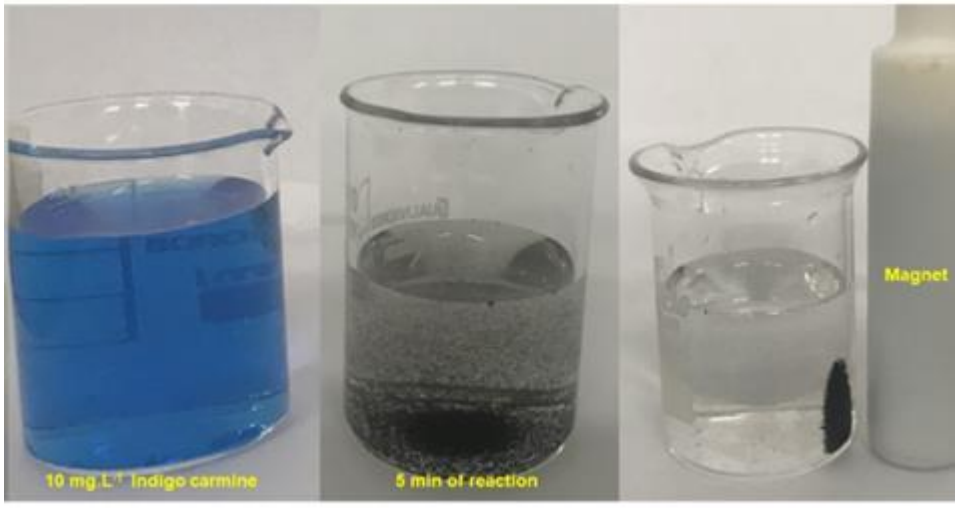


Source: The author, 2020.

To test the catalyst reuse, another reaction was performed with the recovered catalyst. Figure 20 shows that $Fe_3O_4$/RGO composite also reached total indigo carmine discoloration at 30 min of reaction. One concern about spinel catalysts preservation is that the reuse may lead to $Fe(OH)_3$ formation (Qiu *et al.*, 2016) and microphase separation (Yao *et al.*, 2014; Hong *et al.*, 2012), thus reducing the catalyst activity. An XPS analysis of $Fe2p_{3/2}$ was performed in order to observe iron oxidation state after reuse. Figure 21 shows the Fe2p3/2 spectrum deconvolution for the recovered $Fe_3O_4$/RGO composite after first cycle. The peaks related to $Fe^{2+}$ (A) and $Fe^{3+}$ (B) were: 708.9 eV (A1), 709.8 eV (A2), 710.8 eV (B1), 711.8 eV (B2), 712.9 eV (B3), 714.0 eV (B4), and 715.1 (B5), respectively. The calculated $Fe^{3+}/Fe^{2+}$ ratio was 1.9 (with a fitting residual of 0.87), which is the same that found for the fresh catalyst, indicating that after the first cycle, iron particles did not change their oxidation state. Furthermore, the surface $Fe^{3+}/Fe^{2+}$ atomic ratio suggests that the $Fe_3O_4$ spinel was preserved after first cycle, which can explain the remarkable indigo carmine dye discoloration in the second cycle. Hence, the $Fe_3O_4$ preservation is evidence of the beneficial interaction between graphene sheets and $Fe_3O_4$. These observations lead to a simpler system, with a potential catalyst for indigo carmine dye discoloration that can be reused without losing its activity in its first recycle, reducing the operation costs. Although the $Fe_3O_4$/RGO composite maintained its activity in the second indigo carmine dye discoloration cycle, further studies regarding its stability such as additional indigo carmine discoloration cycles and after test characterizations should be performed.

Figure 20 – Reusability of the $Fe_3O_4$/RGO composite.

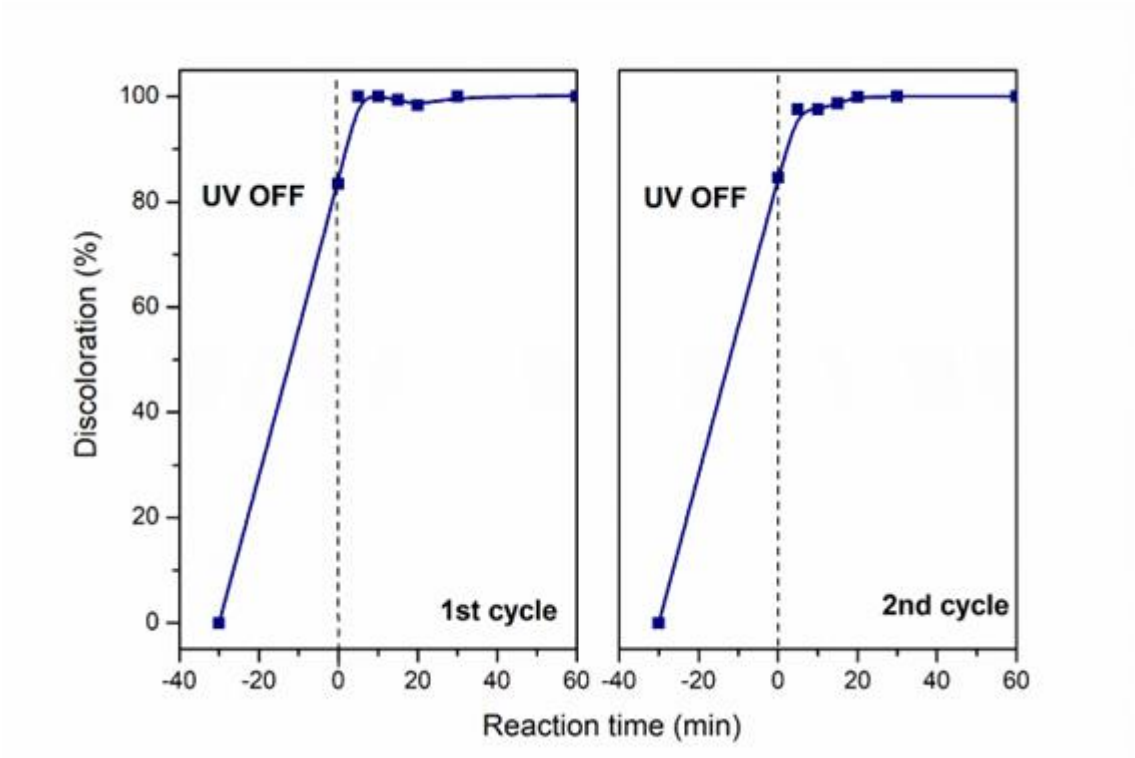


Source: The author, 2020.

Figure 21 – XPS Fe2p spectrum peak fitting for $Fe_3O_4$/RGO after the firs indigo carmine discoloration test.

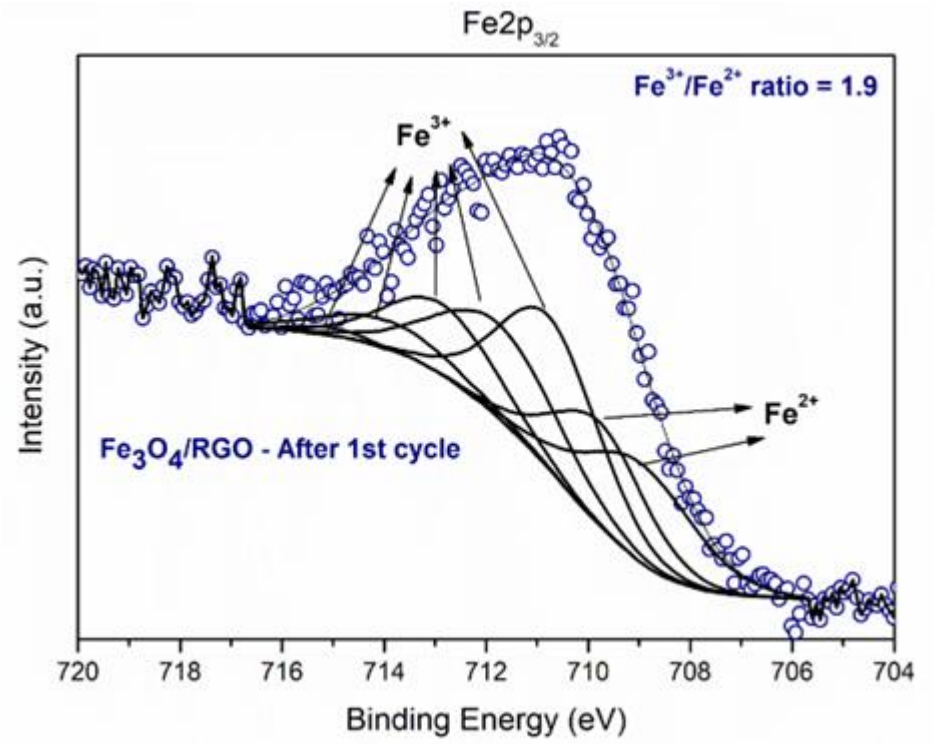


Source: The author, 2020.

## 1.4 Conclusions

In this work, a $Fe_3O_4$/RGO composite was synthesized and evaluated in the indigo carmine photo-Fenton discoloration. XRD, LRS, VSM and XPS analyses indicated that the facile synthesis, adopted in this work, lead to the successful high dispersed $Fe_3O_4$ formation on RGO sheets.

The photocatalytic tests for photo-Fenton discoloration of indigo carmine promoted by the $Fe_3O_4$/RGO composite showed promising results. By applying a catalyst with approximately 90% of magnetite, it was possible to reach total indigo carmine discoloration in the first 5 minutes of reaction, without pH correction before the tests, or any additional adjustment. The less negative zeta potential, narrow bandgap, and surface $Fe^{3+}/Fe^{2+}$ atomic ratio of the composite are three possible parameters that could explain the rapid indigo carmine discoloration.

Regarding the catalyst reusability, the composite was easily separated from the medium with a magnetic bar, and its reuse showed that the catalyst did not lose activity, reaching total discoloration of indigo carmine before 30 min of reaction in the second cycle. This outstanding activity in the second cycle could be explained by XPS results. $Fe2p_{3/2}$ spectrum showed that iron did not change its oxidation state, and the surface $Fe^{3+}/Fe^{2+}$.atomic ratio was maintained, indicating a $Fe_3O_4$ spinel preservation. This is evidence that the $Fe^{3+}/Fe^{2+}$ cycle was preserved during the first indigo carmine discoloration, showing that the catalyst could be used at least more than once without losing its activity.

In conclusion, the important aspects discussed hereby, show that the use of the $Fe_3O_4$/RGO composite as photocatalyst in the indigo carmine dye photo-Fenton discoloration is a promising approach that can be very active and reduce costs of dye contaminated wastewater remediation.

# 2 EFFECT OF FE3O4: RGO RATIOS IN MAGNETIC NANOCOMPOSITES APPLIED FOR DYE DISCOLORATION

In this paper, $Fe_3O_4$/RGO nanocomposites were synthetized as well as described in the first article but varying the $Fe_3O_4$:RGO ratios. Three photocatalysts were produced, characterized, and evaluated in the indigo carmine photo-Fenton discoloration. Aiming to complement the physical-chemical characterization of all nanocomposites, new techniques were included in this second paper: textural analysis, Scanning Transmission Electron Mode (STEM-in-SEM) Mössbauer spectroscopy, and Electronic Paramagnetic Resonance (EPR). All nanocomposites were magnetic but increasing the RGO content leads to a decrease in their ferromagnetic character. Also, the addition of RGO results in narrower band gaps values for all nanocomposites, when compared to the bare $Fe_3O_4$. The nanocomposite with the highest $Fe_3O_4$ amount presented the best performance and was chosen to perform reusability tests. In this case, compared to the first paper, more recycling tests were performed. It is worth mentioning that the term "composite" used in Chapter 1 was modified to "nanocomposite" when referring to the $Fe_3O_4$/RGO materials synthesized hereby, without compromising is meaning.

## 2.1 Introduction

Water contamination is one of the major environment-related issues, and it is associated not only with health problems, but with severe socioeconomic impacts (Mathur *et al.*, 2005; Alcocer *et al.*, 2018; Gioia *et al.*, 2018; Selvaraj *et al.*, 2020). It is estimated that around 10,000 different synthetic dyes (Shanker *et al.*, 2017) are used, with significant losses of these compounds to the environment after dyeing procedures (Achieng *et al.*, 2021). Indigo carmine (IC) is an artificial vibrant blue dye, spread worldwide due to its use in denim making. It is an indigoid organic dye and possesses two sulfonic groups. Besides, it is well known that IC brings high health risks because it is toxic, mutagenic, and very stable in nature (Younes, 2013). These characteristics are driving forces to develop new technologies to mitigate water pollution by synthetic organic dyes.

Different techniques are investigated to remediate dying wastewater pollution, such as ultrafiltration, electrochemical, and adsorption (Dastgerdi *et al.*, 2019). However,

heterogeneous photocatalysis of organic dyes emerges as a promising approach due to its advantages, such as catalyst recovery and reuse, use in mild conditions, pollutant chemical transformation and others (Zaied *et al.*, 2011; Barka *et al.*, 2008). These reactions are considered advanced oxidative processes (AOPs), where hydroxyl radicals (•OH) are generated from $H_2O_2$ decomposition, assisted by a light source and a semiconductor oxide (Al Kausor; Chakrabortty, 2021). These structures are then responsible for attacking the organic pollutant molecules, breaking the molecule bonds until mineralization (transforming a pollutant organic molecule into $CO_2$, $H_2O$, and mineral acids).

An attractive abundant semiconductor oxide studied in heterogeneous photocatalysis reactions is magnetite ($Fe_3O_4$) (Khan *et al.*, 2019). This mixed oxide has a $Fe^{3+}/Fe^{2+}$ ratio of 2:1, and narrow bandgap values (Radón *et al.*, 2017; Ghandoor *et al.*, 2012). The first characteristic is responsible for the aforementioned •OH radicals generation. The second, is related to the compound electronic activation, an important parameter to be considered in photocatalysts (Sakar *et al.*, 2019). However, if non-supported iron oxides are employed in water medium, its particles tend to aggregate quickly (Kong *et al.*, 2019). Also, the $Fe^{2+}$ oxidation to $Fe^{3+}$ results in a deactivated oxide passive layer (Gonçalves *et al.*, 2020). Both phenomena are bound to the •OH generation suppression, hindering the capability of decomposing the pollutant. Therefore, supporting iron nanoparticles in materials that stabilize them and improve their physical-chemical properties is a good alternative to mitigate these issues (Zheng *et al.*, 2020).

Due to their remarkable optical (Bagri *et al.*, 2010), electronic (Zhu *et al.*, 2010) and textural (Zhao *et al.*, 2011) properties, graphene derived compounds, such as graphene oxide (GO) and reduced graphene oxide (RGO), have been used to immobilize semiconductor oxide particles, avoiding particle agglomeration, and for improving their photocatalytic activity in various organic dyes removal systems (Zheng *et al.*, 2020; Su *et al.*, 2021; Arshad *et al.*, 2018; Jiang *et al.*, 2017; Zarrabi *et al.*, 2022). For instance, Zarrabi *et al.* (2022) produced a ZnO-GO-$Fe_3O_4$ nanocomposite and achieved 97% of methylene blue (MB) discoloration. Yet for this dye, Umar *et al.* (2022) obtained 91% of conversion within 30 min of reaction, with a $Fe_3O_4$-GO nanocomposite. For methyl orange dye (MO), Liu *et al.* (2023) synthesized an organic-inorganic PGO-$TIO_2$/$Fe_3O_4$, reaching 95% of MO removal. Using a monolithic 3D RGO-$Fe_3O_4$ aerogel, Sadegh *et al.* (2020) observed 100% of acid red 1 (AR1) dye discoloration. Silva *et al.* (2021) tested an amino-$Fe_3O_4$ functionalized graphene oxide, named AmGO, and observed 97% of reactive black 5 (RB5). Besides their remarkable dye removal results, another important highlight reported by these works is that these nanocomposites can

be simply synthesized by diverse approaches. In addition, the magnetic character of these nanocomposites leads to simpler catalyst recovery methods and possibilities for further reuse. Thus, the combination of these features results in promising materials to be used for a wide range of wastewater pollutants removal.

Recently, our group described dispersed $Fe_3O_4$ nanoparticles anchored on RGO sheets (Gonçalves *et al.*, 2020), synthesized by a facile synthesis adapted from the Stöber method (Qiu *et al.*, 2017), where $Fe(NO_3)_3.9H_2O$ oxidates to $Fe_3O_4$ and GO is reduced to RGO. In this way, a nanocomposite with approximately 90%wt of $Fe_3O_4$ and 10%wt of RGO was employed to treat an IC solution (2.1 x $10^{-5}$ M) in a photo-Fenton system. Within 5 min after the light was turned on, a rapid and complete discoloration of the IC solution was observed. Its remarkable characteristics such as: less negative zeta potential, narrow bandgap, and the persistent cycle conversion process of $Fe^{3+}/Fe^{2+}$ promoted by RGO; explained its outstanding activity. Furthermore, due to its strong magnetic character, the nanocomposite could be easily recovered and reused. These observations supported that the Stöber-like method is a powerful synthesis to immobilize $Fe_3O_4$ nanoparticles on RGO, improving its photocatalytic properties.

In this sense, the present work aims to expand the study of IC photo-Fenton discoloration with $Fe_3O_4$/RGO nanocomposites produced by the adapted Stöber-like method. Nanocomposites with different ratios of $Fe_3O_4$:RGO were synthesized, characterized, and evaluated in the IC photo-Fenton discoloration. The nanocomposite with the best performance was selected to perform a study varying the oxidant reactant ($H_2O_2$), and nanocomposite loads, providing kinetic data. Furthermore, reusability tests were conducted to highlight the photocatalyst stability.

## 2.2 Materials and Methods

### 2.2.1 Synthesis of the materials

Graphite (Grafine 996100), provided by Nacional de Grafite (São Paulo, Brazil) was oxidized by the modified Hummers method (Soares *et al.*, 2018). At 0 ºC, assisted by an ice bath, 11,5 mL of $H_2SO_4$ (95 wt.%, Vetec, Rio de Janeiro, Brazil), 270 mg of $NaNO_3$ (98 wt.%, Isofar, Rio de Janeiro, Brazil) were added to 220 mg of graphite under magnetic

stirring. Then, the temperature was set to 35 ± 5 ºC and six portions of 250 mg of $KMnO_4$ (99 wt.% were slowly added into the mixture, which remained stirring for 1 h. After that, distilled water was added, and the temperature was raised to 98º ± 5 ºC and kept for 15 min. Next, 60 mL of $H_2O_2$ (10 wt.%, Isofar, Rio de Janeiro, Brazil) were added to the system, and the temperature was lowered to 20 ºC and maintained for 1 h. After the oxidation procedure, the slurry was washed to remove impurities. Each washing cycle was performed as follows: the slurry was filtered and the solid obtained was washed with 20 mL of $H_2O_2$ (10 wt.%), then with 20 mL of $H_2SO_4$ (5 wt.%), centrifuged, and washed with distilled water until pH=6.0.

The synthesis of the $Fe_3O_4$/RGO magnetic nanocomposites was performed by varying the iron precursor solution concentration in the adapted Stöber-like method (Qiu *et al.*, 2016). In a beaker, an ethanol/acetonitrile (3:1) solution was used to disperse 200 mg of GO for 90 min in an ultrasonic bath. After that, the beaker was placed on a magnetic plate, 1.33 mL of ammonium hydroxide (28 wt.%, Sigma-Aldrich, São Paulo, Brazil) was added, and the suspension stirred for 30 min. The desired solutions of $Fe(NO_3)_3.9H_2O$ (Sigma-Aldrich, São Paulo, Brazil) were added dropwise to the suspension and kept stirring for 30 min. Then, the mixture was transferred to a round bottom glass flask and a reflux system was assembled. The temperature was set to 60 ºC, and the mixture was magnetically stirred for 40 h. At the end of this step, the iron oxide/GO solid was centrifuged from the solution, washed with ethanol to remove impurities, and dried in an oven. The iron oxide/GO solid was then heated to 500 ºC (with a rate of 1.5 ºC $min^{-1}$) and treated for 2 h with a pure nitrogen flow of 50 mL $min^{-1}$. Table 4 shows the precursor $Fe(NO_3)_3.9H_2O$ quantities used in each synthesis, and the respective names of the prepared samples. Also, an appropriate mass of GO was separated, and thermally treated as the iron oxide/GO likewise to yield pure RGO. A sample of bulk $Fe_3O_4$ obtained as described by Da Costa *et al.* (2019) was also used as a standard.

Table 4 – Nanocomposites nomenclatures, iron precursor contents, and approximate mass ratio of the precursors.

| Material | $Fe(NO_3)_3.9H_2O$ mass (g) | $Fe(NO_3)_3.9H_2O$ : GO[a] |
|---|---|---|
| Nanocomposite 1 | 1.1260 | 6:1 |
| Nanocomposite 2 | 2.2510 | 11:1 |
| Nanocomposite 3 | 3.3760 | 17:1 |

[a] Approximate mass ratio

Source: The author, 2023.

### 2.2.2 Characterization

Microscopic studies of the iron oxide nanoparticles of the $Fe_3O_4$/RGO nanocomposites were performed using Scanning Transmission Electron mode on a SEM microscope (STEM-in-SEM) operated at 30 kV, with a specific sample holder for conventional copper TEM grids and a high angular STEM detector (HAADF-STEM) in a Helios Nanolab Dual Beam G3 CX equipment. Field Emission Gun Scanning Electron (FE-SEM) analysis was carried out in a Quanta FEG 450 equipment. Both microscopes are from FEI/Thermo Fischer. C, O, and Fe distribution and composition in the $Fe_3O_4$/RGO nanocomposites were determined by Electron Dispersive X-Ray (FE-SEM-EDX). Particle size measurements were performed using Image J (1.52a) software. The crystallinity of all materials was observed by X-Ray Diffraction (XRD).

The diffractograms were obtained in a Rigaku Miniflex II, with CuKα radiation of 1.540562 Å, 30 kV voltage, and 15 mA current. The acquisition parameters were: 2θ (from 5 º to 70 º), a step of 0.05 º, and 2 º.min$^{-1}$ per step.

Textural analysis of RGO and the nanocomposites was performed in an ASAP 2020 from Micromeritics. Specific areas and pore volumes were estimated by $N_2$ adsorption at -196 ºC, using BET method for the estimation of the specific area, and BJH method for the estimation of the average pore diameter.

The thermal stability of the materials was investigated using Thermo Gravimetric Analysis (TGA), which the measurements were performed in a STA 409 Pc Luxx (NETZSCH) equipment, from room temperature to 1000 °C with a 20 °C min$^{-1}$ heating rate and 20 mL min$^{-1}$ of airflow.

Diffuse Reflectance Spectroscopy (DRS) was performed to estimate the bandgap of the nanocomposites and bulk $Fe_3O_4$. The materials were mixed with $BaSO_4$ (1:25) and analyzed in a Varian Cary 5000 UV-Vis-NIR spectrometer from 200 nm to 1500 nm.

The magnetic properties of the $Fe_3O_4$/RGO nanocomposites were studied by combining Electronic Paramagnetic Resonance (EPR) and Vibrating-Sample Magnetometer (VSM) techniques. EPR analysis was performed in an ESP 300e (Bruker) with band cavity-X of 9 GHz at room temperature. VSM measurements were obtained in a Physical Property Measurements System (PPMS) DynaCool, from Quantum Design.

$^{57}$Fe Mössbauer absorption spectra were taken at room temperature in transmission mode using a standard spectrometer with sinusoidal velocity sweep of the $^{57}$Co/Rh source (about 5 mCi). The hyperfine parameters derived from the spectra allow to distinguish different iron oxide phases.

X-Ray Photoelectron Spectroscopy was employed to evaluate the surface chemical environment of iron before and after reuse cycles. The spectra were recorded in a PHOIBOS 150 (SPECS), without a monochromator, and AlKα X-Ray source. Adventitious carbon (C1s at 284.6 eV) was used to calibrate the whole spectra, whilst all mathematical treatment was performed with a CasaXPS software (2.3.17). The pressure inside the analysis chamber during all measurements was in the range of $10^{-10}$ to $10^{-9}$mbar.

### 2.2.3 Indigo carmine (IC) photocatalysis

The IC photo-Fenton discoloration was evaluated in a system set up into a box that prevents from external light interference, with a 50 mL glass reactor surrounded by a cooling jacket, already described in previous works (Gonçalves *et al.*, 2020; Costa *et al.*, 2020; Rafael *et al.*, 2020). Nanocomposite dosages of 0.67 $g.L^{-1}$, 0.33 $g.L^{-1}$, 0.17 $g.L^{-1}$, and 0.07 $g.L^{-1}$, were dispersed in distilled water using an ultrasonic bath for 30 min. Then, 15 mL of IC solution ($4.2 \times 10^{-5}$ M) was aggregated to the dispersion to reach a final IC concentration of $2.1 \times 10^{-5} g.L^{-1}$. This IC concentration was selected because it is reported to be within the typical wastewater range (Aleboyeh *et al.*, 2003). Finally, the appropriate amounts of 30% $H_2O_2$ were transferred to the reactor, to complete a final volume of 30 mL and reach $H_2O_2$ concentrations of $2.3 \times 10^{-1}$ M, $1.2 \times 10^{-1}$ M, and $0.6 \times 10^{-1}$ M. At first, the magnetic stirring started, the chamber door was closed, and the mixture remained stirring for 30 min in the dark to reach

the dye-catalyst adsorption equilibrium. Then, the lamp Master HPI-T (400W), from PHILIPS, which emits predominantly visible light in the range of 380-740 nm (Rafael *et al.*, 2020) was activated, and aliquots were extracted in periodic time intervals. The time when the lamp was turned on was denominated as 0 min. A magnet was used to separate the magnetic materials from the reaction medium. After that, the liquid was filtered with a Millipore filter (MILEX-GV PVDF – 0.22 μm) and taken to a Varian Cary 500 UV-Vis spectrometer. Before each analysis, a calibration curve was performed by measuring the absorbance in the specific concentration at 611 nm, and this wavelength was used to monitor IC discoloration. Eq. 1.1 (Article 1) was employed to calculate the IC discoloration.

The photocatalyst with the best performance was selected to perform reuse experiments. In this case, the nanocomposites magnetically separated from the reaction were washed with distilled water and dried in an oven at 100ºC overnight. Then, the dried catalyst was used in the following reuse cycle, with a fixed IC/nanocomposite mass ratio of 0.015.

## 2.3 Results and discussion

### 2.3.1 Materials characterization

Figures 2.1 – 2.5 shows the microscopic analysis for bare RGO (FESEM), bulk $Fe_3O_4$ (SEM), and all nanocomposites (STEM-in-SEM). RGO (Figure 22) has a compact sheet morphology, while bulk $Fe_3O_4$ (Figure 23) is a powder characteristic with different sizes of agglomerates. Meanwhile, nearly spherical iron oxide nanoparticles were successfully anchored on RGO sheets for the three nanocomposites (Figures 24-26). The nanoparticle counts by STEM-in-SEM (Figures 2.3-2.5 and Table 5) indicate that the anchored iron oxide particles mean sizes are 12 nm for nanocomposites 1 and 2, and 15 nm for nanocomposite 3. It is worth mentioning that even with higher $Fe_3O_4$ loads, all nanocomposites showed well dispersed $Fe_3O_4$ nanoparticles on RGO sheets. The high dispersion of the small particles of iron oxide was favored by the synthesis method used, as shown by Qiu *et al.*, 2016. FESEM-EDX (Table 5) iron semiquantitative analysis obtained from different regions, for nanocomposites 3 and 2 showed iron contents (wt %) of 55.4 ± 2.8, and 41.6 ± 2.5, respectively. The observed deviation between each region is accepted due to the semiquantitative characteristic of this analysis and the heterogeneous nature of these

nanocomposites. However, the FESEM-EDX iron content (wt %) for nanocomposite 1 was found to be 29.1 ± 18.3, with a pronounced discrepancy among the regions.

Figure 22 – SEM images of bare reduced graphene oxide.

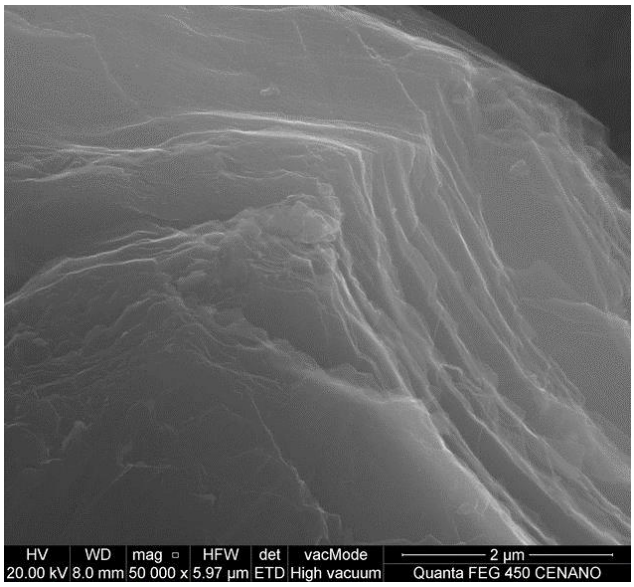


Source: The author, 2023.

Figure 23– SEM images of bulk $Fe_3O_4$.

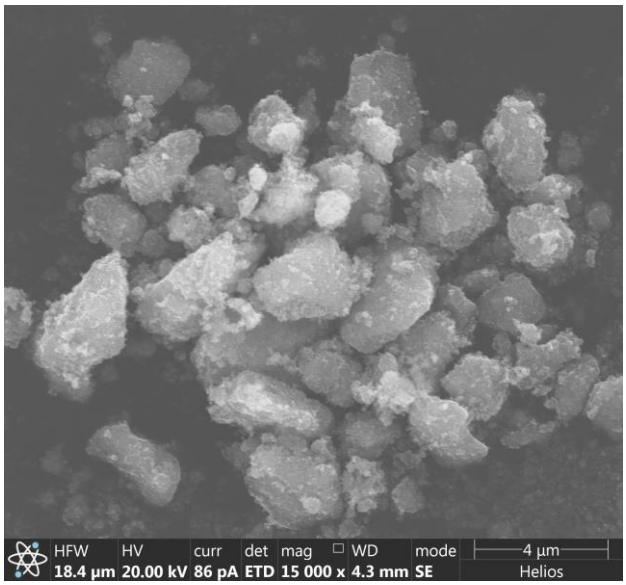


Source: The author, 2023.

Figure 24– STEM-in-SEM micrograph of nanocomposite 3.

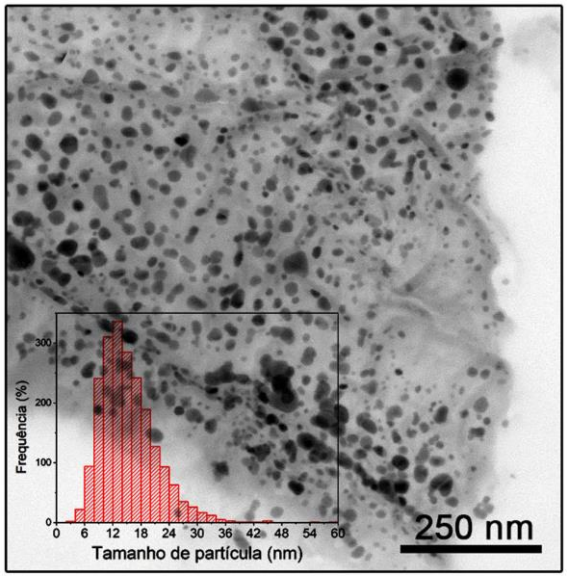


Source: The author, 2023.

Figure 25 – STEM-in-SEM micrograph of nanocomposite 2.

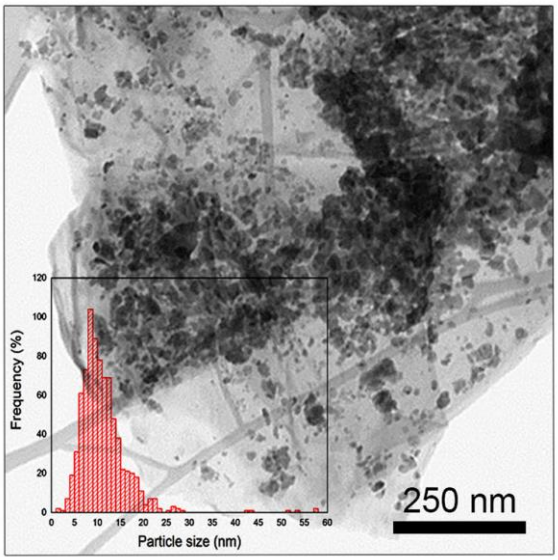


Source: The author, 2023.

Figure 26 – STEM-in-SEM micrograph of nanocomposite 1.

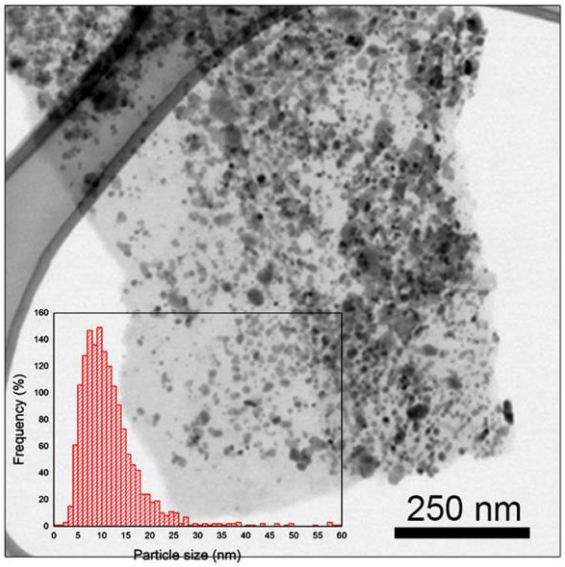


Source: The author, 2023.

Table 5 – STEM-in-SEM particle counting, FE-SEM-EDX iron content, crystallite size (by XRD), BET specific surface area, and mesopore volumes of all nanocomposites.

| Material | Iron oxide mean particle size (nm)[a] | EDX Fe content (%)[b] | Crystallite size (nm)[c] | BET specific surface area ($m^2.g^{-1}$) | $V_{meso}$ ($cm^3.g^{-1}$) | $V_{micro}$ ($cm^3.g^{-1}$) | Pore Diameter (nm) |
|---|---|---|---|---|---|---|---|
| Nanocomposite 1 | 12 | 29.1 ± 18.3 | 15 | 25 | 0.042 | 0.0013 | 8.51 |
| Nanocomposite 2 | 12 | 41.6 ± 2.5 | 16 | 81 | 0.058 | 0.0044 | 3.62 |
| Nanocomposite 3 | 15 | 55.4 ± 2.8 | 22 | 74 | 0.064 | 0.0043 | 4.25 |

Source: The author, 2023.

[a]STEM-in-SEM particle counting.

[b]Calculation for 5 different regions.

[c]Estimation by Scherrer Equation with peak at $2\theta = 35.4^o$ of $Fe_3O_4$

EDX mapping (Figures A1-A2) was performed to investigate the Fe distribution in the photocatalysts. RGO sheets of nanocomposites 3 and 2 showed to be fully covered by Fe (not shown). However, due to a high discrepancy in the different points of EDX semiquantitative analysis for nanocomposite 1, two different $Fe_3O_4$/RGO aliquots were selected to perform the EDX mapping. As a result, site 1 map (Figure A3) shows an iron oxide-rich sheet, where the circle clearly reveals a RGO sheet prolongation with no detectable iron oxide. On the

contrary, site 2 map (Figure A4) indicates an iron oxide poor RGO folded sheet. Therefore, although some heterogeneity in these materials is expected, nanocomposite 1 showed to contain manifold regions with very different characteristics, suggesting the insufficient filling of iron oxides on RGO sheets, probably due to the lower iron precursor content in this synthesis, which is 3 times lower than nanocomposite 3.

XRD patterns for all $Fe_3O_4$/RGO nanocomposites, and RGO are shown in Figure 27. For nanocomposites 2 and 3, it can be seen the crystalline $Fe_3O_4$ diffraction peaks and their respective Miller indexes, which are: 29.9º (220), 35.4º (311), 43.1º (400), 56.9º (511), and 62.5º (440). The JCPDS 76-1849 diffraction peaks, highlighted by pink bars, confirm that $Fe_3O_4$ particles were successfully formed on RGO sheets. For nanocomposite 1, however, a considerable displacement of ~0.5º of these peaks to higher 2 theta values is observed. Also, the intensity of the peaks indicated by the stars at $2\theta$ = 24.3º, 33.3º, 40.8º, and 64.2º becomes higher with the decreasing $Fe_3O_4$ contents, suggesting that hematite ($\alpha$-$Fe_2O_3$) (Han *et al.*, 2014) might be formed in lower $Fe(NO_3)_3.9H_2O$ loads [JCPDS 24-0072]. It is worth mentioning that nanocomposite 1, besides the characteristic magnetite black color, also presented a dark reddish color, which could be associated with the $\alpha$-$Fe_2O_3$ formation. These observations agree with the study performed by Dong *et al.*, (2014), which detected higher $Fe_2O_3$ amounts for the nanocomposites with higher RGO contents. In parallel, no diffraction peak at $2\theta < 10º$ was detected for the three nanocomposites, indicating that GO in the three samples was reduced to RGO. Furthermore, for nanocomposites 2 and 1, the appearance of a halo with a maximum around $2\theta$ = 25º is related to RGO. The crescent intensity of this halo was expected once the amount of RGO in these samples increased (Figure 28) (Cheng *et al.*, 2013). The Scherrer equation was used to estimate the average crystallite size, using the most intense $Fe_3O_4$ peak ($2\theta$ = 35.4º) of the synthesized nanocomposites. The results are shown in Table 5, evidencing average crystallite sizes close to the particle size counting by STEM-in-SEM. These results suggest that no significant particle agglomeration occurs in this synthesis. It is noteworthy that nanocomposite 3 showed slightly larger average crystallite size, as well as particle size (by STEM-in-SEM).

Figure 27 – XRD patterns for RGO and all nanocomposites.

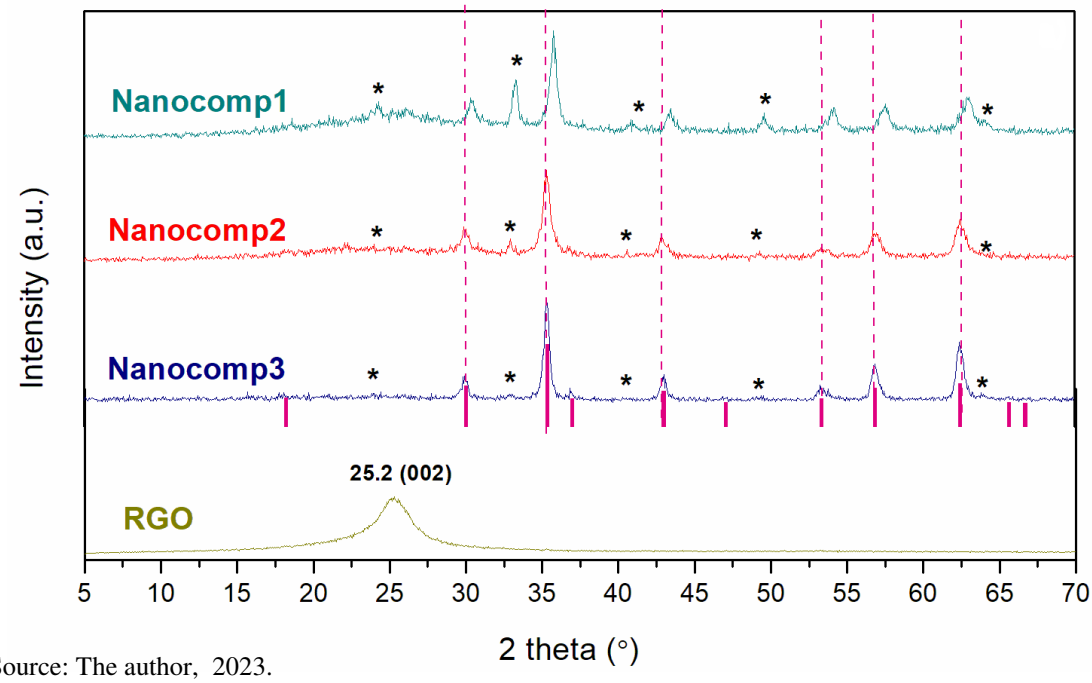


Source: The author, 2023.

Figure 28 – XRD patterns of all nanocomposites to highlight RGO halo.

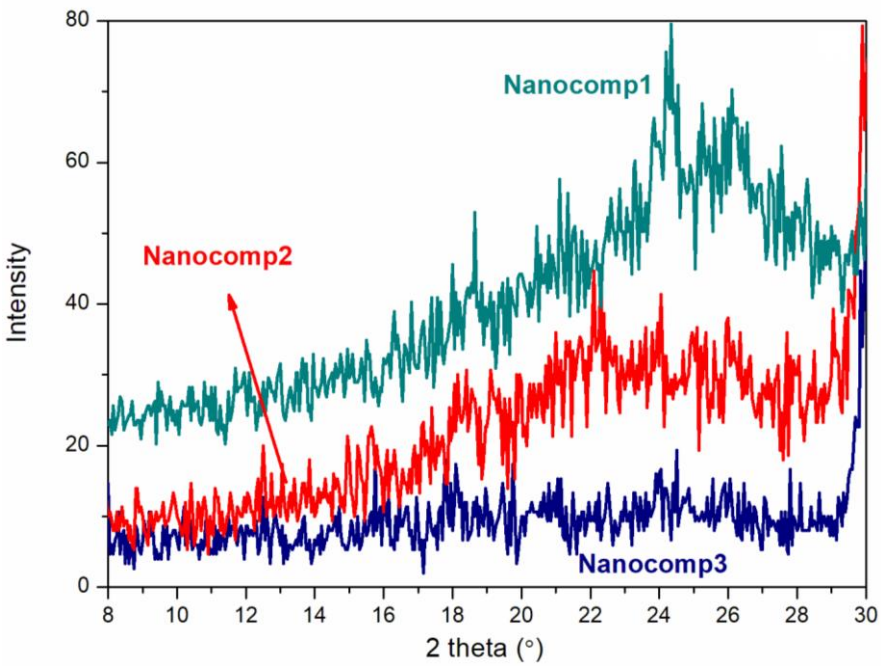


Source: The author, 2023.

Figure 29 shows the Thermogravimetric Analysis (TGA) for RGO and the three $Fe_3O_4$/RGO nanocomposites. It was observed a mass gain up to 350 ºC for nanocomposite 3. This phenomenon was already discussed elsewhere for nanocomposites of $Fe_3O_4$/RGO, and it is related to the oxidation of $Fe_3O_4$ particles (Zhou *et al.*, 2010). Considering the increasingly

XRD α-$Fe_2O_3$ diffraction peaks intensities from nanocomposite 3 to nanocomposite 1, it can be argued that the samples with lower iron contents could possess more iron particles in higher oxidation states. These results could explain that nanocomposites 2 and 1 did not present a mass gain. The maximum mass losses up to 1000ºC for nanocomposites 3, 2, and 1 were about 7%, 18%, and 26%, respectively. Once bare RGO has a total mass loss of about 95%, the iron oxide contents estimations for nanocomposites 3, 2, and 1 are 88%, 77%, and 69%, respectively.

Figure 29 – TGA analysis for RGO and all nanocomposites.

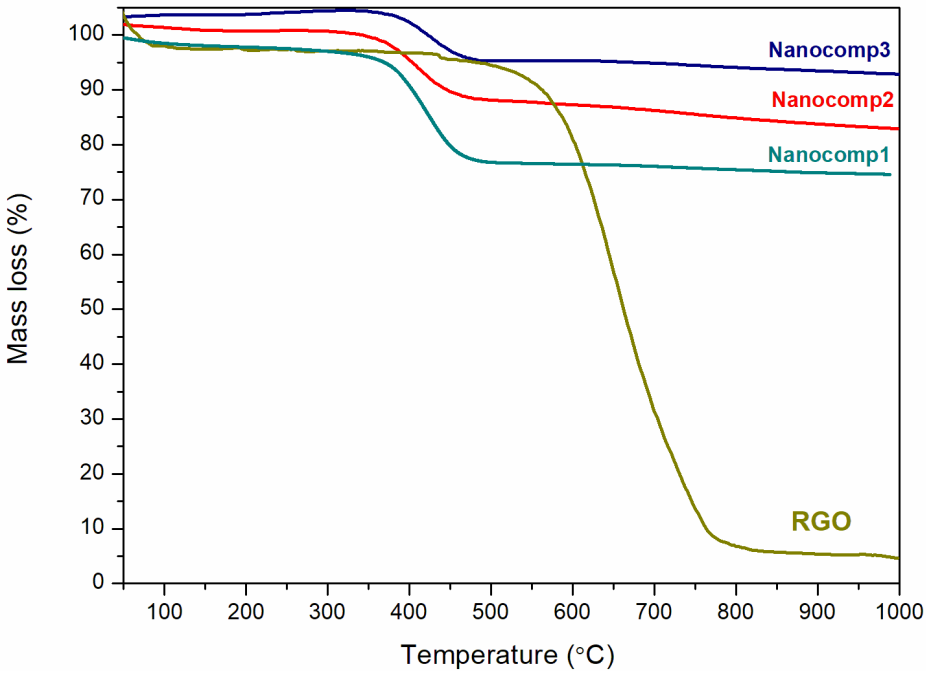


Source: The author, 2023.

The main aspects of the textural analysis of the nanocomposites are shown in Table 5. Textural analyzes (Figure A5 and A6) suggest that all nanocomposites are mesoporous (Type IV isotherms). As shown in Table 5, the BET specific surface area of nanocomposite 3 is slightly lower than that of nanocomposite 2, 74 $m^2$ $g^{-1}$ and 81 $m^2$ $g^{-1}$, respectively. Interestingly, nanocomposite 1 presented a much lower BET specific surface area (25 $m^2.g^{-1}$) than nanocomposites 3 and 2. XRD results showed the peaks related to the formation of α-$Fe_2O_3$, yet much larger for nanocomposite 1. A study performed by Jozwiak *et al.* (2007) reported a BET specific surface area for α-$Fe_2O_3$, heat-treated at 600ºC, equal to 24 $m^2.g^{-1}$.

Therefore, a plausible hypothesis is that the pronounced formation of α-$Fe_2O_3$, in nanocomposite 1 reduces its BET specific surface area.

DRS analysis was used to obtain the UV-Visible spectra of the nanocomposites and $Fe_3O_4$, aiming to use the Kulbelka-Munk and Tauc methods to extrapolate the indirect bandgap of the materials studied in this work (Kubelka; Munk, 1931; Tauc *et al.*, 1966). Figure 30 shows the curves of the $(F(R)h\nu)^{1/2}$ function versus energy for each synthesized nanocomposite and $Fe_3O_4$, while the UV-Visible spectra are shown inset. The estimated bandgap values (Table 6) for nanocomposites 3, 2, and 1 were 1.30 eV, 1.41 eV, and 1.50 eV, respectively. All nanocomposites' bandgap values showed to be lower than the bulk $Fe_3O_4$ (1.66 eV), suggesting that RGO is responsible for reducing the gap between the valence and conduction bands (Zheng *et al.*, 2020; Jin *et al.*, 2020; Sadiq *et al.*, 2017). Furthermore, the bandgap energies of nanocomposites 2 and 1 are, respectively, 0.11 eV and 0.20 eV higher than for nanocomposite 3. Wang *et al.* (2016) studied hematite photoanodes for water splitting, where a bandgap energy of 2 eV was observed for bulk α-$Fe_2O_3$. Therefore, these results might be linked to the more pronounced α-$Fe_2O_3$ formation in nanocomposites 2 and 1, already discussed in XRD results.

Figure 30 – DRS spectra for all nanocomposites and bare $Fe_3O_4$.

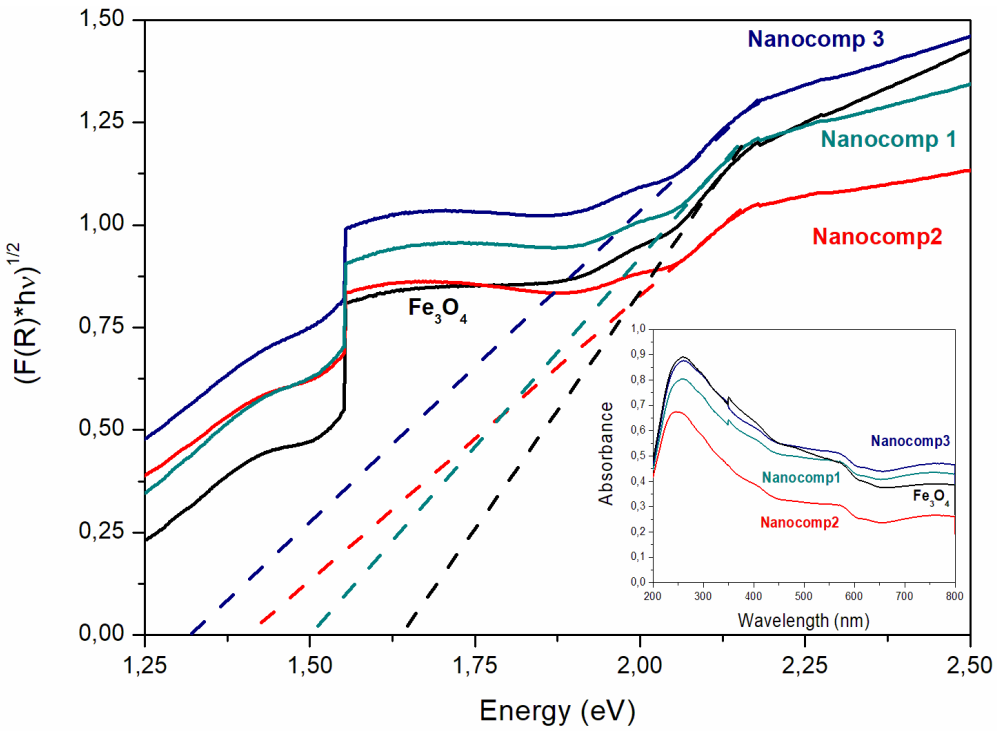


Source: The author, 2023.

Electron Paramagnetic Resonance (EPR) and Vibrating-Sample Magnetometry (VSM) were performed to investigate the magnetic properties of the nanocomposites. EPR parameters were obtained by analyzing Figure 31, considering the effective gyromagnetic factor ($g_{eff}$) and the asymmetry ratio (A), according to Equations 2 and 3, respectively:

$$\boldsymbol{g_{eff}} = \frac{h\nu}{\mu_B H_{eff}} \quad (2)$$

where, h, ν, $\mu_B$, $H_{eff}$ are the Planck constant, microwave frequency, Bohr magneton and microwave absorption maximum, respectively.

$$\boldsymbol{A} = \frac{\Delta H_{high}}{\Delta H_{low}} \quad (3)$$

where, $\Delta H_{high}$ and $\Delta H_{low}$ are the half values of the full width at half maximum on the right and left of $H_{eff}$ as represented in Figure 31, respectively. Table 6 shows that the $g_{eff}$ values are 3.74 (nanocomposite 3), 3.25 (nanocomposite 2), and 3.10 (nanocomposite 1). These results suggest the presence of larger $Fe_3O_4$ particles and/or aggregates in the nanocomposites with higher $Fe_3O_4$ contents, as discussed in XRD and STEM-in-SEM results. Also, A values for all nanocomposites are higher than 1, indicating cubic magnetocrystalline anisotropy for all nanocomposites (Klencsár *et al.*, 2019). It is important to note that the $Fe_3O_4$/RGO nanocomposites were synthesized by an *in situ* one-step synthesis to anchorage iron oxide on GO sheets, before obtaining $Fe_3O_4$ particles on RGO sheets. This process might lead to a non-uniform material, due to the heterogeneous nucleation, as discussed in a study performed by Bertran *et al.* (2020).

Figure 31 – EPR spectra for all nanocomposites.

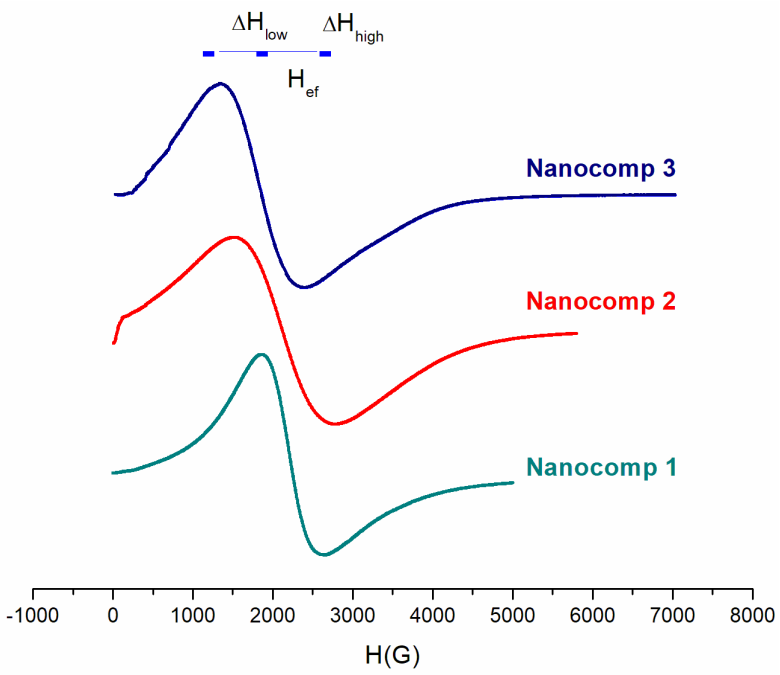


Source: The author, 2023.

VSM curves of the magnetic nanocomposites are shown in (Figure 32), and Table 6 shows the parameters obtained. The descending order of saturation magnetization ($M_S$) is: 63.6 emu.g$^{-1}$ (nanocomposite 3), 51.6 emu.g$^{-1}$ (nanocomposite 2), and 31.7 emu.g$^{-1}$ (nanocomposite 1). The coercive fields ($H_C$) are 327.5 Oe (nanocomposite 3), and 136.4 (nanocomposites 2 and 1). These results, combined with the squareness ratio ($M_R/M_S$) indicate the better response of nanocomposite 3 to the applied magnetic field, probably due to the higher iron oxide content that results in larger $Fe_3O_4$ particles and/or aggregates (Petrychuk *et al.*, 2010). Even though it is clear the decreasing in magnetization saturations values with the decreasing of $Fe_3O_4$ content in the nanocomposites, the EPR and VSM results combination shows that all nanocomposites still maintain their pronounced ferromagnetic character.

Figure 32 – VSM curves for all composites.

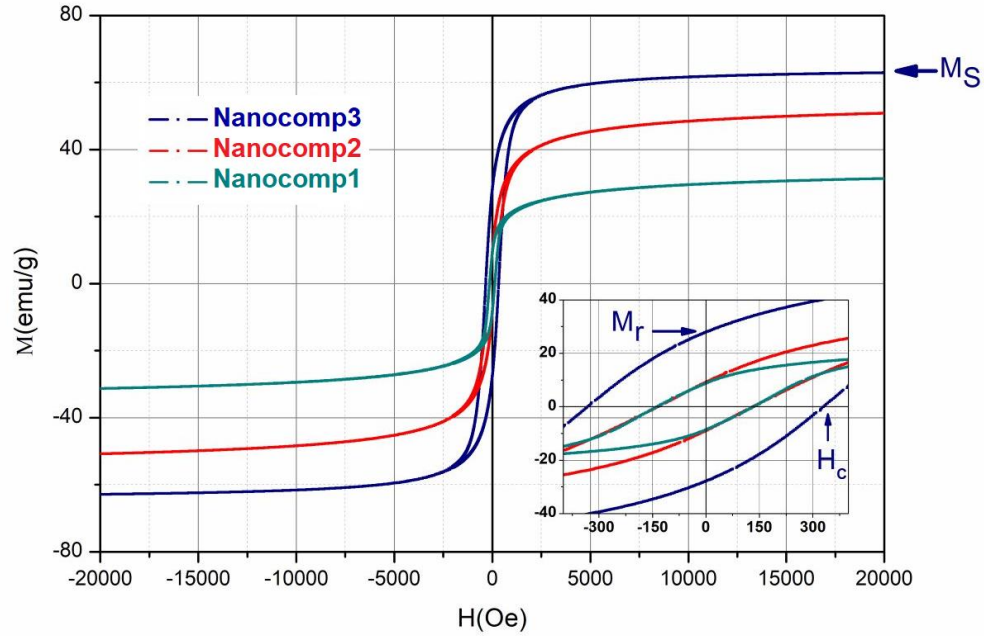


Source: The author, 2023.

Table 6 – Parameters obtained by DRS, EPR spectra and VSM curves for all nanocomposites.

| Material | Bandgap by DRS (eV) | EPR | | VSM | | | |
|---|---|---|---|---|---|---|---|
| | | $g_{eff}$ | A | $M_R$ (emu.g$^{-1}$) | $H_C$ (Oe) | $M_s$ (emu.g$^{-1}$) | $M_R/M_S$ |
| Nanocomposite 1 | 1.50 | 3.10 | 1.34 | 8.7 | 136.4 | 31.7 | 0.27 |
| Nanocomposite 2 | 1.41 | 3.25 | 1.09 | 9.1 | 136.4 | 51.6 | 0.18 |
| Nanocomposite 3 | 1.30 | 3.74 | 1.20 | 28.0 | 327.5 | 63.6 | 0.44 |
| $Fe_3O_4$ | 1.66 | - | - | - | - | - | - |

Source: The author, 2023.

In Figures 33-35 it is shown the Mössbauer spectra of the nanocomposites taken at room temperature. It is well resolved magnetic hyperfine patterns with no indications for superparamagnetism on the time scale of nuclear Larmor precession (i.e. magnetic fluctuations must be slower than $10^{-8\text{-}9}s^{-1}$) as expected for the here investigated crystallite sizes (Table 5). Under these conditions $^{57}Fe$ Mössbauer spectra allow to discriminate various iron oxide phases by their different hyperfine parameters, i.e. primarily the isomer shift S (its

value is indicating the iron valency in various lattice sites), the nuclear electric quadrupole splitting QS (reflecting the deviations from cubic site symmetry), and the magnetic hyperfine field B. In addition to these for the different iron oxides specific parameters one can determine the population of lattice sites (e.g. the tetrahedral A and octahedral B sites in $Fe_3O_4$). Data analysis was performed using MossWinn 4.0i software (Klencsár *et al.*, 1996). For the fit of the spactra we used a superposition of 4 magnetic sextet patterns: one for the trivalent A site of $Fe_3O_4$, one for its intermediate valent B site, a further pattern of minor intensity attributed to distorted and less magnetic sites B', and one sextet for $\alpha$-$Fe_2O_3$. The line shapes were assumed as Lorentzians with full width W. The magnetic hyperfine fields show a distribution (as typically found for nanoparticles) that is assumed to have Gaussian shape of width $\sigma$.

All magnetic patters reveal indications for a non-random orientation of magnetic moments with respect to the gamma ray direction. This can be taken as indication for a texture effect induced by the graphene sheet morphology.

For nanocomposites 1 and 2 (not 3) a further contribution is visible in the center of spectra that can be reproduced by a doublet patter, i.e a non-magnetic contribution, yet with a spectral weight of only a few percent, of a not well defined $FeO_x$.

The hyperfine parameters are summarized in Tables 7-9. The central result from these Mössbauer data is the quantitative separation of the contributions by $Fe_3O_4$ and $\alpha$-$Fe_2O_3$. The hyperfine parameters of both phases are in good agreement with literature values (Murad, 1998; Dézsi *et al.*, 2008). The additional octahedra B' site in $Fe_3O_4$ can be possibly associated with grain surface sites. The overall population of octahedral versus tetrahedral sites is about 1.7(2):1 and thus reduced against the ideal value of 2:1 for stoichiometric magnetite. A possible reason is that in our analysis we used the spectral areas as identical with site occupation without correction for differing Debye-Waller factors. While the nanocomposites 2 and 3 reveal comparable amounts of hematite, the amount in nanocomposite 1 is clearly enhanced which agrees with our XRD results.

Figure 33 – $^{57}$Fe Mössbauer absorption spectrum at 300K for nanocomposite 1.

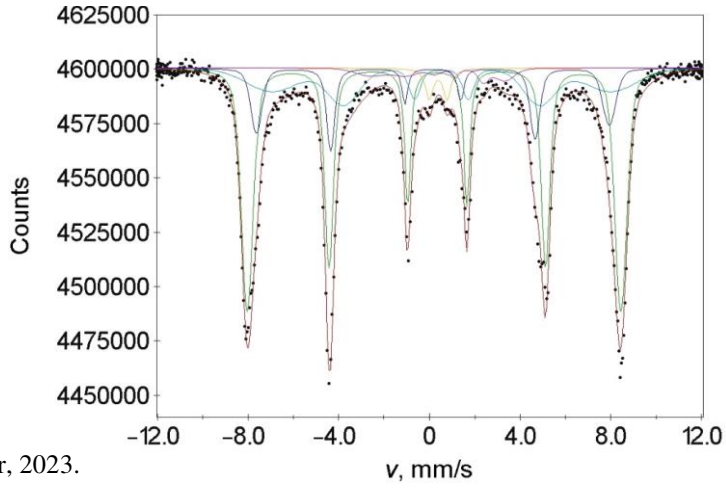


Source: The author, 2023.

Figure 34 – $^{57}$Fe Mössbauer absorption spectrum at 300K for nanocomposite 2.

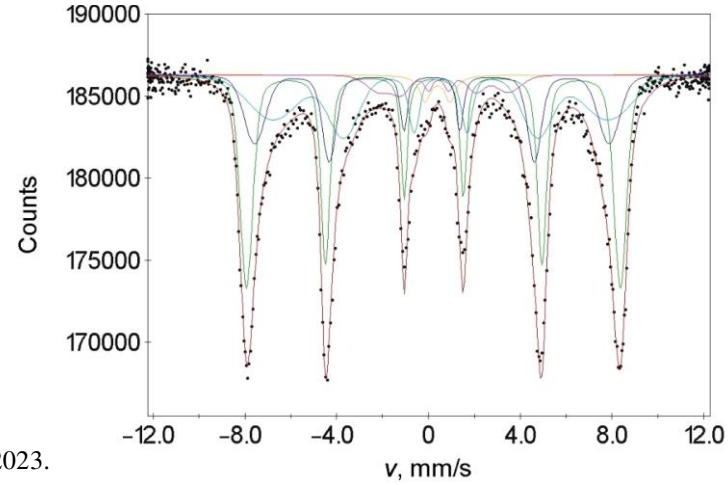


Source: The author, 2023.

Figure 35 – $^{57}$Fe Mössbauer absorption spectrum at 300K for nanocomposite 3.

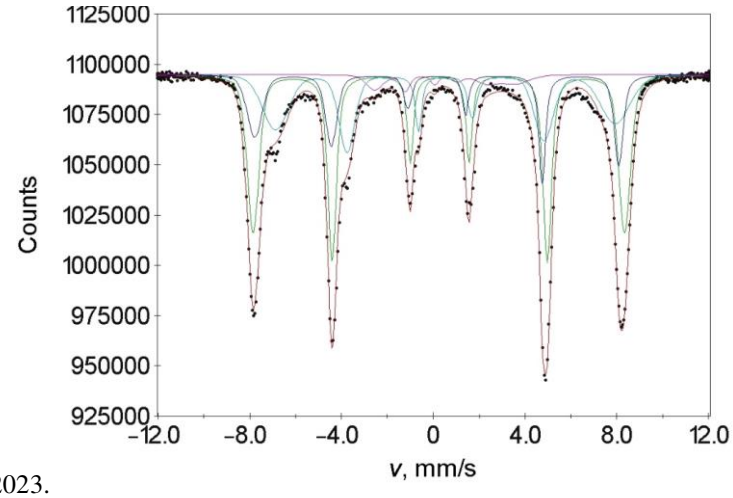


Source: The author, 2023.

Table 7 – Hyperfine parameters from Mössbauer spectra of nanocomposite 1.

| **Nanocomposite 1** | Area (%) | S (rel α Fe) | B (T) | QS (mm/s) | σ (T) | W (mm/s) |
|---|---|---|---|---|---|---|
| Sextet magnetite site A | 16(1) | 0.26(1) | 48.4(1) | 0* | 1.2(1) | 0.30* |
| Sextet magnetite site B | 22(1) | 0.64** | 46.5(2) | 0* | 5.9(1) | 0.30* |
| Sextet magnetite site B’ | 5(1) | 0.64** | 18.3(5) | 0.0(3) | 3.0* | 0.30* |
| Sextet hematite | 55(2) | 0.39(1) | 51.3(1) | -0.15(2) | 1.2(1) | 0.30* |
| Doublet | 3(1) | 0.50(5) | - | 0.79(10) | - | 0.4(1) |

Source: The author, 2023.

*value fixed during fit, **difference of isomer shift between sites A and B fixed during fit.

Table 8 – Hyperfine parameters from Mössbauer spectra of nanocomposite 2.

| **Nanocomposite 2** | Area (%) | S (rel α Fe) | B (T) | QS (mm/s) | σ (T) | W (mm/s) |
|---|---|---|---|---|---|---|
| Sextet magnetite site A | 22(1) | 0.26(1) | 48.0(1) | 0* | 2.5(1) | 0.30* |
| Sextet magnetite site B | 30(1) | 0.64** | 45.3(2) | 0* | 6.3(1) | 0.30* |
| Sextet magnetite site B’ | 6(1) | 0.67* | 17.5(5) | 0.23(5) | 3.0(1) | 0.30* |
| Sextet hematite | 40(2) | 0.33(1) | 50.7(1) | -0.01(3) | 1.3(1) | 0.30* |
| Doublet | 3(1) | 0.51(3) | - | 1.1(1) | - | 0.6(1) |

Source: The author, 2023.

*value fixed during fit, **difference of isomer shift between sites A and B fixed during fit.

Table 9 – Hyperfine parameters from Mössbauer spectra of nanocomposite 3.

| **Nanocomposite 3** | Area (%) | S (rel α Fe) | B (T) | QS (mm/s) | σ (T) | W (mm/s) |
|---|---|---|---|---|---|---|
| Sextet magnetite site A | 21(1) | 0.26(1) | 49.2(1) | 0* | 1.2(1) | 0.30* |
| Sextet magnetite site B | 30(1) | 0.64** | 46.0(2) | 0* | 3.3(1) | 0.30* |
| Sextet magnetite site B’ | 5(1) | 0.64* | 19.0(5) | 0.0(1) | 2.6(1) | 0.30* |
| Sextet hematite | 44(2) | 0.38(1) | 50.4(1) | -0.03(2) | 1.2(1) | 0.30* |
| Doublet | - | - | - | - | - | - |

Source: The author, 2023.

*value fixed during fit, **difference of isomer shift between sites A and B fixed during fit.

### 2.3.2 IC photo-Fenton discoloration

#### 2.3.2.1 IC discoloration in the absence of a heterogeneous catalyst

Figure 36 shows the IC (2.1 x $10^{-5}$M) discoloration results by varying the $H_2O_2$ inputs without any nanocomposite, named photolysis. These tests were conducted prior to the heterogeneous photo-Fenton IC discoloration aiming to set the $H_2O_2$ starting concentration. It is important to highlight that, in the absence of a heterogeneous catalyst, the IC discoloration already occurs with $H_2O_2$, due to its decomposition, as reported elsewhere (Gonçalves *et al.*, 2020; Aleboyeh *et al.*, 2003). Table A1 shows the apparent rate constant ($k_{app}$) obtained by applying the pseudo-first-order kinetics fitting (Agorku *et al.*, 2015a; Agorku *et al.*, 2015b; Eroi *et al.*, 2021; Khanh *et al.*, 2019), from the data displayed in Figure A7, for each test and their corresponding $R^2$ values. The descending order of $k_{app}$ values with their respective $H_2O_2$ concentrations was: 1.65 x $10^{-2}$ $min^{-1}$ (2.3 x $10^{-1}$ M) > 0.55 x $10^{-2}$ $min^{-1}$ (1.2 x $10^{-1}$ M) > 0.31 x $10^{-2}$ $min^{-1}$ (0.6 x $10^{-1}$ M). These results clearly indicate a significant contribution of the $H_2O_2$ as the oxidizing agent. However, UV-visible spectra (Figure 37) of the test with the highest IC discoloration (2.3 x $10^{-1}$M of $H_2O_2$) shows that, even in the highest [$H_2O_2$], the peak 611 nm does not decrease in a satisfactory magnitude, reflecting in a maximum IC discoloration below 50%.

Figure 36 – IC discoloration with different $H_2O_2$ inputs, and without a photocatalyst.

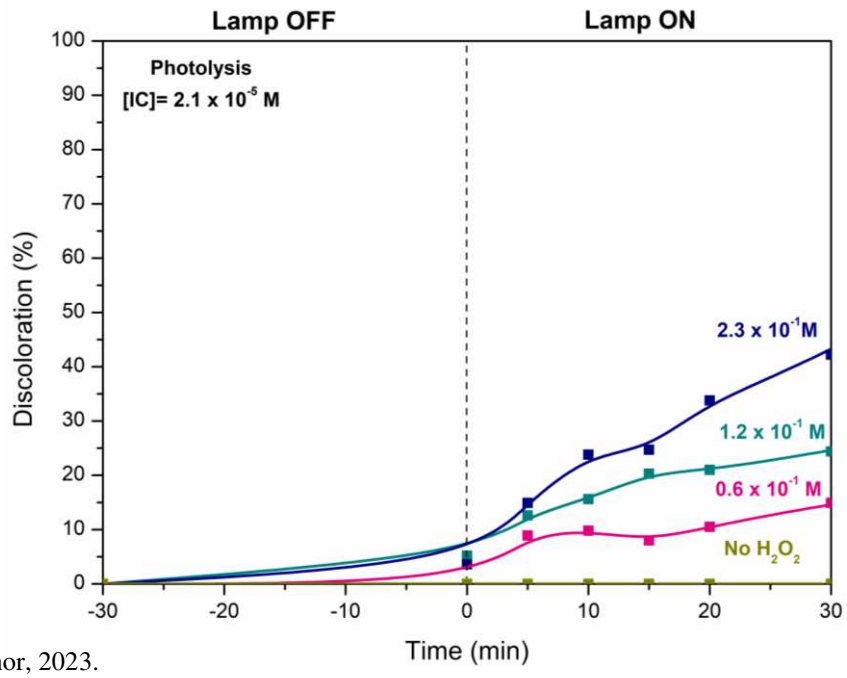


Source: The author, 2023.

Figure 37 – UV-visible spectra for photolysis tests.

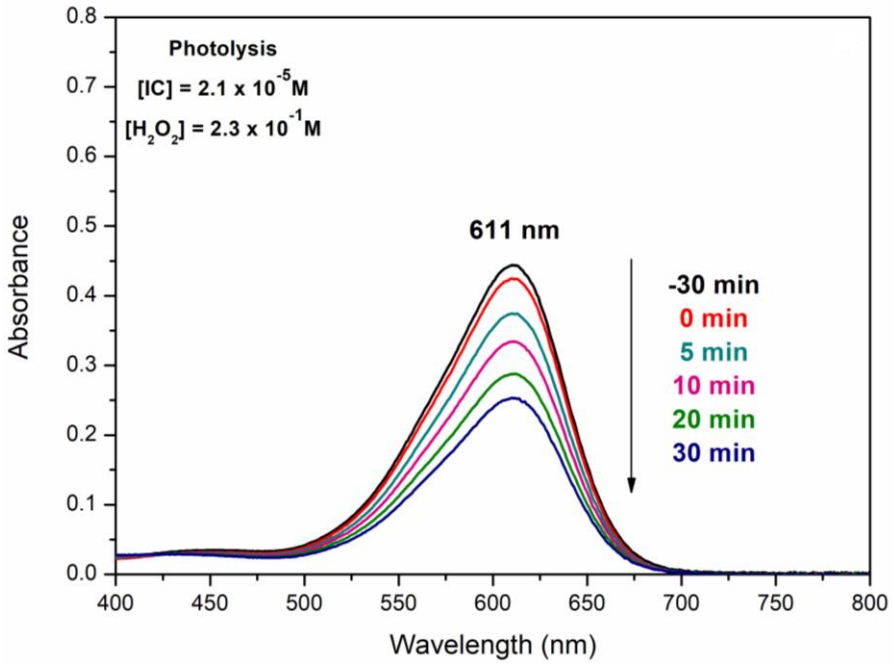


Source: The author, 2023.

IC discoloration in function of [$H_2O_2$] can be explained by the more available $H_2O_2$ molecules to be photo-decomposed, leading to higher •OH radical generation (Equation 4) (Aleboyeh *et al.*, 2003).

$$H_2O_2 + hv \rightarrow 2 \cdot OH \tag{4}$$

It is worth mentioning that no decrease was observed in IC discoloration with the increasing of $H_2O_2$ loading, as discussed elsewhere (Aleboyeh *et al.*, 2003). If an excess of $H_2O_2$ is added to the photo-Fenton system, it may lead to the formation of hydroperoxyl radicals (•$O_2H$) and water, described in Equations 5, and 6.

$$H_2O_2 + \cdot OH \rightarrow \cdot O_2H + H_2O \tag{5}$$

$$H_2O_2 + \cdot O_2H \rightarrow \cdot OH + H_2O + O_2 \tag{6}$$

Furthermore, if the system is saturated with •OH radicals, they may immediately combine to form hydrogen peroxide (Equation 7).

$$\cdot OH + \cdot OH \rightarrow H_2O_2 \tag{7}$$

With respect to photo-Fenton dye discoloration, products formed in Equations 5-7 are not desirable, since they are much less reactive than •OH radicals (Zhang *et al.*, 2009; Ji *et al.*, 2011). For instance, $•O_2H$ and $H_2O_2$ have oxidation potentials of 1.4V and 1.8V, respectively, while •OH radicals have a much higher oxidation potential of 2.8V. According to Figures 36 and A7, the highest $H_2O_2$ concentration tested in this work (2.3 x $10^{-1}$ M) seems to be below the $H_2O_2$ limit, this concentration being therefore selected to perform the heterogeneous photo-Fenton tests with the three synthesized nanocomposites and bulk $Fe_3O_4$.

2.3.2.2 Heterogeneous IC photo-Fenton discoloration

At first, the heterogeneous photocatalytic tests were carried out with a catalyst load of 0.67 g.$L^{-1}$, 30 mL of IC solution (2.1 x $10^{-5}$ M), and 30% $H_2O_2$ (2.3 x $10^{-1}$M) (Figure A8). The choice of using this catalyst dosage was based on our previous study, which described a $Fe_3O_4$/RGO nanocomposite that discolored an IC solution (2.1 x $10^{-5}$ M) within 5 min (Gonçalves *et al.*, 2020). All nanocomposites showed to be very active in the IC photo-Fenton discoloration and presented superior IC discoloration performance than the photolysis with 2.3 x $10^{-1}$ M of $H_2O_2$. However, with a catalyst dosage of 0.67 g.$L^{-1,}$ it was impossible to note a significant difference among the three nanocomposites. Furthermore, due to the fast discoloration observed with all nanocomposites, a reliable acquisition of enough points to perform the kinetics calculations was prevented, thus no kinetic plots for 0.67 g.$L^{-1}$ are presented in this work. Aiming to investigate the IC photo-Fenton discoloration kinetics with the synthesized nanocomposites, the catalyst dosage was reduced by half. Figure 38 shows the IC discoloration with a catalyst dosage of 0.33 g.$L^{-1}$ and $H_2O_2$ (2.3 x $10^{-5}$ M), as well as the kinetic plots for each nanocomposite. Now, a noticeable difference can be observed among the three nanocomposites. IC discoloration at 5 min for nanocomposite 3 was 93.9%, followed by nanocomposite 2 (90.8%) and nanocomposite 1 (60.7%). It is also important to note that nanocomposite 3 reached a maximum IC discoloration of 99.7% at 30 min. Once again, even lowering the catalyst dosage by half, all nanocomposites showed to be far more active than photolysis with 2.3 x $10^{-1}$ M of $H_2O_2$. Furthermore, nanocomposites 3 and 2 discoloration curves showed to be higher than for bulk $Fe_3O_4$. The data for the heterogeneous photo-Fenton tests (Figure A9) were also best fitted with the pseudo-first-order model, as described for the tests without the heterogeneous photocatalysts. The $k_{app}$ and $R^2$ values for each nanocomposite and bulk $Fe_3O_4$ are presented in Table A1. The $k_{app}$ descending ranking

was as follows: nanocomposite 3 (8.99 x $10^{-2}$ $min^{-1}$) > nanocomposite 2 (8.51 x $10^{-2}$ $min^{-1}$) > $Fe_3O_4$ (6.13 x $10^{-2}$ $min^{-1}$) > nanocomposite 1 (3.69 x $10^{-2}$ $min^{-1}$). These results indicate that RGO improves the photocatalytic character of the $Fe_3O_4$ nanoparticles, except for nanocomposite 1.

Figure 38 – IC photo-Fenton discoloration for the different nanocomposites with a catalyst dosage of 0.33 $g.L^{-1}$.

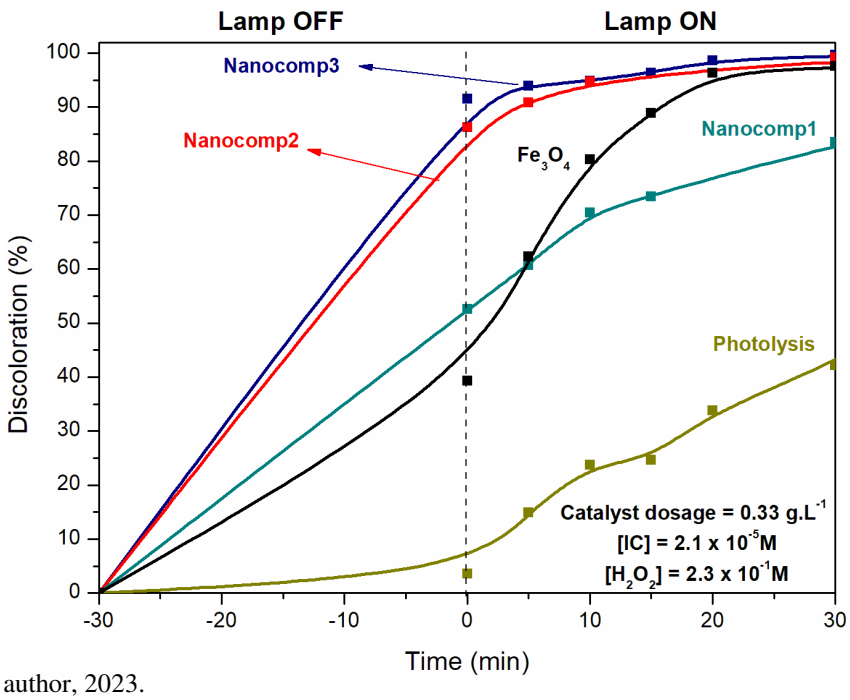


Source: The author, 2023.

This assumption can be supported by STEM-in-SEM particle counting and XRD crystallite size, which showed that $Fe_3O_4$ nanoparticles of 12-15 nm size (STEM-in-SEM) were successfully anchored on RGO sheets, resulting in more available particles to transform $H_2O_2$ molecule into •OH radicals. Furthermore, the narrower bandgap, estimated by DRS analysis, after $Fe_3O_4$ nanoparticles immobilization on RGO, leads to a more active photocatalyst. In addition, the slight difference in photocatalysis activity between nanocomposite 3 and 2 may be linked to their slightly different formation of α-$Fe_2O_3$, observed by XRD and Mössbauer analysis. Yet for these two nanocomposites, the appearance of a non-magnetic $FeO_x$ oxide in nanocomposite 2 confirmed by Mössbauer analysis, also supports its lower activity. According to Liu *et al.* (2017), hematite presents lower activity than other iron oxide phases in the Fenton reaction because it exhibits a high electron-hole recombination rate. In addition, the bandgap for $Fe_2O_3$ reported in literature is wider than for $Fe_3O_4$ (Iqbal *et al.*, 2020). DRS analysis also showed that nanocomposite 2 presented higher

bandgap value than nanocomposite 3, corroborating with the observed by XRD analysis. On the contrary, nanocomposite 1 did not perform better than bulk $Fe_3O_4$. This behavior can be explained by the combination of the results obtained in characterization section. FESEM-EDX (Table 5) and EDX mapping (Figures A1-A2) showed that nanocomposite 1 presented a high discrepancy in iron distribution through RGO sheets. This may lead to iron oxide agglomerates thus lowering its specific surface area, confirmed by textural analysis. Furthermore, the more pronounced formation of α-$Fe_2O_3$, and non-magnetic $FeO_x$, observed by XRD analysis and Mössbauer spectroscopy, may contribute to lower performance, due to its wider bandgap and higher electron-hole recombination rates.

The photo-Fenton heterogeneous IC discoloration with the $Fe_3O_4$/RGO nanocomposites can be summarized by Equations 8-11. Firstly, when $Fe_3O_4$/RGO nanocomposite is irradiated by visible light, it absorbs a photon, photoexciting an electron from valence band to the conduction band. This phenomenon is responsible for creating an electron hole in the valence band (Equation 8). The promoted electron ($e^-$) on RGO surface in contact with $H_2O_2$ and $H^+$ generates the •OH radicals (Equation 9), whereas the hole ($h^+$) in $Fe_3O_4$ combined with the water $OH^-$, also results in •OH radicals (Equation 10). These structures attack the IC molecule, generating degradation products leading to the discoloration of the solution (Equation 11).

$$Fe_3O_4/RGO + hv \rightarrow Fe_3O_4\,(h^+) + RGO\,(e^-) \quad (8)$$

$$RGO\,(e^-) + H_2O_2 + H^+ \rightarrow \cdot OH + H_2O \quad (9)$$

$$Fe_3O_4\,(h^+) + OH^- \rightarrow Fe_3O_4 + \cdot OH \quad (10)$$

$$Indigo\ carmine\ dye + \cdot OH \rightarrow degradation\ products \quad (11)$$

Due to the best performance in IC discoloration, nanocomposite 3 was selected and a nanocomposite dosage variation study was conducted considering IC discoloration (2.1 x $10^{-5}$ M) and $H_2O_2$ (2.3 x $10^{-1}$ M) (Figure 39, A8 and Table A1). All IC discoloration curves for the three loads of nanocomposite 3 showed to be higher than the photolysis, with emphasis on 0.33 g.$L^{-1}$ curve (IC discoloration of 99.7% at t = 30 min). Although nanocomposite 3 dosages of 0.17 g.$L^{-1}$ and 0.07 g.$L^{-1}$ resulted in discoloration curves higher than the photolysis test until t = 20 min, they became significantly close at the succeeding times. Therefore, these loads were not enough to observe the photocatalyst activity, and the dosage of 0.33 g.$L^{-1}$ was fixed.

Figure 39 – IC photo-Fenton discoloration with different dosages of nanocomposite 3.

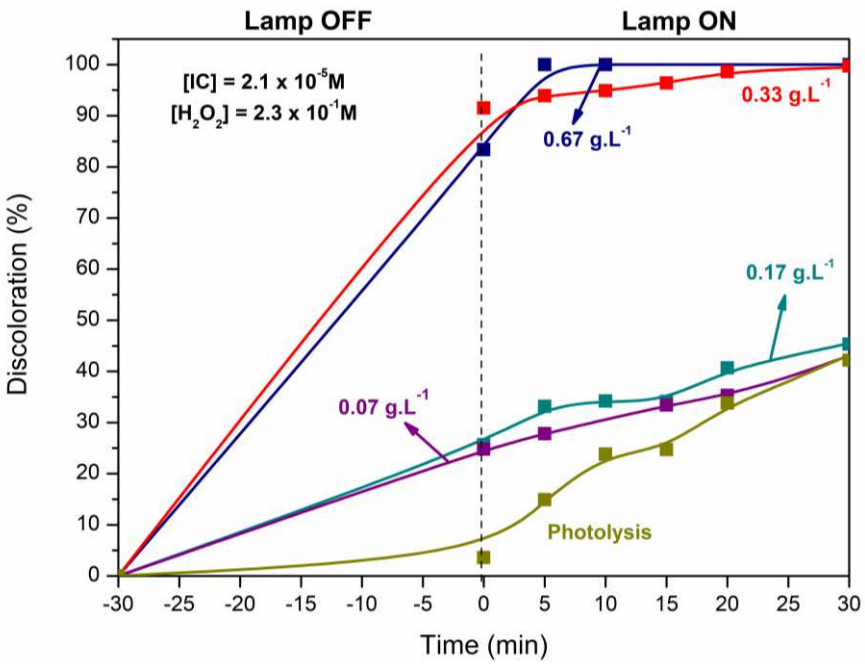


Source: The author, 2023.

Figures 40, 41, A9 and Table A1 show the photocatalytic tests and results of nanocomposite 3 for different $H_2O_2$ inputs, performed with a photocatalyst dosage of 0.33 $g.L^{-1}$ and 30 mL of IC solution (2.1 x $10^{-5}$ M). In this sense, two more tests varying the $H_2O_2$ concentration, and another without $H_2O_2$ were executed to observe if the $H_2O_2$ amount could be reduced in the heterogeneous photo-Fenton IC photocatalysis, without losing significant discoloration results.

As can be seen in Figures 40, 41, A9, and Table A1 reducing the $H_2O_2$ concentrations to 1.2 x $10^{-1}$ M and 0.6 x $10^{-1}$ M, leads to a decrease in IC discoloration at t = 5 min, to 87.3% ($k_{app}$ = 6.94 x $10^{-2}$ $min^{-1}$) and 70.1% ($k_{app}$ = 5.02 x $10^{-2}$ $min^{-1}$), respectively for the nanocomposite 3. Furthermore, if $H_2O_2$ is completely removed from this system, a drastic activity drop is observed (IC discoloration at t = 5 min equal to 39.4% and $k_{app}$ = 0.30 x $10^{-2}$ $min^{-1}$). The results found for the $H_2O_2$ concentration study with nanocomposite 3 (0.33 $g.L^{-1}$), compared with the tests without a heterogeneous photocatalyst, clearly indicate that the presence of the $Fe_3O_4$/RGO nanocomposite is responsible for facilitating the •OH radical formation, thus improving the IC discoloration.

Figure 40 – IC photo-Fenton discoloration with different $H_2O_2$ concentrations and nanocomposite 3 (0.33g.L$^{-1}$).

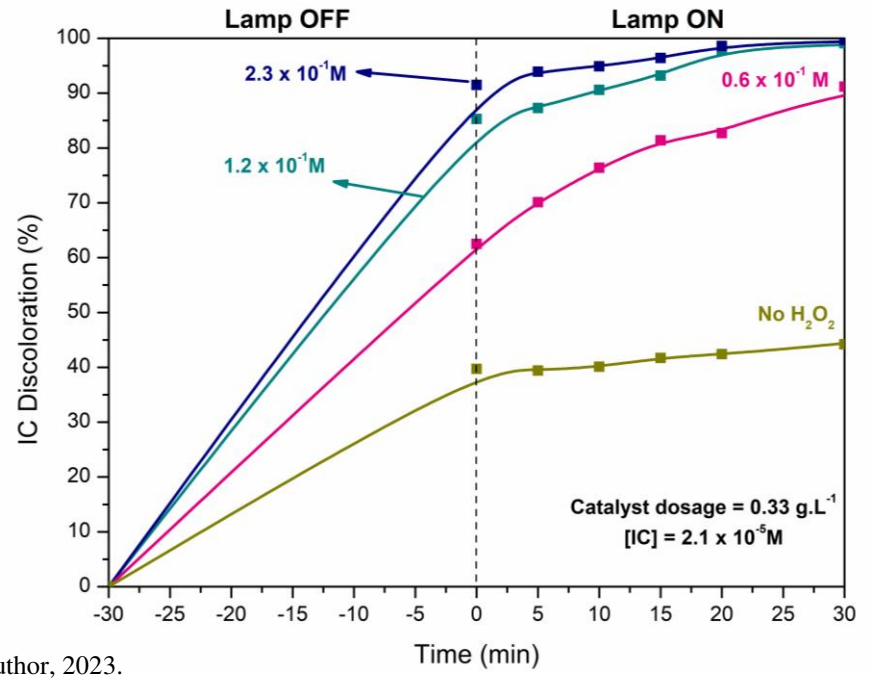


Source: The author, 2023.

Figure 41 – UV-visible absorption spectra obtained for each time interval for IC photo-Fenton discoloration with nanocomposite 3 (0.33 g.L$^{-1}$).

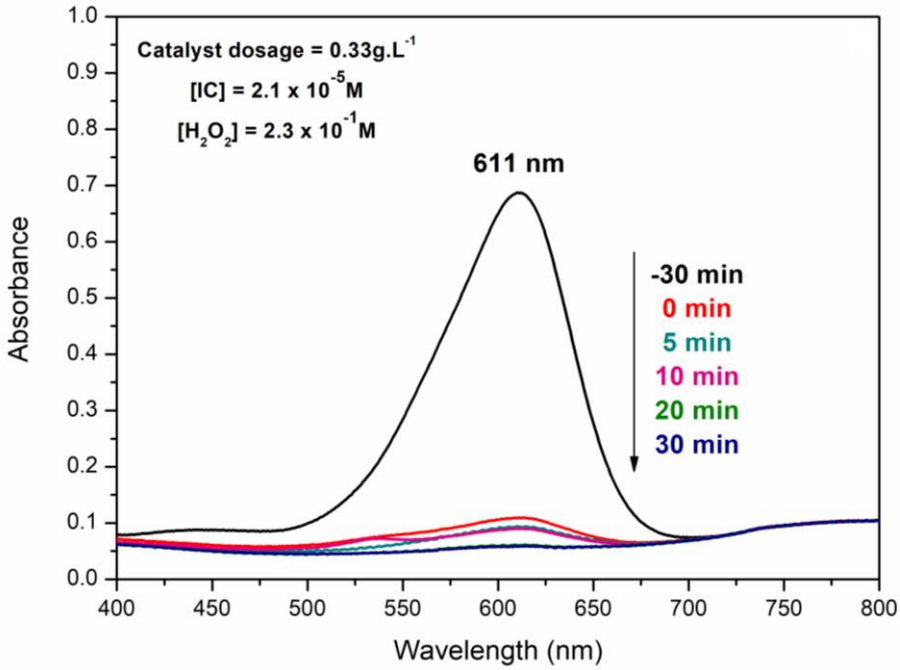


Source: The author, 2023.

The recycling tests for nanocomposite 3 are shown in Figures 42, and 43. It is observed that nanocomposite 3 remained its outstanding activity (~99%) after 30 min for, at least, three recycles or four runs.

Figure 42 – IC photo-Fenton discoloration curves for nanocomposite 3 recycling tests.

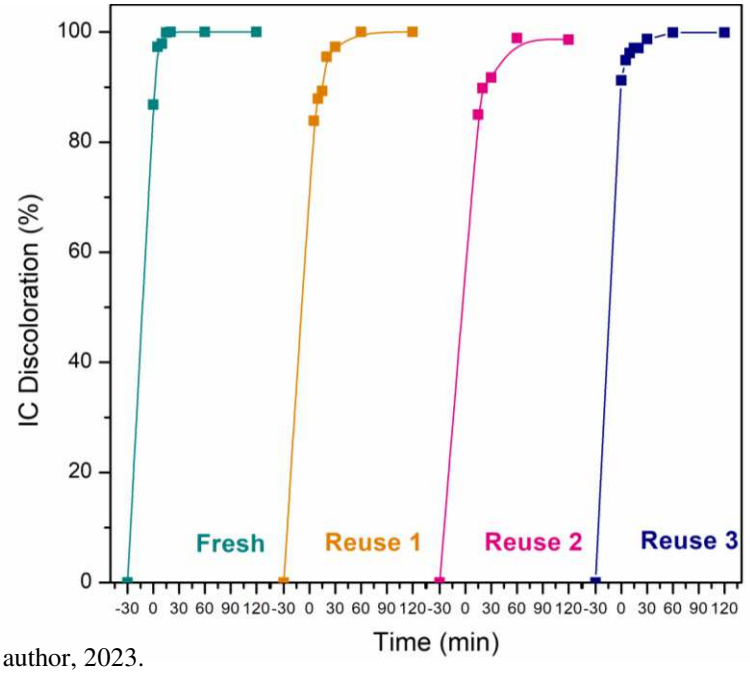


Source: The author, 2023.

Figure 43 – UV-visible absorption spectra obtained for each time interval for IC photo-Fenton discoloration with the third reuse of nanocomposite 3 (0.33 g.L$^{-1}$).

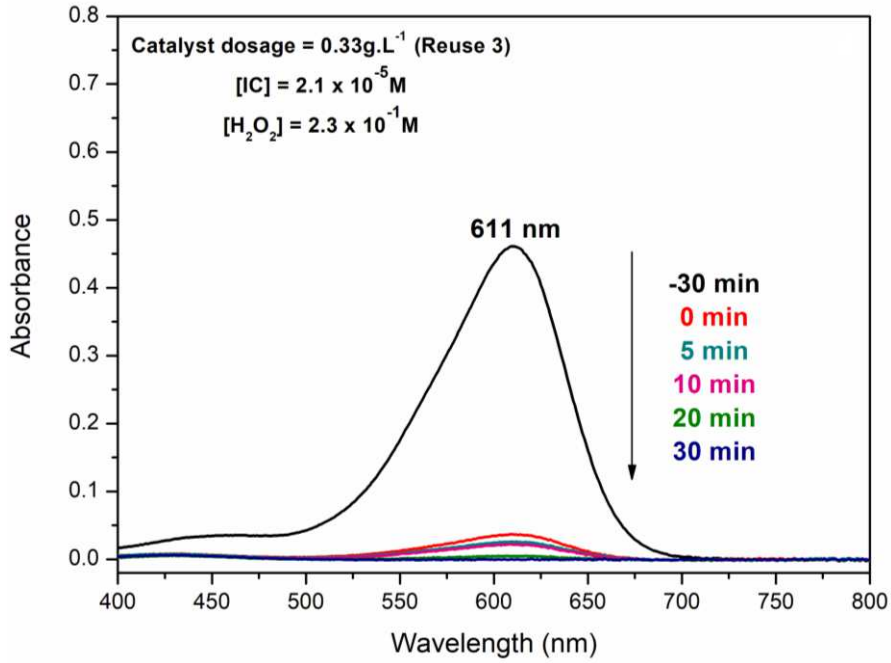


Source: The author, 2023.

Figures 44, and 45 shows the XPS analysis of fresh nanocomposite 3, and after its third recycle.

Figure 44 – Fe2p XPS photoelectron spectra of fresh and reused (3 recycles, or 4 runs) nanocomposite 3.

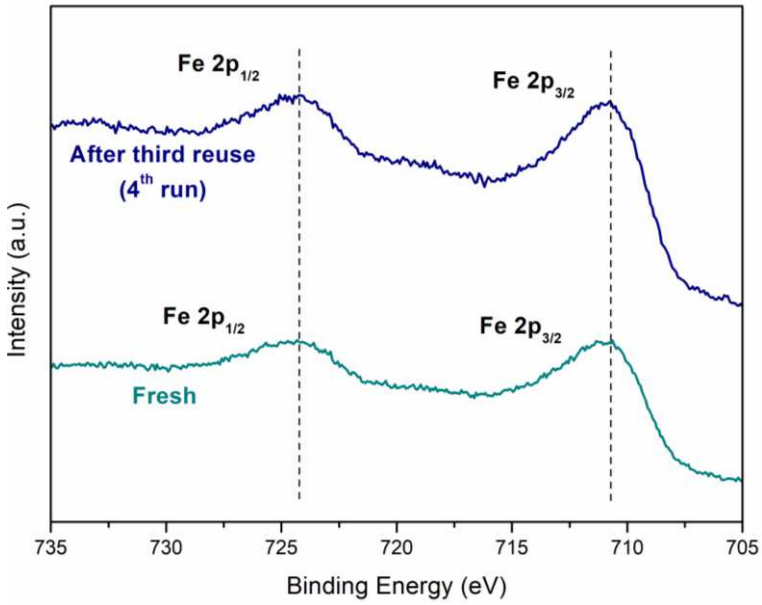


Source: The author, 2023.

Figure 45 – $Fe2p_{3/2}$ peak fitting of fresh and reused (3 recycles, or 4 runs) nanocomposite 3.

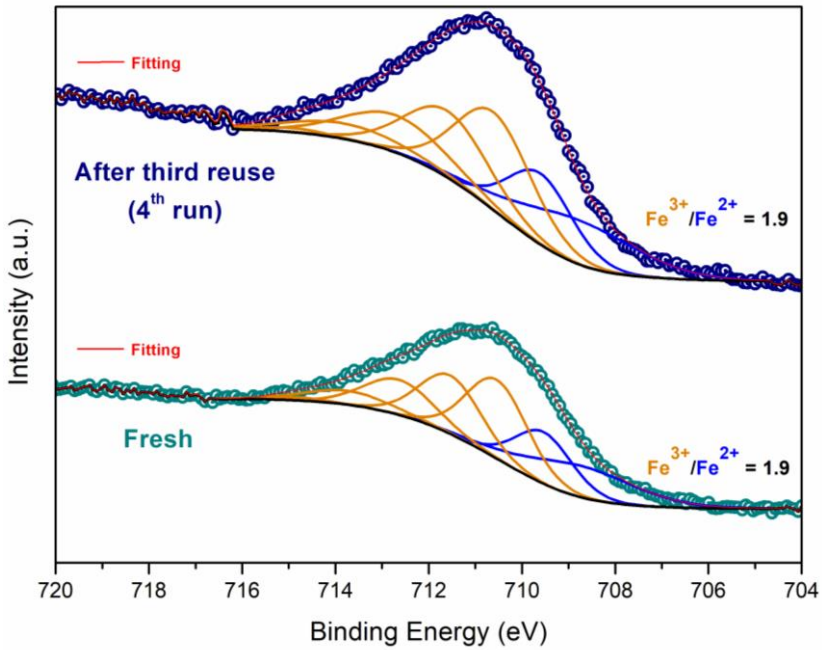


Source: The author, 2023.

The Fe2p spectra comparison (Figure 44) indicates that $Fe2p_{3/2}$ and $Fe2p_{1/2}$ photoelectron peaks did not have any significant displacements for both samples, as well as the spin-orbit splitting, which remained at 13.6 eV. After a thorough $Fe2p_{3/2}$ peak fitting (Figure 45) with the parameters described by Biesinger *et al.* (2011) it was observed that the $Fe^{3+}/Fe^{2+}$ ratio persisted at 1.9. These results are strong evidence that RGO stabilizes the $Fe^{3+}/Fe^{2+}$ pair, maintaining its activity, and by mitigating the electron ($e^-$) – hole ($h^+$) recombination, a critical phenomenon that is responsible for the deactivation of photocatalysts (Agorku *et al.*, 2015a; Agorku *et al.*, 2015b; Khanh *et al.*, 2019). However, higher RGO amounts, as observed by XRD for nanocomposites 2 and 1, lead to α-$Fe_2O_3$ formation, changing the nanocomposite physical-chemical properties, thus reducing its photocatalytic activity. Moreover, other works that synthesized different semiconductor oxides/RGO nanocomposites observed that adding low amounts of RGO is crucial for maintaining their photocatalytic activity (Su *et al.*, 2021; Jiang *et al.*, 2017; Wei *et al.*, 2020), supporting that higher RGO contents above an optimal RGO load result in lower performances.

#### 2.3.2.3 Critical assessment of IC discoloration with $Fe_3O_4$/RGO nanocomposites

One concern about heterogeneous Fenton-like reactions with $H_2O_2$ is that the generated •OH radicals have very short half-life, meaning that these structures can be rapidly transformed before attacking the pollutant molecule in bulk solution, thus reducing the system efficiency (Zhang *et al.*, 2020). In this sense, Xu *et al.* (2023) designed a nanoreactor of halloysite nanotubes internally loaded with $Fe_3O_4$ nanoparticles ($Fe_3O_4$@HNTs), aiming to increase the reaction medium confinement, thus improving radicals' utilization in MO dye discoloration. This author indeed observed that in the condition with nanoconfinement, MO discoloration was significantly improved. Furthermore, by using radical scavenging experiments, this author also observed that besides •OH radical, the formation of $^1O_2$ also has crucial role in MO discoloration. Therefore, the presence of other reactive oxygen species cannot be discarded. Thus, quenching experiments are suggested to improve understanding of the IC degradation mechanism for further works (Li *et al.*, 2023). Nevertheless, in our work, RGO was used to anchor and stabilize $Fe_3O_4$ nanoparticles, and especially for nanocomposite 3. Besides its high $Fe_3O_4$ load we can observe that it presented low nanoparticle mean size (Figure 24 and Table 5), improved textural properties such as high surface area (Table 5), and mesoporous structure. Thus, these properties may provide favorable conditions to the

continuous reactive oxygen species generation and its further utilization, as well as the IC dye adsorption onto $Fe_3O_4$/RGO active sites, once these reactions are known to occur mostly on the heterogeneous catalyst surface (Xu *et al.*, 2023). This hypothesis can be endorsed by Figure 40, which shows that the increasing in [$H_2O_2$] for nanocomposite 3 reflects in higher and faster IC discoloration.

Table 10 brings information about IC discoloration in the presence of distinct photocatalysts from other works. References Coelho *et al.*, (2010), Oliveira *et al.*, (2021), Hadjltaief *et al.*, (2021), and Ray *et al.*, (2020), not discussed in the text, are displayed only in Table 10 for comparison purposes. Considering the maximum discoloration, the time due to reach it, and the $k_{app}$ values, the present work shows quick IC photo-Fenton discoloration, and very active $Fe_3O_4$/RGO nanocomposites, with emphasis on nanocomposite 3. Furthermore, some works listed in Table 10 also performed photocatalyst recovery and new IC discoloration cycles. As aforementioned, our $Fe_3O_4$/RGO nanocomposites possess a strong magnetic character, providing an easy recovery method for succeeding IC discoloration cycles. Comparing it with the literature on the recycling capability of nanocomposite 3, one can infer that this is promising. In addition, this work did not use any initial pH correction or sonification and was carried out at room temperature, leading to a simpler IC discoloration system.

A facile two-step method to anchor and disperse high loads of $Fe_3O_4$ over RGO sheets was successfully adapted from the Stöber-like[31] method, resulting in very active nanocomposites for IC discoloration. With this approach we were able to employ cost-effective reagents and mild temperature (60°C) during iron particles nucleation, which are important aspects that could result in scalable processes for environmentally friendly nanocomposites production, as discussed elsewhere (Ansari *et al.*, 2018; Parveen, *et al.*, 2023; Ansari, 2023; Ansari, *et al.*, 2023).

In this sense, the magnetic properties, reusability, and simplicity of the photo-Fenton system described hereby, is a set of features that can be considered, aiming to contribute to the remediation of dye-containing wastewater. Furthermore, adding low amounts of RGO to iron oxide/RGO nanocomposites might be attractive once iron oxides are abundant, thus cost-effective.

Table 10 – IC heterogeneous catalysis discoloration results of different works found in literature.

| Catalyst | IC/ catalyst mass ratio | Maximum IC discoloration (%) | $k_{app}$ ($10^{-2}.min^{-1}$)[a] | Recycles (% discoloration) | REF |
|---|---|---|---|---|---|
| $Fe_3O_4$/RGO | 0.02 | 99.9 (5 min) | - | 1 (~100) | Gonçalves *et al.*, 2020 |
| $Fe_3O_4$ | 0.03 | 97.8 (60 min) | 6.13 | - | Present work |
| $Fe_3O_4$/RGO (Nanocomposite 1) | 0.03 | 96.3 (60 min) | 3.69 | - | Present work |
| $Fe_3O_4$/RGO (Nanocomposite 2) | 0.03 | 99.2 (30 min) | 8.51 | - | Present work |
| $Fe_3O_4$/RGO (Nanocomposite 3) | 0.03 | 99.7 (30 min) | 8.99 | 3 (99.0) | Present work |
| Pd-ZnS/RGO | 0.02 | 100 (210 min) | 2.19 | - | Agorku *et al.*, 2015b |
| Co-ZnS/RGO | 0.02 | 100 (210 min) | 3.10 | - | Agorku *et al.*, 2015a |
| $WO_3$ | 0.5 | 90.0 (120 min) | 1.83 | 3 (70.0) | Eroi *et al.*, 2021 |
| $ZnBi_2O_4$/RGO | 0.05 | 91.0 (75 min) | 3.20 | 3 (84.6) | Khanh *et al.*, 2019 |
| Sn/$Al_2O_3$ | 0.05 | 100 (40 min) | - | - | Coelho *et al.*, 2010 |
| g-$C_3N_4$ | 0.04 | ~100 (50 min) | 3.74 | - | Oliveira *et al.*, 2021 |
| ZnO-$Fe_3O_4$/kaolinite clay | 0.006 | 100 (70 min) | 5.20 | 4 (98.0) | Hadjtaief *et al.*, 2021 |
| Ni-$BaMo_3O_{10}$ | 0.01 | 98.0 (180 min) | 4.29 | 4 (98.0) | Ray *et al.*, 2020 |

Source: The author, 2023.

[a]pseudo-first-order fitting.

## 2.4 Conclusion

$Fe_3O_4$/RGO nanocomposites were synthesized with different precursors ratios ($Fe(NO_3)_3.9H_2O$ : GO) and evaluated in the photo-Fenton discoloration of indigo carmine. The materials were characterized, and their physical-chemical properties were associated with their performances in the indigo carmine photo-Fenton discoloration.

Microscopic analysis showed that the nanocomposites with higher iron precursor loads resulted in well-distributed iron oxide nanoparticles on RGO sheets. In parallel, XRD patterns and Mössbauer spectra showed that lowering the $Fe(NO_3)_3.9H_2O$ : GO ratio leads to the formation of a crystalline $\alpha$-$Fe_2O_3$ phase, and formation of a non-magnetic $FeO_x$.

The photocatalyst with the best performance in indigo carmine ($2.1 \times 10^{-5}$ M) photo-Fenton discoloration was the nanocomposite 3 ($Fe(NO_3)_3.9H_2O$ : GO) mas ratio of 17:1. With a photocatalyst dosage and $H_2O_2$ concentration of 0.33 $g.L^{-1}$ and $2.3 \times 10^{-1}$ M, respectively, IC discoloration reached 99.7% ($k_{app} = 8.99 \times 10^{-2}$ $min^{-1}$), at 30 min of reaction. The well-dispersed $Fe_3O_4$ nanoparticles can explain this outstanding activity on RGO sheets, BET surface area (74 $m^2.g^{-1}$), and narrower bandgap.

The magnetic properties of the nanocomposites, proven by the VSM analysis, contributed to facilitate their removal from the system in the reuse tests. Nanocomposite 3 could be reused at least three times without significant activity loss. XPS analysis showed that the $Fe^{3+}/Fe^{2+}$ surface ratio did not change after the third recycle, meaning that RGO sheets are responsible for stabilizing the $Fe_3O_4$ nanoparticles by hindering electron-hole recombination.

In conclusion, $Fe_3O_4$/RGO nanocomposites are proving to be promising photocatalysts. Their physical-chemical properties lead to remarkable dye discoloration results, and their reusability is important in reducing operational costs. Furthermore, their facile synthesis could motivate new studies such as scalability and other applications.

# CONCLUSIONS AND SUGGESTIONS

Based on the work described in both Chapter 1 and 2, this section aims to discuss the conclusions obtained so far. Also, in order to continue and improve this research, some suggestions are included.

## Conclusions

Textile Industry is a sector that is well known for its significant role worldwide. Nevertheless, their dyeing processes are responsible for releasing great amounts of dye-containing wastewater, whereas most of them are related to severe impacts to the environment, and human health. For this reason, designing new technologies aiming to mitigate water pollution is required in contemporary world.

In this work, $Fe_3O_4$/RGO magnetic nanocomposites were successfully synthesized by a Stöber-like method, which was found to be a facile method to anchor semiconductor oxides on graphene-like materials. These magnetic nanocomposites were thoroughly characterized, and evaluated in the photo-Fenton discoloration of indigo carmine, an extensively used dye employed in denim fabrication.

The results described in the first paper showed that the magnetic $Fe_3O_4$/RGO nanocomposite, with ~90%wt of $Fe_3O_4$ and ~10%wt RGO, is promising due to its improved physicochemical properties. For instance, zeta potential of the $Fe_3O_4$/RGO nanocomposite showed to be more positive than the bare RGO, thus improving the attraction between indigo carmine molecule and the nanocomposite. Also, XPS results showed that the $Fe^{3+}/Fe^{2+}$ atomic surface ratio was very similar to the theoretical for $Fe_3O_4$ even after the reuse test. This characteristic can be associated to the presence of RGO in the nanocomposite, which is responsible to hinder the electron-hole recombination, maintaining its activity. Furthermore, VSM analysis showed that the nanocomposite presented a strong magnetic character, yielding to a facile catalyst recovery.

Based on the previous results, the second paper was devoted to study the $Fe_3O_4$:RGO mass ratio, and catalyst/$H_2O_2$ dosages. It was observed by XRD and Mössbauer analysis that decreasing the $Fe_3O_4$ content up to 69%wt (nanocomposite 1) results in not well dispersed iron oxide particles. In addition, it leads to the formation of $\alpha$-$Fe_2O_3$ and non-magnetic $FeO_x$, responsible widening the bandgap, thus reducing its activity. The nanocomposite that presented the best performance (nanocomposite 3), with 88%wt of $Fe_3O_4$, showed rapid

indigo carmine discoloration in optimal conditions. The kinetic data provided in this work Also, the reusability tests showed that the nanocomposite can be reused for at least 3 recycles (4 runs) without losing activity.

In this regard, the results obtained in both works lead to the conclusion that $Fe_3O_4$/RGO nanocomposites, synthesized by the facile Stöber-like method, are promising materials that can be used in dye-containing wastewater remediation. The features presented hereby support that photo-Fenton approach may be an important ally to treat dyeing contamination.

**Suggestions**

Aiming to advance with the research described hereby, follow are some suggestions:

- Synthesize, characterize, and evaluate new $Fe_3O_4$/RGO nanocomposites, reducing the $Fe_3O_4$ content, to better understand the $Fe_2O_3$ and $FeO_x$ formation.
- Perform new IC discoloration tests collecting aliquots in regular time intervals before turning the light source on. This proposal will provide new insights about the adsorption character of these materials.
- Select the optimal conditions with the nanocomposite that presented the best activity and monitor de Total Organic Carbon (TOC) removal. This action will prove if these nanocomposites are effective in IC mineralization, and not only discoloration.

# REFERENCES


ABIT - ASSOCIAÇÃO BRASILEIRA DA INDÚSTRIA TÊXTIL E CONFECÇÃO. *Perfil do setor*, 2023. Disponível em: https://www.abit.org.br/cont/perfil-do-setor. Acesso em: 8 mai. 2023.

ACHIENG, G.O.; KOWENJE, C.O.; LALAH, J.O.; OJWACH, S.O. Synthesis and characterization of FSB@$Fe_3O_4$ composites and application in removal of indigo carmine dye from industrial wastewaters. *Environmental Science and Pollution Research*, v. 28, p. 54876-54890, 2021.

AGORKU, E.S.; MAMO, M.A.; MAMBA, B.B.; PANDEY, A.C.; MISHRA, A.K. Cobalt-doped ZnS-reduced graphene oxide nanocomposite as an advanced photocatalytic material. *Journal of Porous Materials*, v. 22, p. 47-56, 2015a.

AGORKU, E.S.; MAMO, M.A.; MAMBA, B.B.; PANDEY, A.C.; MISHRA, A.K. Palladium-decorated zinc sulfide/reduced graphene oxide nanocomposites for enhanced visible light-driven photodegradation of indigo carmine. *Materials Science in Semiconductor Processing*, v. 33, p. 119-126, 2015b.

AL KAUSOR, M.; CHAKRABORTTY, D. Graphene oxide based semiconductor photocatalysts for degradation of organic dye in waste water: A review on fabrication, performance enhancement and challenges. *Inorganic Chemistry Communication*, v. 129, n. 108630, 2021.

ALCOCER, S.; PICOS, A.; URIBE, A.R.; PÉREZ, T.; PERALTA-HERNÁNDEZ, J.M. Comparative study for degradation of industrial dyes by electrochemical advanced oxidation processes with BDD anode in a laboratory stirred tank reactor. *Chemosphere*, v. 205, p. 682-689, 2018.

ALEBOYEH, A.; ALEBOYEH, H.; MOUSSA, Y. Decolorisation of acid blue 74 by ultraviolet/$H_2O_2$. *Environmental Chemistry Letters*, v. 1, p. 161-164, 2003.

AMBROSI, A.; CHUA, C.K.; LATIFF, N.M.; LOO, A.H.; WONG, C.; ENG, A.; BONANNI, A.; PUMERA, M. Graphene and its electrochemistry - an update. *Chemical Society Reviews*, v. 45, p. 2458-2493, 2016.

AMMAR, S.; ABDELHEDI, R.; FLOX, C.; ARIAS, C.; BRILLAS, E. Electrochemical degradation of the dye indigo carmine at boron-doped diamond anode for wastewaters remediation. *Environmental Chemistry Letters*, v. 4, p. 229-233.

ANSARI, S.A. Elemental semiconductor red phosphorus/ZnO nanohybrids as high performance photocatalysts. *Ceramics International*, v. 49, p. 17746-17752, 2023.

ANSARI, S.A.; KUMAR, R.; BARAKAT, M.A.; CHO, M.H. Simple and sustainable route for large scale fabrication of few layered molybdenum disulfide sheets towards superior adsorption of the hazardous organic pollutant. *Journal of Materials Science: Materials in Electronics*, v. 29, p. 7792-7800, 2018.

ANSARI, S.A.; PARVEEN, N.; ALSULAIM, G.M.; ANSARI, A.A.; ALSHARIF, S.A.; ALNAHDI, K.M.; ALALI, H.A.; REDDY, V.R.M. Emerging NiO-rGO nanohybrids for antibiotic pollutant degradation under visible-light irradiation. *Surfaces and Interfaces*, v. 40, n. 103078, 2023.

ARSHAD, A.; IQBAL, J.; AHMAD, I.; ISRAR, M. Graphene/$Fe_3O_4$ nanocomposite: interplay between photo-Fenton type reaction, and carbon purity for the removal of methyl orange. *Ceramics International*, v. 44, n. 3, p. 2643-2648, 2018.

BABU, C.M.; VINODH, R.; SELVAMANI, A.; KUMAR, K.P.; PARVEEN, A.S.; THIRUKUMARAN, P.; SRINIVASAN, V.V.; BALASUBRAMANIAM, R.; RAMKUMAR, V. Organic functionalized $Fe_3O_4$/RGO nanocomposites for $CO_2$ adsorption. *Journal of Environmental Chemical Engineering*, v. 5, p. 2440-2447, 2017.

BAGRI, A.; MATTEVI, C.; ACIK, M.; CHABAL, Y.J.; CHOWALLA, M.; SHENOY, V.B. Structural evolution during the reduction of chemically derived graphene oxide. *Nature Chemistry*, v. 2, p. 581-587, 2010.

BARKA, N.; ASSABBANE, A.; NOUNAH, A.; ICHOU, Y.A. Photocatalytic degradation of indigo carmine in aqueous solution by $TiO_2$-coated non-woven fibres. *Journal of Hazardous Materials*, v. 152, p. 1054-1059, 2008.

BEATTIE, I.R.; GILSON, T.R.; The single-crystal Raman spectra of nearly opaque materials. Iron(III) oxide and chromium(III) oxide. *Journal of the Chemical Society A: Inorganic, Physical, Theoretical*, p. 980-986, 1970.

BERTRAN, A.; SANDOVAL, S.; ORÓ-SOLÉ, J.; SÁNCHEZ, A.; TOBIAS, G. Particle size determination from magnetization curves in reduced graphene oxide decorated with monodispersed superparamagnetic iron oxide nanoparticles. *Journal of Colloid and Interface Science*, v. 566, p. 107-119, 2020.

BIESINGER, M.C.; PAYNE, B.P.; GROSVENOR, A.P.; LAU, L.W.M.; GERSON, A.R.; SMART, R.S.C. Resolving surface chemical states in XPS analysis of first row transition metals, oxides and hydroxides: Cr, Mn, Fe, Co and Ni. *Applied Surface Science*, v. 257, p. 2717-2730, 2011.

BORUAH, P.K.; SHARMA, B.; KARBHAL, I.; SHELKE, M.V.; Ammonia modified graphene sheets decorated with magnetic $Fe_3O_4$ nanoparticles for the photocatalytic and photo-Fenton degradation of phenolic compounds under sunlight irradiation. *Journal of Hazardous Materials*, v. 325, p. 90-100, 2017.

BORUAH, P.K.; DIPANKAR, B.J.; HANDIQUE, J.; SHARMA, P.; SENGUPTA, P.; DAS, M.R. Facile synthesis and characterization of $Fe_3O_4$ nanopowder and $Fe_3O_4$/reduced graphene oxide nanocomposite for methyl blue adsorption: a comparative study. *Journal of Environmental Chemical Enginnering*, v. 3, n. 3, p. 1974-1985, 2015.

CASAXPS. *Processing software for XPS, AES, SIMS and more*, 2018. Disponível em: http://www.casaxps.com. Acesso em: 5 dec. 2019.

CHENG, J.P.; SHOU, Q.L.; WUB, J.S.; LIU, F.; DRAVID, V.P.; ZHANG, X.B. Influence of component content on the capacitance of magnetite/reduced graphene oxide composite, *Journal of Electroanalytic Chemistry*, v. 968, p. 1-8, 2013.

CHOI, S.M.; SEO, M.H.; KIM, W.B. Synthesis of surface-functionalized graphene nanosheets with high Pt-loadings and their applications to methanol electrooxidation. *Carbon*, v. 49, p. 904-909, 2011.

COELHO, M.G.; DE LIMA, G.M.; AUGUSTI, R.; MARIA, D.A.; ARDISSON, J.D. New materials for photocatalytic degradation of Indigo Carmine-Synthesis, characterization and catalytic experiments of nanometric tin dioxide-based composites. *Applied Catalysis B: Environmental*, v. 96, p. 67-71, 2010.

COSME-TORRES, I.; MACEDO-MIRANDA, M.G.; MARTINEZ-GALLEGOS, S.M.; GONZÁLEZ-JUÁREZ, J.C.; ROA-MORALES, G.; ILLESCAS-MARTÍNEZ, F.J.; IBARRA-ESCUTIA, P. Heterogeneous photo-Fenton treatment for degradation of indigo carmine dye. *MRS ADVANCES*, v. 4, p. 3281-3289, 2019.

COSTA, G.P.; RAFAEL, R.A.; SOARES, J.C.S.; GASPAR, A.B.; Synthesis and characterization of $ZnO-Nb_2O_5$ catalysts for photodegradation of bromophenol blue. *Catalysis Today*, v. 344, p. 240-246, 2020.

COSTA, T.R.; BALDI, E.; FIGUEIRÓ, A.; COLPANI, G.L.; SILVA, L.L.; ZANETTI, M.; DE MELLO, J.M.M.; FIORI, M.A. $Fe_3O_4$@C core-shell nanoparticles as adsorbent of ionic zinc: evaluating of the adsorptive capacity. *Materials Research*, v. 22(suppl. 1), n. e20180847, 2019.

DASTGERDI, Z.H.; MESHKAT, S.S.; ESRAFILI, M.D. Enhanced adsorptive removal of Indigo carmine dye performance by functionalized carbon nanotubes based adsorbents from aqueous solution: equilibrium, kinetic, and DFT study. *Journal of Nanostructure in Chemistry*, v. 9, p. 323-334, 2019.

DAUD, N.K.; HAMEED, B.H. Acid Red 1 dye decolorization by heterogeneous Fenton-like reaction using Fe/kaolin catalyst. *Desalination*, v. 269, p. 291-293, 2011.

DÉZSI, I.; FETZER, Cs.; GOMBKÖTŐ, Á.; SZŰCS, I.; GUBICZA, J.; UNGÁR, T. Phase transition in nanomagnetite. *Journal of Applied Physics*, v. 103, n. 104312, 2008.

DONG, X.; LI, L.; ZHAO, C.; LIU, H.K.; GUO, Z. Controllable synthesis of RGO/FexOy nanocomposites as high-performance anode materials for lithium ion batteries. *Journal of Materials Chemistry A*, v. 2, p. 9844-9850, 2014.

EROI, S.N.; ELLO, A.S.; DIABATÉ, D.; OSSONON, D.B. Heterogeneous $WO_3/H_2O_2$ system for degradation of Indigo Carmin dye from aqueous solution. *South African Journal of Chemical Engineering*, v. 37, p. 53-60, 2021.

FAN, W.; ZHANG, C.; TJIU, W.W.; LIU, T. Fabrication of electrically conductive graphene/polystyrene composites via a combination of latex and layer-by-layer assembly approaches. *Journal of Materials Research*, v. 28, n. 4, 2013.

FERREIRA, F.N.; BENEVIDES, A.P.; CESAR, D.V.; LUNA, A.S.; GOIS, J.S. Magnetic solid-phase extraction and pre-concentration of 17β-estradiol and 17α-ethinylestradiol in tap water using maghemite-graphene oxide nanoparticles and determination using HPLC with fluorescence detector. *Microchemical Journal*, v. 157, n. 104947, 2020.

FLOX, C.; AMMAR, S.; ARIAS, C.; BRILLAS, E.; VARGAS-ZAVALA, A.V.; ABDELHEDI, R. Electro-Fenton and photoelectro-Fenton degradation of indigo carmine in acidic aqueous medium. *Applied Catalysis B*, v. 67, p. 93-104, 2006.

GALINDO, C.; JACQUES, P.; KALT, A.; Photochemical and photocatalytic degradation of an indigoid dye: a case study of acid blue 74 (AB74). *Journal of Photochemistry and Photobiology A: Chemistry*, v. 141, n. 1, p. 47-56, 2001.

GEIM, A.K.; NOVOSELOV, K.S. The rise of graphene. *Nature Materials*, v. 6, p. 183-191, 2007.

GHANDOOR, H.E.; ZIDAN, H.M.; KHALIL, M.M.H.; ISMAIL, M.I.M. Synthesis and some physical properties of magnetite ($Fe_3O_4$) nanoparticles. *International Journal of Electrochemical Science*, v. 7, p. 5734-5745, 2012.

GIOIA, L.; OVSEJEVI, K.; MANTA, C.; MÍGUEZ, D.; MENÉNDEZ, P. Biodegradation of acid dyes by an immobilized laccase: an ecotoxicological approach. *Environmental Science: Water Research & Technology*, v. 4, p. 2125-2135, 2018.

GONÇALVES, A.H.A.; SICILIANO, P.H.C.; ALVES, O.C.; CESAR, D.V.; HENRIQUES, C.A.; GASPAR, A.B. Synthesis of a magnetic $Fe_3O_4$/RGO composite for the rapid photo-Fenton discoloration of indigo carmine dye. *Topics in Catalysis*, v. 63, p. 1017-1029, 2020.

GONÇALVES, A.H.A.; SICILIANO, P.H.C.; MOREIRA, C.R.; ALVES, O.C.; CAYTUERO, A.; SAITOVITCH, E.M.B.; LITTERST, F.J.; CESAR, D.V.; HENRIQUES, C.A.; GASPAR, A.B. Effect of $Fe_3O_4$:RGO ratios in magnetic nanocomposites applied for dye discoloration. *Journal of the Brazilian Chemical Society*, v.35(9), n. e-20240045, p. 1-16, 2024.

GONÇALVES, N.P.F.; MINELLA, M.; FABBRI, D.; CALZA, P.; MALISTESTA, C.; MAZZOTTA, E.; PREVOT, A.B. Humic acid coated magnetic particles as highly efficient heterogeneous photo-Fenton materials for wastewater treatments. *Chemical Engineering Journal*, v. 390, n. 124619, 2020.

HADJLTAIEF, H.B.; BAIRQ, Z.A.S.; SHI, C.; BENZINA, M. Evaluation of sono-assisted solar/Fenton process for indigo carmine degradation over magnetic ZnO-$Fe_3O_4$ supported Tunisian kaolinite clay. *Surface and Interfaces*, v. 26, n. 101395, 2021.

HAI, F.I.; YAMAMOTO, K.; NAKAJIMA, F.; FUKUSHI, K.; NGHIEM, L.D.; PRICE, W.E.; JIN, B. Degradation of azo dye acid orange 7 in a membrane bioreactor by pellets and attached growth of coriolus versicolour. *Bioresource Technology*, v. 141, p. 29-34, 2013.

HAN, R.; LI, W.; PAN, W.; ZHU, M.; ZHOU, D.; LI, F. 1D Magnetic materials of $Fe_3O_4$ and Fe with high performance of microwave absorption fabricated by electrospinning method. *Scientific Reports*, v. 4, n. 7493, 2014

HANEEF, M.; SALEEM, H.; HABIB, A. Use of graphene nanosheets and barium titanate as fillers in PMMA for dielectric applications. *Synthetic Metals*, v. 223, p. 101-106, 2017.

HONG, D.; YAMADA, Y.; NAGATOMI, T.; TAKAI, Y.; FUKUZUMI, S. Catalysis of Nickel Ferrite for Photocatalytic Water Oxidation Using $[Ru(bpy)_3]^{2+}$ and $S_2O_8^{2-}$. *Journal of the American Chemical Society*, v. 134, n. 48, p. 19572-19575, 2012.

HSIEH, S.; LIN, P.Y.; FePt nanoparticles as heterogeneous Fenton-like catalysts for hydrogen peroxide decomposition and the decolorization of methylene blue. *Journal of Nanoparticle Research*, v. 14, n. 956, 2012.

HU, C.; XUE, J.; DONG, L.; JIAN, Y.; WANG, X.; QU, L.; DAI, L. Scalable Preparation of Multifunctional Fire-Retardant Ultralight Graphene Foams. *ACS Nano*, v. 10, n. 1, p. 1325-1332, 2016.

HUANG, H.; LI, Z.; SHE, J.; WANG, W. Oxygen density dependent band gap of reduced graphene oxide. *Journal of Applied Physics*, v. 111, n. 054317, 2012.

IEMI – INTELIGÊNCIA DE MERCADO. *Brasil Têxtil 2022*. Disponível em: https://www.iemi.com.br/produto/brasil-textil/. Acesso em: 8 mai. 2023.

IQBAL, R.M.; WARDANI, D.A.P.; HAKIM, L.; DAMSYIK, A.; SAFITRI, R.; FANSURI, H. The structural and optical band gap energy evaluation of $TiO_2$-$Fe_2O_3$ nanocomposite. *IOP Conference Series Materials Science and Engineering*, v. 833, n. 012072, 2020.

JENKINS, C.L. Textile dyes are potential hazards. *Journal of Environmental Health*, v. 40, p. 7-12, 1978.

JI, F.; LI, C.; ZHANG, J.; DENG, L. Efficient decolorization of dye pollytants with $LiFe(WO_4)_2$ as a reusable heterogeneous Fenton-like catalyst. *Desalination*, v. 269, p. 284-290, 2011.

JIANG, X.; LI, L.; CUI, Y.; CUI, F. New branch on old tree: green-synthesized RGO/$Fe_3O_4$ composite as a photo-Fenton catalyst for rapid decomposition of methylene blue. *Ceramics International*, v. 43, n. 16, p. 14361-14368, 2017.

JIN, Y.; ZHENG, Y.; PODKOLZIN, S.G.; LEE, W. Band gap of reduced graphene oxide tuned by controlling functional groups. *Journal of Materials Chemistry C*, v. 8, p. 4885-4894, 2020.

JOHRA, F.T.; LEE, J.W.; JUNG, W.G. Facile and safe graphene preparation on solution based platform. *Journal of Industrial and Engineering Chemistry*, v. 20, p. 2883-2887, 2014.

JOZWIAK, W.K.; KACZMAREK, E.; MANIECKI, T.P.; IGNACZAK, W.; MANIUKIEWICZ, W. Reduction behavior of iron oxides in hydrogen and carbon monoxide atmospheres. *Applied Catalysis A: General*, v. 326, p. 17-27, 2007.

KHAN, M.A.M.; KHAN, W.; AHAMED, M.; ALHAZAA, A.N. Investigation on the structure and physical properties of $Fe_3O_4$/RGO nanocomposites and their photocatalytic application. *Materials Science in Semiconductor Processing*, v. 99, p. 44-53, 2019.

KHANH, D.N.N.; THO, N.T.M.; THANG, N.Q.; TIEN, N.T.; PHONG, C.T.; CANG, M.H.; PHUONG, N.T.K. Synthesis, characterization and photocatalytic activity of novel mixed metal oxides/reduced graphene oxide hybrid catalysts. *Vietnam Journal of Science and Technology*, v. 57, n. 5, p. 572-584, 2019.

KIM, H.K.; ARAVINDAN, V.; ROH, M.H.K.; LEE, K.; JUNG, M.H.; MADHAVI, S.; ROH, K.C.; KIM, K.B. Exploring high-energy Li-I(r)on batteries and capacitors with conversion-type $Fe_3O_4$-rGO as the negative electrode. *ChemElectroChem*, v. 4, p. 2626-2633, 2017.

KLENCSÁR, Z.; ÁBRAHÁM, A.; SZABÓ, L.; SZABÓ, E.G.; STICHLEUTNER, S.; KUZMANN, E.; HOMONNAY, Z.; TOLNAI, G. The effect of preparation conditions on magnetite nanoparticles obtained via chemical co-precipitation. *Materials Chemistry and Physics*, v. 223, p. 122-132, 2019.

KLENCSÁR, Z.; KUZMANN, E.; VÉRTES, A. User-friendly software for Mössbauer spectrum analysis. *Journal of Radioanalytical and Nuclear Chemistry*, v. 210, p. 105-118, 1996.

KONG, C.; LI, M.; LI, J.; MA, X.; FENG, C.; LIU, X. One-step synthesis of $Fe_2O_3$ nano-rod modified reduced graphene oxide composites for effective Cr(VI) removal: removal capability and mechanism. *RSC Advances*, v. 9, p. 20582-20592, 2019.

KUBELKA, P.; MUNK, F. Ein Beintrag zur Optik der Farbanstriche. *Zeitschrift für Technische Physik*, v. 12, p. 593-601, 1931.

KUDIN, K.N.; OZBAS, B.; SCHNIEPP, H.C.; PRUD'HOMME, R.K.; AKSAY, I.A.; CAR, R. Raman spectra of graphite oxide and functionalized graphene sheets. *Nano Letters*, v. 8, n. 1, p. 36-41, 2008.

KULKARNI, S.A.; SAWADH, P.S.; PALEI, P.K.; KOKATE, K.K. Effect of synthesis route on the structural, optical and magnetic properties of $Fe_3O_4$ nanoparticles. *Ceramics International*, v. 40, p. 1945-1949, 2013.

KURT, B.Z.; DURMUS, Z.; DURMUS, A.; Preparation and characterization of platinum (Pt) and palladium (Pd) nanoparticle decorated graphene sheets and their utilization for the elimination of basic fuchsin and indigo carmine dyes. *Solid State Sciences*, v. 51, p. 51-58, 2016.

LATORRE-SANCHEZ, M.; PRIMO, A.; GARCIA, H. Green synthesis of $Fe_3O_4$ nanoparticles embedded in a porous carbon matrix and its use as anode material in Li-ion batteries. *Journal of Materials Chemistry*, v. 22, n. 21373, p. 21373-21375, 2012.

LI, B.; XU, H.Y.; LIU, Y.L.; LIU, Y.; XU, Y.; ZHANG, S.Q. Unveiling the structure-activity relationships of ofloxacin degradation by $CO_3O_4$-activated peroxymonosulfate: from microstructures to exposed facets. *Chemical Engineering Journal*, v. 467, n. 143396, 2023.

LI, H.; LI, Y.; XIANG, L.; HUANG, Q.; QIU, J.; ZHANG, H.; SIVAIAH, M.V.; BARON, F.; BARRAULD, J.; PETIT, S.; VALANGE, S. Heterogeneous photo-Fenton decolorization of orange II over Al-pillared Fe-smectite: response surface approach, degradation pathway, and toxicity evaluation. *Journal of Hazardous Materials*, v. 287, 32-41, 2015.

LI, Y.; ZHANG, F.S. Catalytic oxidation of Methyl Orange by an amorphous FeOOH catalyst developed from a high iron-containing fly ash. *Chemical Engineering Journal*, v. 158, n. 2, p. 148-153, 2010.

LIN, S.H.; LIN, C.M. Treatment of textile waste effluents by ozonation and chemical coagulation. *Water Research*, v. 27, n. 12, p. 1743-1748, 1993.

LIU, H.; WANG, K.; ZHANG, D.; ZHAO, D.; ZHAI, J.; CUI, W. Adsorption and catalytic removal of methyl orange from water by PIL-GO/$TiO_2$/$Fe_3O_4$ composites. *Materials Science in Semiconductor Processing*, v. 154, n. 107215, 2023.

LIU, Y.; JIN, W.; ZHAO, Y.; ZHANG, G.; ZHANG, W.; Enhanced catalytic degradation of methylene blue by α-$Fe_2O_3$/graphene oxide via heterogeneous photo-Fenton reactions. *Applied Catalysis B: Environmental*, v. 206, p. 642-652, 2017.

MADHUVILAKKU, R.; ALAGAR, S.; MARIAPPAN, R.; PIRAMAN, S. Green one-pot synthesis of flowers-like $Fe_3O_4$/rGO hybrid nanocomposites for effective electrochemical detection of riboflavinand low-cost supercapacitor applications. *Sensors and Actuators B: Chemical*, v.253, p. 879-892, 2017.

MAKSOUD, M.I.A.A.; ELGARAHY, A.M.; FARRELL, C.; AL-MUHTASEB, A.H.; ROONEY, D.W.; OSMAN, A.I. Insight on water remediation application using magnetic nanomaterials and biosorbents. *Coordination Chemistry Reviews*, v. 403, n. 213096, 2020.

MATHUR, N.; BHATNAGAR, P.; NAGAR, P.; BIJARNIA, M.K. Mutagenicity assessment of effluents from textile/dye industries of Sanganer, Jaipur (India): a case study, *Ecotoxicology and Environmental Safety*, v. 61, p. 105-113, 2005.

MITTAL, A.; MITTAL, J.; KURUP, L. Batch and bulk removal of hazardous dye, indigo carmine from wastewater through adsorption. *Journal of Harzardous Materials*, v. B137, p. 591-602, 2006.

MOUSSAVI, G.; MAHMOUDI, M. Removal of azo and anthraquinone reactive dyes from industrial wastewaters using MgO nanoparticles. *Journal of Hazardous Materials*, v. 168, p. 806-812, 2009.

MURAD, E. Clays and clay minerals: what can Mössbauer spectroscopy do to help understand them? *Hyperfine Interactions*, v. 117, p. 39-70, 1998.

NIETO-JUAREZ, J.I.; KOHN, T. Virus removal and inactivation by iron (hydr)oxide-mediated Fenton-like processes under sunlight and in the dark. *Photochemical & Photobiological Sciences*, v. 12, p. 1596-1605, 2013.

OLIVEIRA, W.L.; FERREIRA, M.A.; MOURÃO, H.A.J.L.; PIRES, M.J.M.; FERREIRA, V.; GORGULHO, H.F.; CIPRIANO, D.F.; FREITAS, J.C.C.; MASTELARO, V.R.; NASCIMENTO, O.R.; FERREIRA, D.E.C.; FIORAVANTE, F.R.; PEREIRA, M.C.; DE MESQUITA, J.P. Heterogeneous Fenton-like surface of oxygenated graphitic carbon nitride. *Journal of Colloid and Interface Science*, v. 587, p. 479-488, 2021.

OTHMAN, I.; MOHAMED, R.M.; IBRAHEM, F.M. Study of photocatalytic oxidation of indigo carmine dye on Mn-supported $TiO_2$. *Journal of Photochemistry and Photobiology A: Chemistry*, v. 189, p. 80-85, 2007.

PARVEEN, N.; ALQAHTANI, F.O.; ALSULAIM, G.M.; ALSHARIF, S.A.; ALNAHDI, K.M.; ALALI, H.A.; AHMAD, M.M.; ANSARI, S.A. Emerging mesoporous polyacrylamide/gelatin-iron lanthanum oxide nanohybrids towards the antibiotic drugs removal from the wastewater. *Nanomaterials*, v. 13, n. 2835, 2023.

PETRYCHUK, M.; KOVALENKO, V.; PUD, A.; OGURTSOV, N.; GUBIN, A. Ternary magnetic nanocomposites based on core–shell $Fe_3O_4$/polyaniline nanoparticles distributed in PVDF matrix. *Physica Status Solidi A*, v. 207, n. 2, p. 442-447, 2010.

QIN, Y.; LONG, M.; TAN, B.; ZHOU, B. RhB adsorption performance of magnetic adsorbent $Fe_3O_4$/ RGO composite and its regeneration through a Fenton-like reaction. *Nano-Micro Letters*, v. 6, n. 2, p. 125-135, 2013.

QIU, B.; LI, Q.; SHEN, B.; XING, M. Stöber-like method to synthesize ultradispersed $Fe_3O_4$ nanoparticles on graphene with excelente photo-Fenton reaction and high-performance lithium storage. *Applied Catalysis B: Environmental*, v. 183, p. 216-223, 2016.

QUARTARONE, G.; BELLOMI, T.; ZINGALES, A. Inhibition of copper corrosion by isatin in aerated 0.5 M $H_2SO_4$. *Corrosion Science*, v. 45, p. 715-733, 2003.

RADÓN, A.; DRYGALA, A.; HAWEŁEK, Ł.; ŁUKOWIEC, D. Structure and optical properties of $Fe_3O_4$ nanoparticles synthesized by co-precipitation method with different organic modifiers. *Materials Characterization*, v. 131, p. 148-156, 2017.

RAFAEL, R.A.; NORONHA, F.B.; GASPAR, A.B. Synthesis and characterization of Ti-$Nb_2O_5$ catalysts for discoloration reaction of bromophenol blue and indigo carmine dyes. *Topics in Catalysis*, v. 63, p. 1066-1076.

RAO, C.N.R.; BISWAS, K.; SUBRAHMANYAM, K.S.; GOVINDARAJ, A. Graphene, the new nanocarbon. *Journal of Materials Chemistry*, v. 19, p. 2457-2469, 2009.

RAY, S.K.; DHAKAL, D.; LEE, S.W. Visible light driven Ni-$BaMo_3O_{10}$ photocatalyst for indigo carmine degradation: mechanism and pathways. *Materials Science in Semiconductor Processing*, v. 105, n. 104697, 2020.

RUFUSS, D.D.W.; INIYAN, S.; SUGANTHI, L.; DAVIESC, P.A.; Low mass fraction impregnation with graphene oxide (GO) enhances thermo-physical properties of paraffin for heat storage applications. *Thermochimica Acta*, v. 655, p. 226-233, 2017.

SADEGH, F.; POLITAKOS, N.; ROMÁN, E.G.S.; SANZ, O.; PEREZ-MIQUEO, I.; MOYA, S.E.; TOMOVSKA, R. A green synthesis of nanocatalysts based on reduced graphene oxide/magnetic nanoparticles for the degradation of acid red 1. *RSC Advances*, v. 10, n. 38805, 2020.

SADIQ, M.M.J.; SHENOY, U.S.; BHAT, D.K. Enhanced photocatalytic performance of N-doped RGO-$FeWO_4$/$Fe_3O_4$ ternary nanocomposite in environmental applications. *Materials Today Chemistry*, v. 4, p. 133-141, 2017.

SAKAR, M.; PRAKASH, R.M.; DO, T.O. Insights into the $TiO_2$-based photocatalytic systems and their mechanisms. *Catalysts*, v. 9, n. 680, 2019.

SECULA, M.S.; VAJDA, A.; CAGNON, B.; WARMONT, F.; MAMALIGA, I.; Photo-Fenton-peroxide process using Fe(II)-embedded composites based on activated carbon: characterization of catalytic tests. *The Canadian Journal of Chemical Engineering*, v. 98, n. 3, p. 650-658, 2019.

SEE, T.P.; PANDIKUMAR, A.; NGEE, L.H.; MING, H.N.; HUA, C.C. Magnetically separable reduced graphene oxide/iron oxide nanocomposite materials for environmental remediation. *Catalysis Science & Technology*, v. 4, p. 4396-4405, 2014.

SELVARAJ, M.; HAI, A.; BANAT, F.; HAIJA, M.A. Application and prospects of carbon nanostructured materials in water treatment: A review. *Journal of Water Process Engineering*, v. 33, n. 100996, 2020.

SHALABY, A.; NIHTIANOVA, D.; MARKOV, P.; STANEVA, A.D.; IORDANOVA, R.S.; DIMITRIEV, Y.B. Structural analysis of reduced graphene oxide by transmission electron microscopy. *Bulgarian Chemical Communications*, v. 47, n. 1, p. 291-295, 2015.

SHANKER, U.; RANI, M.; JASSAL, V. Degradation of hazardous organic dyes in water by nanomaterials. *Environmental Chemistry Letters*, v. 15, p. 623-642, 2017.

SHEBANOVA, O.N.; LAZOR, P. Raman spectroscopic study of magnetite ($FeFe_2O_4$): a new assignment for the vibrational spectrum. *Journal of Solid State Chemistry*, v. 174, p. 424-430, 2003.

SHEN, J.; SHI, M.; LI, N.; YAN, B.; MA, H.; HU, Y.; YE, M. Facile synthesis and application of Ag-chemically converted graphene nanocomposite. *Nano Research*, v. 3, p. 339-349, 2010.

SHESTAKOVA, M.; SILLANPÄÄ, M.; Removal of dichloromethane from ground and wastewater: a review. *Chemosphere*, v. 93, n. 7, 1258-1267, 2013.

SILVA, M.P.; DE SOUZA, A.C.A.; FERREIRA, L.E.L, NETO, L.M.P.; NASCIMENTO, B.F.; DE ARAÚJO, C.M.B.; FRAGA, T.J.M.; SOBRINHO, M.A.M.; GHISLANDI, M.G. Photodegradation of reactive black 5 and raw textile wastewater by heterogeneous photo-Fenton reaction using amino-$Fe_3O_4$-functionalized graphene oxide as nanocatalyst. *Environmental Advances*, v. 4, n. 100064, 2021.

SOARES, C.P.P.; BAPTISTA, R.L.; CESAR, D.V. Solvothermal reduction of graphite oxide using alcohols. *Materials Research – Ibero American Journal of Materials*, v. 21, n. 1, 2018.

SREEJA, P.H.; SOSAMONY, K.J. A comparative study of homogeneous and heterogeneous photo-Fenton process for textile wastewater treatment, *Procedia Technology*, v. 24, p. 217-223, 2016.

STEURER, P.; WISSERT, R.; THOMANN, R.; MÜLHAUPT, R. Functionalized graphenes and thermoplastic nanocomposites based upon expanded graphite oxide. *Macromolecular Rapid Communications*, v. 30, p. 316-327, 2009.

STREHLOW, W.H.; COOK, E.L. Compilation of energy band gaps in elemental and binary compound semiconductors and insulators. *Journal of Physical and Chemical Reference Data*, v. 2, p. 163-200, 1973.

SU, G.; LIU, L.; ZHANG, L.; LIU, X.; XUE, J.; TANG, A. Fabrication of magnetic $Fe_3O_4$@$SiO_2$@$Bi_2O_2CO_3$/rGO composite for enhancing its photocatalytic performance for organic dyes and recyclability. *Environmental Science and Pollution Research*, v. 28, p. 50286-50301, 2021.

TAUC, J.; GRIGOROVICI, R.; VANCU, A. Optical properties and electronic structure of amorphous germanium. *Physica Status Solidi B*, v. 15, p. 627-637, 1966.

THO, N.T.M.; HUY, B.T.; KHANH, D.N.N.; THANG, N.Q.; DIEU, N.T.P.; DUONG, B.D.; PHUONG, N.T.K. Mechanism of visible-light photocatalytic mineralization of indigo carmine using $ZnBi_2O_4$-$Bi_2S_3$ composites. *Chemistry Select*, v. 3, n. 35, p. 9986-9994, 2018.

UMAR, A.; KUMAR, S.A.; INBANATHAN, S.S.R.; MODARRES, M.; KUMAR, R.; ALGADI, H.; IBRAHIM, A.A.; WENDELBO, R.; PACKIARAJ, R.; ALHAMAMI, M.A.M.; BASKOUTAS, S. Enhanced sunlight-driven photocatalytic, supercapacitor and antibacterial applications based on graphene oxide and magnetite-graphene oxide nanocomposites. *Ceramics International*, v.48, p. 29349-29358, 2022.

VAUTIER, M.; GUILLARD, C.; HERRMAN, J.M. Photocatalytic degradation of dyes in water: case study of indigo and of indigo carmine. *Journal of Catalysis*, v. 201, p. 46-59, 2001.

VERBLE, J.L. Temperature-dependent light-scattering studies of the Verwey transition and electronic disorder in magnetite. *Physical Review B*, v. 9, n. 12. P. 5236-5248, 1974.

WANG, L.; NGUYEN, N.T.; SCHMUKI, P. A facile surface passivation of hematite photoanodes with iron titanate cocatalyst for enhanced water splitting. *ChemSusChem Communications*, v. 9, n. 16, p. 2048-2053, 2016.

WEI, Z.; HUANG, S.; ZHANG, X.; LU, C.; HE, Y. Hydrothermal synthesis and photo-Fenton degradation of magnetic $MnFe_2O_4$/RGO nanocomposites. *Journal of Material Science: Materials in Electronics*, v. 31, p. 5176-5186, 2020.

XU, H.Y.; XU, Y.; ZHANG, S.Q.; DAI, L.Y.; WANG, Y. Fabricating a $Fe_3O_4$@HNTs nanoreactor to expedite heterogeneous fenton-like reactions. *Materials Letters*, v. 337, n. 133985, 2023.

XU, H.Y.; ZHANG, S.Q.; WANG, Y.F.; XU, Y.; DONG, L.M. New insights into the photocatalytic mechanism of pristine ZnO nanocrystals: from experiments to DFT calculations. *Applied Surface Science*, v. 614, n. 156225, 2023.

YANG, X.; CHEN, W.; HUANG, J.; ZHOU, Y.; ZHU, Y.; LI, C. Rapid degradation of methylene blue in a novel heterogeneous $Fe_3O_4$@rGO@TiO2-catalyzed photo-Fenton system. *Scientific Reports*, v. 5, n. 10632, 2015.

YAO, Y.; MIAO, S.; LIU, S.; MA, L.P.; SUN, H.; WANG, S. Synthesis, characterization, and adsorption properties of magnetic $Fe_3O_4$@graphene nanocomposite. *Chemical Engineering Journal*, v. 184, p. 326-332.

YAO, Y.; QIN, J.; CAI, Y.; WEI, F.; LU, F.; WANG, S. Facile synthesis of magnetic $ZnFe_2O_4$–reduced graphene oxide hybrid and its photo-Fenton-like behavior under visible irradiation. *Environmental Science and Pollution Research*, v. 21, n. 12, p. 7296-7306, 2014.

YASEEN, D.A.; SCHOLZ, M. Textile dye wastewater characteristics and constituents of synthetic effluents: a critical review. *International Journal of Environmental Science and Technology*, v. 16, p. 1193-1226, 2019.

YOUNES, S.B.; SAYADI, S. Detoxification of Indigo carmine using a combined treatment via a novel trimeric thermostable laccase and microbial consortium. *Journal of Molecular Catalysis B: Enzymatic*, v. 87, p. 62-68, 2013.

ZAIED, M.; CHUTET, E.; PEULON, S.; BELLAKHAL, N.; DESMAZIÈRES, B.; DACHRAOUI, C.A.; CHAUSSÉ, A. Spontaneous oxidative degradation of indigo carmine by thin films of birnessite electrodeposited onto $SnO_2$. *Applied Catalysis B: Environmental*, v. 107, p. 42-51, 2011.

ZANONI, M.V.B; YAMANAKA, H. Corantes: caracterização química, toxicológica, métodos de detecção e tratamento. 1. ed. São Paulo: Cultura Acadêmica, 2016.

ZARRABI, M.; HAGHIGHI, M.; ALIZADEH, R.; MAHBOOB, S. Hybrid sonoprecipitation fabrication of magnetic ZnO-GO-$Fe_3O_4$ nanophotocatalyst for solar-light-driven degradation of dyes in water. *Materials Research Bulletin*, v. 153, n. 111907, 2022.

ZHANG, S.; SUN, M.; HEDTKE, T.; DESHMUKH, A.; ZHOU, X.C.; WEON, M.; ELIMELECH, J.; KIM, H. Mechanism of heterogeneous fenton reaction kinetics enhancement under nanoscale spatial confinement. *Environmental Science & Technology*, v. 54, n. 17, p. 10868-10875, 2020.

ZHANG, Y.; LI, D.; CHEN, X.; WANG, X.; WANG, S.; Catalytic wet air oxidation of dye pollutants by polyoxomolybdate nanotubes under room condition. *Applied Catalysis B: Environmental*, v. 86, p. 182-189, 2009.

ZHANG, Y.; PAN, C. $TiO_2$/graphene composite from thermal reaction of graphene oxide and its photocatalytic activity in visible light. *Journal of Materials Science*, v. 46, p. 2622-2626, 2011.

ZHAO, B.; LIU, P.; JIANG, Y.; PAN, D.; TAO, H.; SONG, J.; FANG, T.; XU, W. Supercapacitor performances of thermally reduced graphene oxide. *Journal of Power Sources*, v. 198, p. 423-427, 2012.

ZHAO, G.; JIANG, L.; HE, Y.; LI, J.; DONG, H.; WANG, X.; HU, W. Sulfonated graphene for persistent aromatic pollutant management. *Advanced Materials*, v. 23, p. 3959-3963, 2011.

ZHENG, M.; MA. X.; HU, J.; ZHANG, X.; LI, D.; DUAN, W. Novel recyclable BiOBr/$Fe_3O_4$/RGO composites with remarkable visible-light photocatalytic activity. *RSC Advances*, v. 10, n. 19961, 2020.

ZHOU, G.; WANG, D.W.; LI, F.; ZHANG, L.; LI, N.; WU, Z.S.; WEN, L.; LU, G.Q.M.; CHENG, H.M. Graphene-wrapped $Fe_3O_4$ anode material with improved reversible capacity and cyclic stability for lithium ion batteries, *Chemistry of Materials*, v. 22, p. 5306-5313, 2010.

ZHU, Y.; MURALI, S.; CAI, W.; LI, X.; SUK, J.W.; POTTS, J.R.; RUOFF, R.S. Graphene and Graphene Oxide: synthesis, properties, and applications. *Advanced Materials*, v. 22, p. 3906-3924, 2010.

ZUBIR, N.A.; YACOU, C.; MOTUZAS, J.; ZHANG, X.; DA COSTA, J.C.D. Structural and functional investigation of graphene oxide–$Fe_3O_4$ nanocomposites for the heterogeneous Fenton-like reaction. *Scientific Reports*, v. 4, n. 4594, 2014.

**APPENDIX A –** Supplementary Material of Article 2

Table A1 – Compilation of all IC discoloration results in this work (article 2).

| Sample | Catalyst dosage ($g.L^{-1}$) | $[H_2O_2]$ x $10^{-1}$M | Discoloration at t = 5min (%) | $K_{app}$ ($10^{-2}.min^{-1}$)[a] | $R^2$ |
|---|---|---|---|---|---|
| Nanocomposite 3 | 0.07 | 2.3 | 27.8 | 0.89 | 0.99843 |
| | 0.17 | | 33.2 | 1.00 | 0.99062 |
| | 0.33 | | 93.9 | 8.99 | 0.97924 |
| | 0.67 | | 99.9 | - | - |
| | | 1.2 | 87.3 | 6.94 | 0.98439 |
| | 0.33 | 0.6 | 70.1 | 5.02 | 0.99077 |
| | | - | 39.4 | 0.30 | 0.98359 |
| Nanocomposite 2 | 0.67 | 2.3 | 92.5 | - | - |
| | 0.33 | | 90.8 | 8.51 | 0.98311 |
| Nanocomposite 1 | 0.67 | | 98.5 | - | - |
| | 0.33 | | 60.7 | 3.69 | 0.98584 |
| $Fe_3O_4$ | 0.33 | | 62.3 | 6.13 | 0.97818 |
| Photolysis | - | 2.3 | 14.9 | 1.65 | 0.98755 |
| | | 1.2 | 12.6 | 0.55 | 0.97364 |
| | | 0.6 | 8.9 | 0.31 | 0.98073 |

Source: The author, 2023.

[a] pseudo-first-order adjust.

Figure A1 – UV-visible absorption spectra obtained for different IC concentrations.

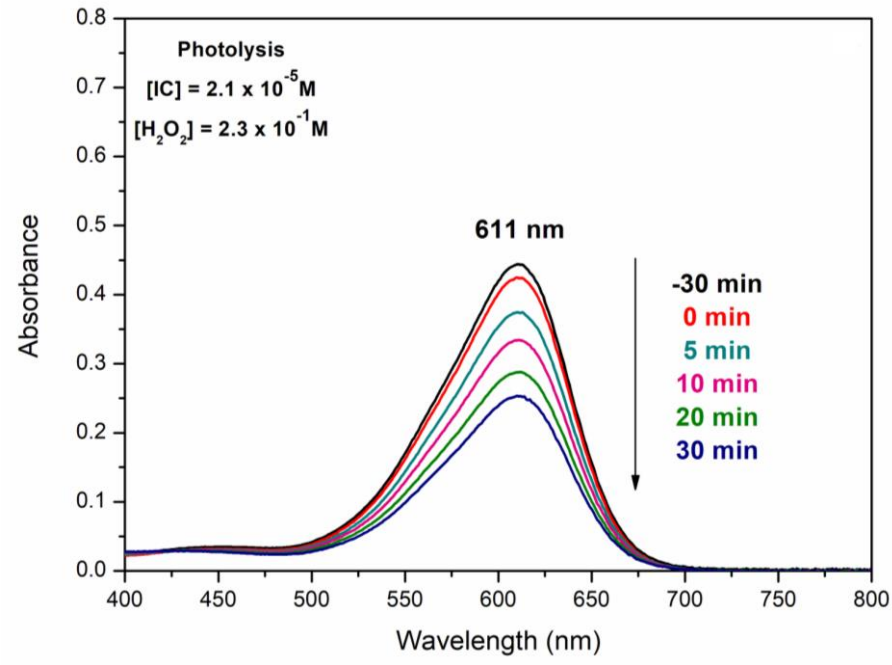


Source: The author, 2023.

Figure A2 – Calibration curve for different IC concentrations of Figure A1.

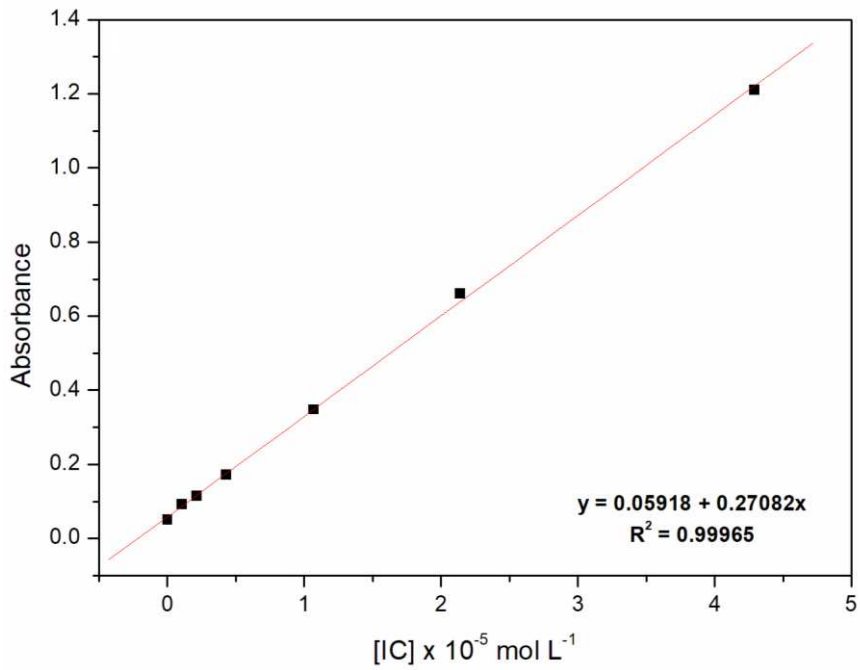


Source: The author, 2023.

Figure A3 – EDX mapping of site 1.

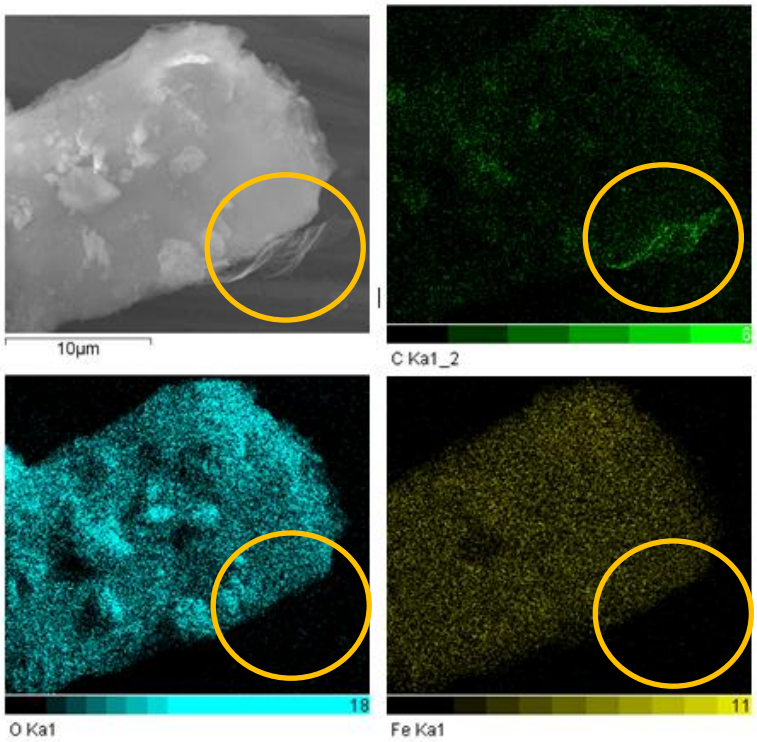


Source: The author, 2023.

Figure A4 – EDX mapping of site 2.

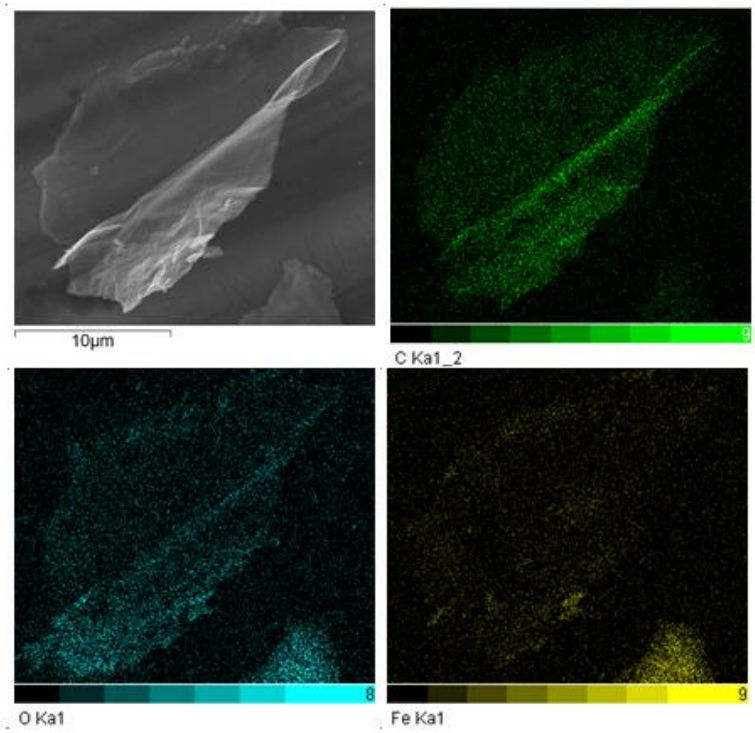


Source: The author, 2023.

Figure A5 – Isotherm plots for all nanocomposites.

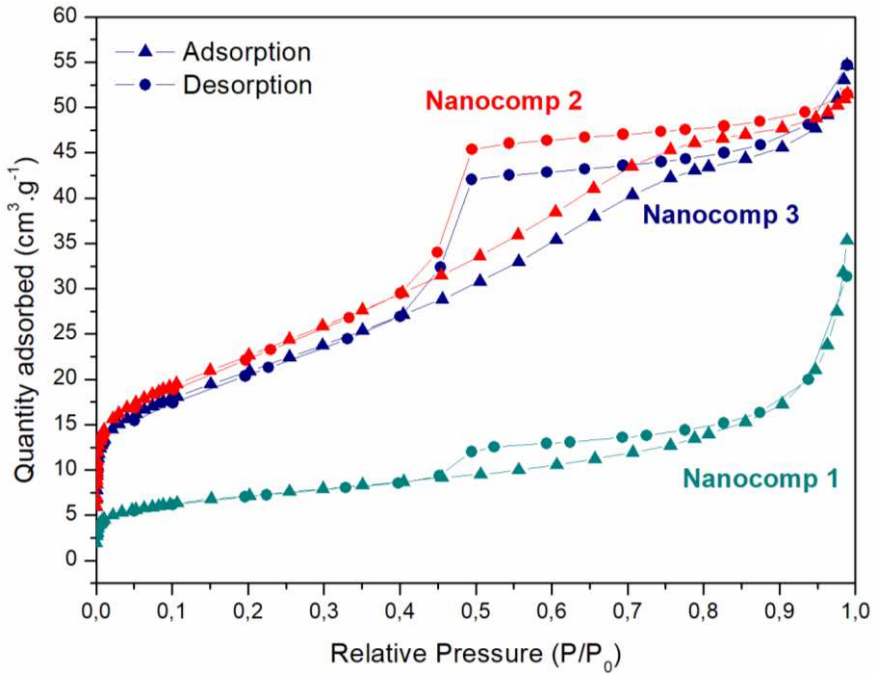


Source: The author, 2023.

Figure A6 – Pore size distribution for all nanocomposites.

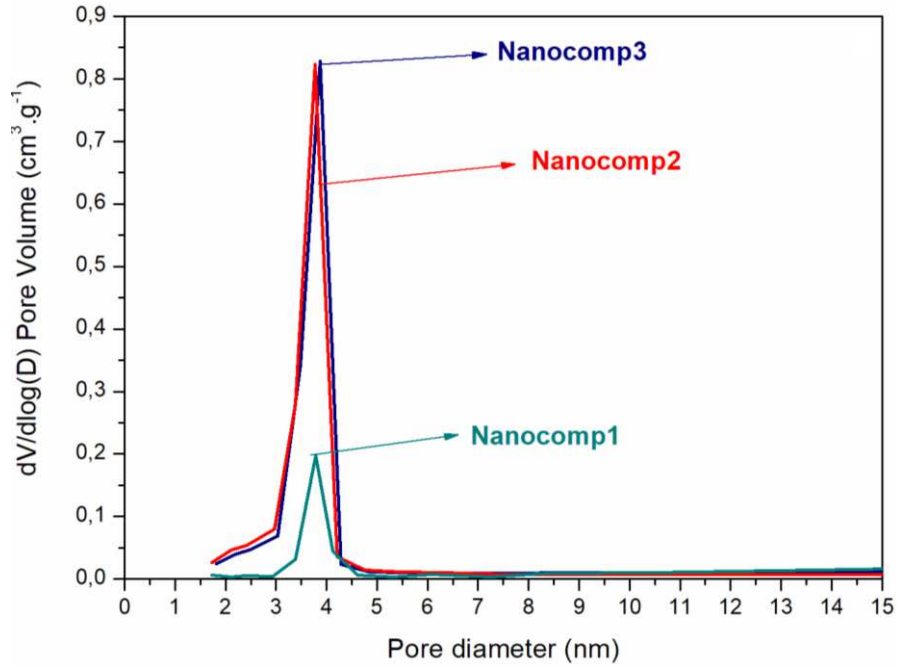


Source: The author, 2023.

Figure A7 – Ln ($C_0$/C) x time kinetic plot for IC discoloration with different $H_2O_2$, in the absence of a heterogeneous catalysts.

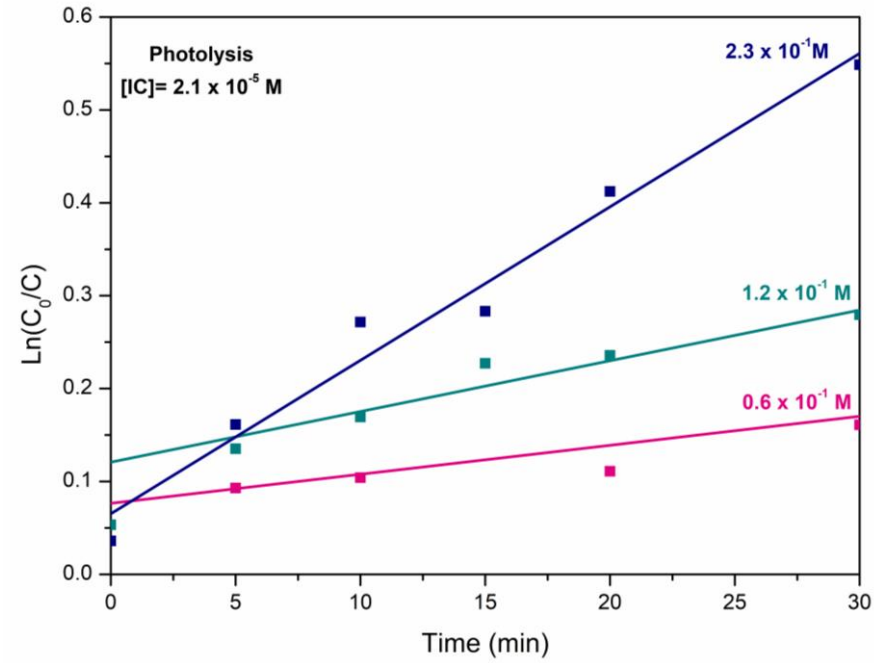


Source: The author, 2023.

Figure A8 – IC discoloration curves for all nanocomposites with a catalyst dosage of 0.67 g.$L^{-1}$, and a fixed $H_2O_2$ concentration of 2.3 x $10^{-1}$M.

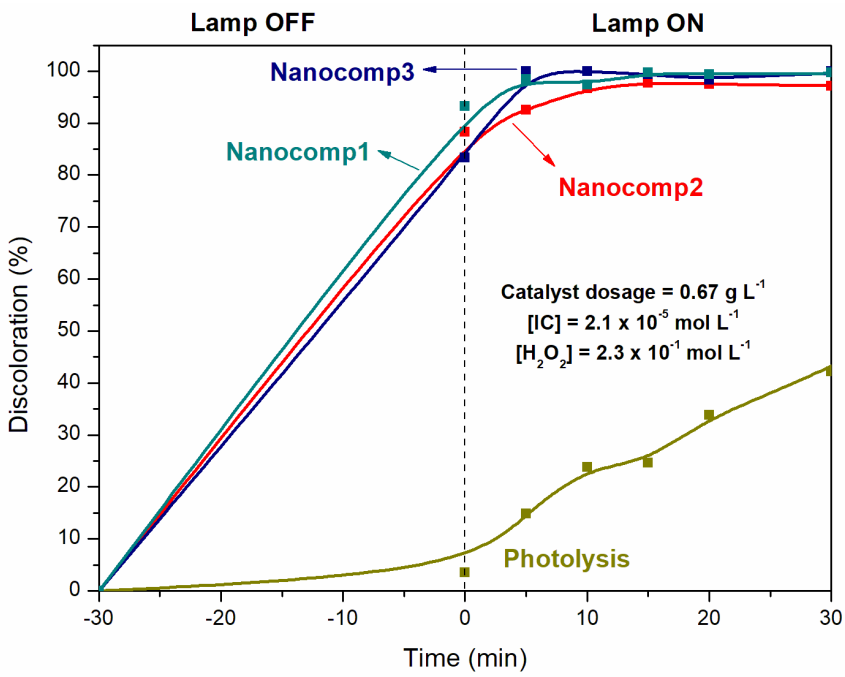


Source: The author, 2023.

Figure A9 – Ln ($C_0$/C) x time kinetic plots for IC discoloration with all nanocomposites (0.33 g.L$^{-1}$), and fixed $H_2O_2$ concentration of 2.3 x 10$^{-1}$ M.

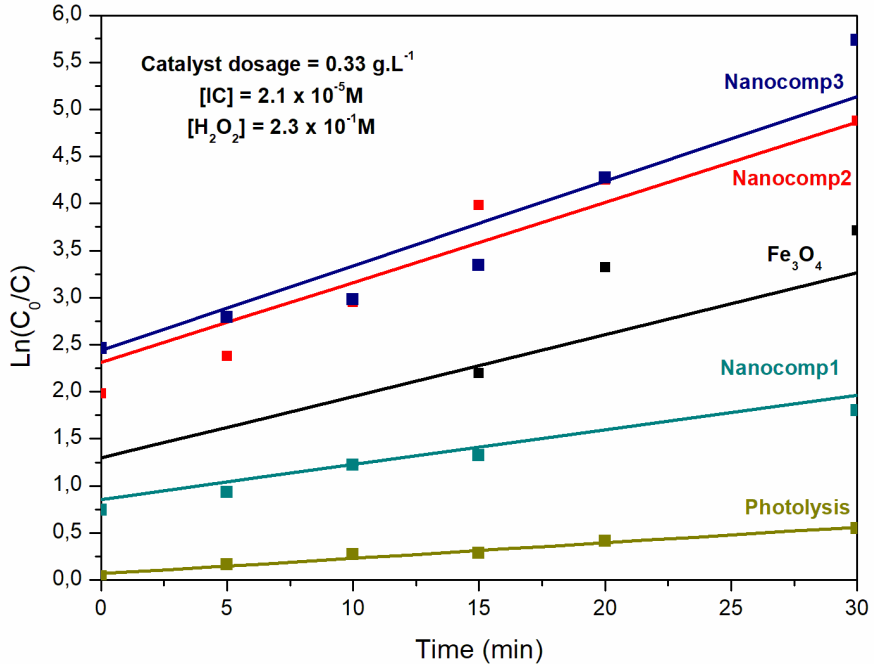


Source: The author, 2023.

Figure A10– Ln ($C_0$/C) x time kinetic plots for different nanocomposite 3 dosages in IC discoloration, with a fixed $H_2O_2$ concentration of 2.3 x 10$^{-1}$.

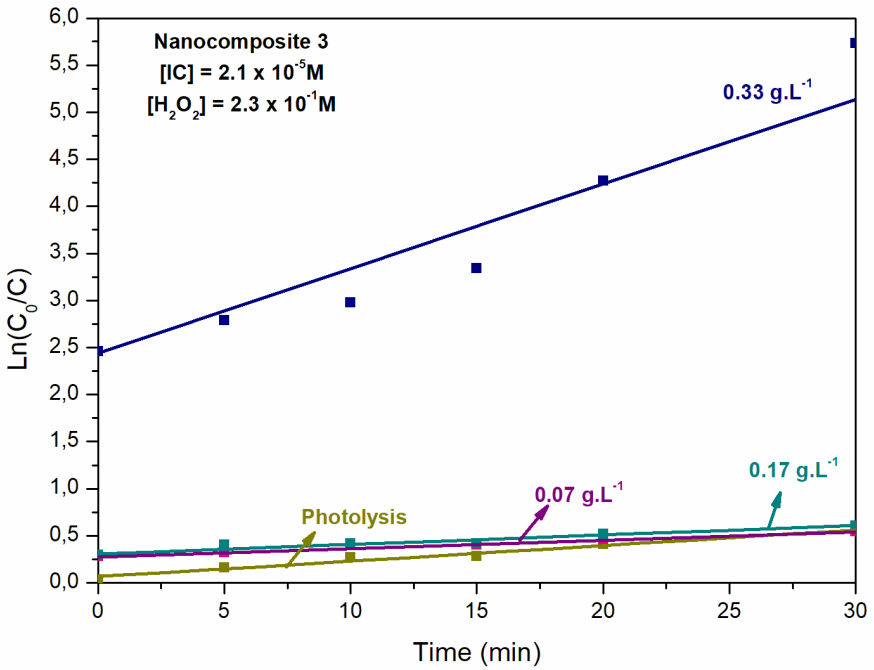


Source: The author, 2023.

Figure A11 – Ln ($C_0$/C) x time kinetic plots for IC discoloration with nanocomposite 3 (0.33 g.L$^{-1}$), with varied $H_2O_2$ concentrations.

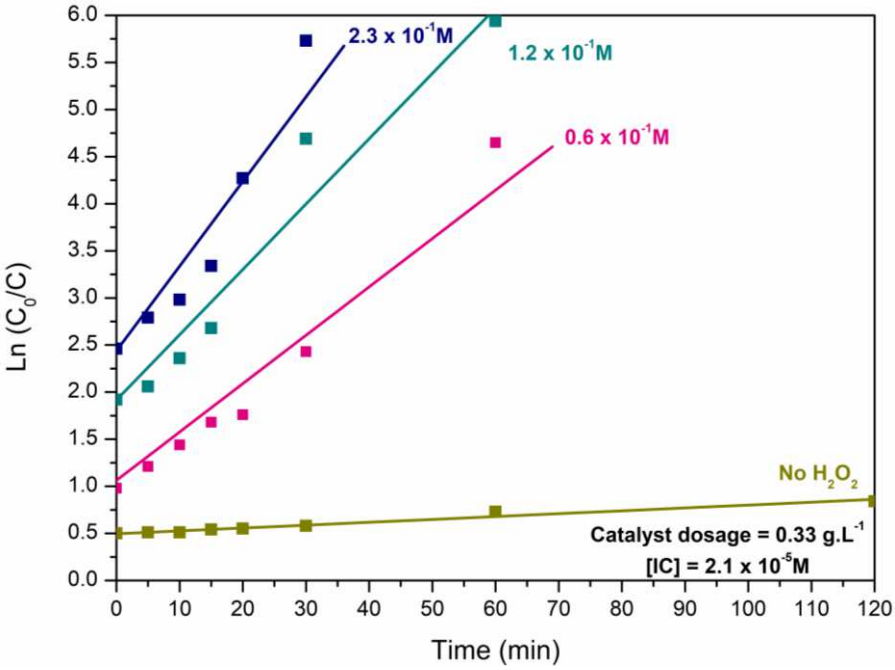


Source: The author, 2023.

**APPENDIX B –** Scientific Production (Journals)

The scientific production developed during the dissertation period is presented hereby. Only the first page of the papers is shown.

**Journal:** Topics in Catalysis, 2020

- Title: Synthesis of a Magnetic $Fe_3O_4$/RGO Composite for the Rapid Photo-Fenton Discoloration of Indigo Carmine. Authors: Arthur H.A. Gonçalves, Pedro H. Siciliano, Odivaldo C. Alves, Deborah V. Cesar, Cristiane A. Henriques, Alexandre B. Gaspar.

**Journal:** Jornal of Brazilian Chemical Society, 2024

- Title: Effect of $Fe_3O_4$/RGO Ratios in Magnetic Nanocomposites Applied for Dye Discoloration. Authors: Arthur H.A. Gonçalves, Pedro H. Siciliano, Bárbara O. da Silva, Carla R. Moreira, Odivaldo C. Alves, Alexander Caytuero, Elisa M.B. Saitovitch, F. Jochen Litterst, Deborah V. Cesar, Cristiane A. Henriques, Alexandre B. Gaspar.

Topics in Catalysis
https://doi.org/10.1007/s11244-020-01277-0

ORIGINAL PAPER

# Synthesis of a Magnetic $Fe_3O_4$/RGO Composite for the Rapid Photo-Fenton Discoloration of Indigo Carmine Dye

Arthur H. A. Gonçalves[1,2] · Pedro H. C. Siciliano[1] · Odivaldo C. Alves[3] · Deborah V. Cesar[2] · Cristiane A. Henriques[2] · Alexandre B. Gaspar[1]



**Abstract**

In the last years, dye wastewater pollution became a major problem due to its toxicity and environmental restrictions. Indigo carmine is an indigoid dye that is largely used, and it is known by its toxicity and stability. In this work, we synthesized a magnetite/reduced graphene oxide ($Fe_3O_4$/RGO) composite with approximately 90%wt of $Fe_3O_4$ and used in the indigo carmine dye photo-Fenton discoloration (accompanied by UV–Vis spectrometry analysis). By using scanning electron microscopy (SEM), X-ray diffractometry (XRD), Laser Raman Spectroscopy (LRS), Magnetization Curves (VSM), and X-ray photoelectron spectroscopy (XPS) analyses it was observed that $Fe_3O_4$ particles of ~ 21 nm were successfully anchored on reduced graphene sheets. Zeta potential showed that the $Fe_3O_4$/RGO composite has a less negative electrostatic behavior in ultrapure water (−46.9 mV) than the bare RGO (−77.7 mV), promoting the attraction of indigo carmine molecule. Magnetic studies proved the ferromagnetic character of the composite with a saturation magnetization of 43 emu/g, thus promoting the easy separation from the reaction medium. In the first 5 min of reaction with the composite, the solution was completely discolored. The composite was recovered, and its reuse also showed total discoloration in the first 30 min of reaction. After first indigo carmine discoloration cycle, XPS results showed that $Fe^{3+}/Fe^{2+}$ atomic ratio was maintained, which can explain the total discoloration in the second cycle.

**Keywords** Reduced graphene oxide · $Fe_3O_4$ · Indigo carmine · Photo-Fenton · Composite · Heterogeneous catalysis · Magnetite

## 1 Introduction

Water pollution caused by dyes has been the focus of much concern over the last years due to the massive amounts used every day, leading to environmental and health complications. Several types of processes are responsible for dye wastewater pollution, being the textile industry the most contributor to this problem [1]. Besides, it is worsened by the high stability of the dyes [2]. Among the variety of dyes on the wastewater pollution, indigo carmine, also called Acid Blue 74, is an indigoid dye that is known by its hazardousness and toxicity [3]. Indigo carmine is carcinogenic and is associated with many other serious health problems [4, 5].

Different processes based on physical–chemical properties have been studied to reduce wastewater pollution by organic dyes [3, 6–9]. Among them, adsorption is one of the most common processes used to remove pollutants from wastewaters, such as drugs, dyes, and others. Maksoud et al. [10] discussed its advantages and disadvantages, focusing on magnetic nanoparticles and bio sorbents. Eco-friendly, low cost, and high efficiency are some properties that characterize them as excellent adsorbents. However, adsorption has several challenges, such as experimental conditions, commercial and disposal issues.

Heterogeneous photocatalytic approach is considered one of the most promising alternatives for wastewater pollution due to many advantages. At first, heterogeneous systems are attractive due to the easy removal from the medium, thus facilitating the catalyst reuse. Also, by using

✉ Alexandre B. Gaspar
alexandre.gaspar@int.gov.br

1 Instituto Nacional de Tecnologia, Av. Venezuela, 82, Sl. 518, Rio de Janeiro, Brazil

2 Instituto de Química, Universidade do Estado do Rio de Janeiro, Rua S. Francisco Xavier, 524, Rio de Janeiro, Brazil

3 Instituto de Química, UFF, Campus do Valonguinho s/n, Niterói, Brazil

Published online: 25 May 2020

Article

Journal of the Brazilian Chemical Society

https://dx.doi.org/10.21577/0103-5053.20240045

J. Braz. Chem. Soc. 2024, 35, 9, e-20240045, 1-16


# Effect of $Fe_3O_4$:RGO Ratios in Magnetic Nanocomposites Applied for Dye Discoloration

*Arthur H. A. Gonçalves,[a,b] Pedro H. C. Siciliano,[a,b] Carla R. Moreira,[a] Odivaldo C. Alves,[c] Alexander Caytuero,[d] Elisa M. B. Saitovitch,[d] Fred. J. Litterst,[e] Deborah V. Cesar,[b] Cristiane A. Henriques[b,b] and Alexandre B. Gaspar[a,a]*

[a]*Instituto Nacional de Tecnologia, Av. Venezuela, 82, SL 518, 20081-312 Rio de Janeiro-RJ, Brazil*

[b]*Instituto de Química, Universidade do Estado do Rio de Janeiro, Rua S. Francisco Xavier, 524, 20550-013 Rio de Janeiro-RJ, Brazil*

[c]*Instituto de Química, Universidade Federal Fluminense, Campus do Valonguinho s/n, 24020-007 Niterói-RJ, Brazil*

[d]*Centro Brasileiro de Pesquisas Físicas, Rua Xavier Sigaud, 150, Urca, 22290-180 Rio de Janeiro-RJ, Brazil*

[e]*Institut für Physik der Kondensierten Materie, Technische Universität Braunschweig, Mendelssohnstr. 3, 38106 Braunschweig, Germany*

Nanocomposites of magnetite anchored on reduced graphene oxide with different magnetite:reduced graphene oxide mass ratios were synthesized and evaluated in indigo carmine photo Fenton discoloration. All nanocomposites are magnetic and showed comparable amounts of magnetite and hematite with a higher level of hematite for low iron contents. The highest value of 63.6 emu $g^{-1}$ was obtained for the nanocomposite with the highest magnetite content. The nanocomposites presented high dispersion of iron oxide particles, at about 12 nm on reduced graphene oxide surface sheets. The samples also showed bandgap energies below that found for bulk magnetite, showing an important effect of reduced graphene oxide. The nanocomposite with an iron nitrate precursors mass ratio of 17:1 showed the best performance (99.7% of indigo carmine discoloration ($2.1 \times 10^{-5}$ mol $L^{-1}$) at 30 min of reaction, hydrogen peroxide ($2.3 \times 10^{-3}$ mol $L^{-1}$), and a catalyst dosage of 0.67 g $L^{-1}$). Reusability tests were performed, and this nanocomposite was shown to be active for at least three recycles. X-ray photoelectron spectrum of $Fe2p_{3/2}$ showed that the $Fe^{III}/Fe^{II}$ ratio was maintained even after three recycles (4 runs), meaning that reduced graphene oxide is responsible for stabilizing magnetite particles, thus maintaining its photocatalytic activity.

**Keywords:** iron oxides, reduced graphene oxide, heterogeneous photocatalysis, indigo carmine

## Introduction

Water contamination is one of the major environment-related issues, and it is associated not only with health problems but with severe socioeconomic impacts.[1-4] It is estimated that around 10,000 different synthetic dyes are used, with significant losses of these compounds to the environment after dyeing procedures.[5,6] Indigo carmine (IC) is an artificial vibrant blue dye, spread worldwide due to its use in denim making. It is an indigoid organic dye and its molecule possesses two sulfonic groups. Besides, it is well known that IC brings health risks because it is toxic, mutagenic, and very stable in nature.[7] These characteristics are driving forces to develop new technologies to mitigate water pollution by synthetic organic dyes.

Different techniques are investigated to remediate dying wastewater pollution, such as ultrafiltration, electrochemical, and adsorption.[8] However, heterogeneous photocatalysis of organic dyes emerges as a promising approach due to its advantages, such as catalyst recovery and reuse, use in mild conditions, pollutant chemical transformation, and others.[9,10] These reactions are considered advanced oxidative processes (AOPs), where hydroxyl radicals (•OH) are generated from $H_2O_2$ decomposition, assisted by a light source and a semiconductor oxide.[11] These

*e-mail: cah@uerj.br; alexandre.gaspar@int.gov.br
Editor handled this article: Célia M. Ronconi (Associate)

**APPENDIX C –** Scientific Production (Proceedings of Conferences)

The scientific production published in proceeding of conferences is presented hereby.

**Event:** International Conference on the Applications of the Mössbauer Effect, September, 2023, Cartagena, Colombia.

- Title: Photo-Fenton Removal of Indigo Carmine Dye from Contaminated Waters Using Nanocomposites of $Fe_3O_4$/RGO. Authors: Alexander Caytuero, Jochen Litterst, Arthur H.A. Gonçalves, Pedro H. Siciliano, Deborah V. Cesar, Cristiane A. Henriques, Alexandre B. Gaspar.

**Event:** 21º Congresso Brasileiro de Catálise, September, 2021, online, Brazil.

- Title: Avaliação de Parâmetros Reacionais para a Descoloração Foto-Fenton do Corante Índigo Carmim com o Compósito Magnético $Fe_3O_4$/RGO. Authors: Arthur H.A. Gonçalves, Pedro H. Siciliano, Carla R. Moreira, Odivaldo C. Alves, Deborah V. Cesar, Cristiane A. Henriques, Alexandre B. Gaspar.

**Event:** 4º Encontro de Catálise REGIONAL 2 "A Catálise em Transição, March, 2021, online, Brazil.

- Title: Síntese do Compósito Magnético $Fe_3O_4$/RGO para a Descoloração Foto-Fenton do Índigo Carmim. Authors: Arthur H.A. Gonçalves, Pedro H. Siciliano, Odivaldo C. Alves, Deborah V. Cesar, Cristiane A. Henriques, Alexandre B. Gaspar.

**Event:** 5$^{th}$ BRICS Young Scientist Forum and BRICS Young Innovator Prize, September, 2020, Chelyabinsk, Russia.

- Title: Synthesis of a Magnetic $Fe_3O_4$/RGO Composite for the Rapid Photo-Fenton Discoloration of Indigo Carmine Dye: Arthur H.A. Gonçalves, Pedro H. Siciliano, Odivaldo C. Alves, Deborah V. Cesar, Cristiane A. Henriques, Alexandre B. Gaspar.